Wet Chemistry Synthesis towards Nanostructures of Thermoelectric Antimonides

Dissertation

zur Erlangung des Grades

„Doktor der Naturwissenschaften“

im Promotionsfach Chemie

am Fachbereich Chemie,

Pharmazie und Geowissenschaften

der Johannes Gutenberg-Universität Mainz

Christina Birkel

geboren in Heidelberg

Mainz, 2010

Dekan: [redacted]

1. Berichterstatter: [redacted]

2. Berichterstatter: [redacted]

Tag der mündlichen Prüfung: [redacted]

The work for this thesis was carried out at the Johannes Gutenberg - University of Mainz and the Seoul National University, Korea in the period between October 15th, 2007 and October 7th 2010, under the guidance of [redacted]

Diese Arbeit wurde an der Johannes Gutenberg - Universität Mainz und an der Staatlichen Universität in Seoul, Korea in der Zeit vom 15. Oktober 2007 bis zum 07. Oktober 2010 angefertigt. Die Arbeit wurde von den [redacted] betreut.

Abstract

This work focuses on the solution based synthesis of nanoparticular antimonides covering the following main issues:

From a chemistry point of view, new synthetic routes have been developed to nano-sized compounds out of the Zn-Sb and Fe-Sb systems, i.e. "Zn_4Sb_3", ZnSb, $FeSb_2$ and $Fe_{1+x}Sb$. Different from conventional solid state reactions established in bulk materials synthesis, the synthesis of nanoparticles has to avoid agglomeration and Ostwald ripening. Thus, reasonable reaction times at comparable low temperatures afford small diffusion paths and low activation barriers. Therefore, the synthetic approach establishes reacting pre-synthesized antimony nanoparticles with properly chosen, molecular or nanoparticular precursors of the corresponding transition metals.
Furthermore, anisotropic ZnSb nanomaterials have been prepared by a templateassisted approach using either AAO (anodized aluminum oxide) or polycarbonate membranes. The obtained products have mainly been investigated by X-ray diffraction techniques and by electron microscopy. Evaluation of the powder X-ray diffraction data has been a challenging task since nanostructuring and presence of multiple phases cause broad and overlapping peaks.

Additionally, Fe-Mößbauer measurements have been carried out in the case of the Fe-compounds in order to provide further insight into phase compositions. The hitherto unknown phase $Zn_{1+x}Sb$ has been subjected to a detailed crystal structure analysis applying a new diffraction technique, Automated diffraction tomography (ADT).

From a physical point of view, Zn_4Sb_3, ZnSb and $FeSb_2$ are interesting thermoelectric materials and have attracted a lot of interest due to their capability to convert between thermal and electrical energy. Nanomaterials are known to exhibit an enhanced conversion efficiency in comparison to bulk materials due to a decreased thermal conductivity. Since thermoelectric devices require solid materials but not loose powders, the solidification and densification of the obtained nanoparticular powders have played a major role in this study. Spark plasma sintering has been used to solidify the materials, which involves rapid heating and cooling to prevent grain growth in the samples. Finding the optimum sintering conditions is the subject of ongoing research.

Another issue that arises is the phase stability of the compounds during the sintering process. Despite the fast pressing of the samples, partial decomposition of the $Zn_{1+x}Sb$ compound was observed, as has been detected by data analysis of Synchrotron X-ray diffraction data.

Morphology and density of the different compacted materials have been determined by Scanning electron microscopy and Laser microscopy. Lattice dynamics have been investigated by means of heat capacity and Nuclear inelastic scattering investigations. The thermal conductivity of the nanostructured materials is decreased drastically in comparison to the bulk materials - by more than two orders of magnitude in case of nanoparticular $FeSb_2$. Depending on the composition and especially the mechanical strength of the solidified nanomaterials, thermoelectric properties, such as Seebeck coefficient, electrical and thermal conductivity, have been determined.

Abstract - German

Die vorliegende Arbeit befasst sich mit der Synthese von nanostrukturierten Antimoniden, wobei die folgenden beiden Themen bearbeitet wurden:

Aus chemischer Sicht wurden neue Synthesewege entwickelt, um Nanopartikel der Verbindungen in den binären Systemen Zn-Sb und Fe-Sb herzustellen ("Zn_4Sb_3", ZnSb, $FeSb_2$ and $Fe_{1+x}Sb$). Anders als in konventionellen Festkörperreaktionen, die auf die Synthese von Bulk-Materialien oder Einkristallen zielen, muss die Synthese von Nanopartikeln Agglomerate und Ostwald-Wachstum vermeiden. Daher benötigen annehmbare Reaktionszeiten und vergleichsweise tiefe Reaktionstemperaturen kurze Diffusionswege und tiefe Aktivierungsbarrieren. Demzufolge bedient sich die Synthese der Reaktion von Antimon-Nanopartikeln mit geeigneten molekularen oder nanopartikulären Edukten der entsprechenden Übergangsmetalle.

Zusätzlich wurden anisotrope ZnSb Strukturen synthetisiert, indem eine Templat-Synthese mit Hilfe von anodisierten Aluminiumoxid- oder Polycarbonat-Membranen angewandt wurde.

Die erhaltenen Produkte wurden hauptsächlich durch Röntgen-Diffraktion und Elektronenmikroskopie untersucht. Die Auswertung der Pulver Röntgendiffraktions-Daten stellte eine Herausforderung dar, da die Nanostrukturierung und die Anwesenheit von mehreren Phasen zu verbreiterten und überlagernden Reflexen führen. Zusätzliche Fe-Mößbauer Messungen wurden im Falle der Fe-Sb Produkte vorgenommen, um detailliertere Informationen über die genaue Zusammensetzung zu erhalten. Die erstmals hergestellte Phase $Zn_{1+x}Sb$ wurde einer detaillierten Kristallstrukturanalyse unterzogen, die mit Hilfe einer neuen Diffraktionsmethode, der automatisierten Elektronen Diffraktions Tomographie, durchgeführt wurde.

Aus physikalischer Sicht sind Zn_4Sb_3, ZnSb and $FeSb_2$ interessante thermoelektrische Materialien, die aufgrund ihrer Fähigkeit thermische in elektrische Energie umzuwandeln, großes Interesse geweckt haben. Nanostrukturierte thermoelektrische Materialien zeigen dabei eine höhere Umwandlungseffizienz, da deren thermische Leitfähigkeit herabgesetzt ist. Da thermoelektrische Bauteile aus dichten Bulk-Materialien gefertigt werden, spielte die Verfestigung der synthetisierten nanopartikulären Pulver eine große Rolle. Die als "Spark Plasma Sintern" bezeichnete Methode wurde eingesetzt, um die Proben zu pressen. Dies ermöglicht schnelles Heizen und Abkühlen der Probe und kann so das bei klassischen Heißpress-Methoden unvermeidliche Kristallitwachstum verringern. Die optimalen Bedingungen für das Spark Plasma Sintern zu finden, ist Inhalt von bestehender und weiterführender Forschung.

Ein Problem stellt die Stabilität der Proben während des Sinterns dar. Trotz des schnellen Pressens wurde eine teilweise Zersetzung im Falle des $Zn_{1+x}Sb$ beobachtet, wie mit Hilfe von Synchrotrondiffraktionsuntersuchungen aufgedeckt wurde. Morphologie und Dichte der verschiedenen verfestigten Materialien wurden mittels Rasterelektronenmikroskopie und Lasermikroskopie bestimmt. Die Gitterdynamik wurde mit Hilfe von Wärmekapazitätsmessungen und inelastischer Kern-Streuung untersucht. Die Wärmeleitfähigkeit der nanostrukturierten Materialien ist im Vergleich zu den Festkörpern drastisch reduziert - im Falle des $FeSb_2$ um mehr als zwei Größenordnungen. Abhängig von der Zusammensetzung und mechanischen Härte wurden für einen Teil der verfestigten Nanomaterialien die thermoelektrischen Eigenschaften, wie Seebeck Koeffizient, elektrische und Wärmeleitfähigkeit, gemessen.

초록

본 연구는 '용액상에서의 안티모나이드 나노입자 합성'에 대한 것으로, 구체적인 연구결과를 서술하면 다음과 같다.

화학적 관점에서 보면 본 연구결과는, 나노미터 크기의 Zn-Sb와 Fe-Sb계 화합물(예를 들면, Zn_4Sb_3, ZnSb, $FeSb_2$, $Fe_{1+x}Sb$)의 합성을 위한 새로운 합성 방법이 개발된 것이다. 나노입자 합성은 기존의 벌크 물질을 만드는 고체 상태에서의 반응과는 달리 응집작용과 Ostwald ripening이 일어나서는 안 된다. 즉, 비교적 낮은 온도에서 적절한 시간 동안 반응시켜 분산 패스(path)와 활성화 에너지 장벽을 최소화시키는 것이 중요하다. 따라서 본 연구에서는 미리 합성된 안티모니 나노입자에 합성하고자 하는 전이금속에 상응하는 분자 또는 나노입자 크기의 전구체를 선택적으로 도입하여 반응시키는 방법을 개발하였다.

또한 이방성의 ZnSb 나노물질을 다공성 산화알루미늄(AAO) 또는 폴리탄산에스테르(polycarbonate) 박막을 템플레이트로 사용하여 합성하였다. 합성된 화합물은 엑스선 회절 분광법과 전자현미경 사진 분석을 통해 확인하였다. 분말 엑스선 회절 패턴은 나노구조체와 여러 개 상(phase)의 존재에 의한 넓고 겹쳐지는 피크가 있음에도 불구하고 분석을 시도하였다. Fe-화합물의 경우, 상 구조에 대한 구체적인 정보를 얻기 위하여 Fe-뫼스바우어 분광 측정을 하였다. 지금까지 알려지지 않은 상인 $Zn_{1+x}Sb$에 대해서는 새로운 회절 분석법인 회절 단층촬영기법을 통해 세부적인 결정구조 분석을 하였다.

물리학적 관점에서 보면 Zn_4Sb_3, ZnSb, $FeSb_2$는 열전화합물로써 열 에너지와 전기 에너지의 전환이 용이하다는 점 때문에 많이 연구되고 있다. 나노물질은 낮은 열 전도성 때문에 벌크물질에 비해 더 높은 전환 효율을 보인다고 알려져 있다. 열전소자는 고체상 물질을 필요로 하기 때문에, 이 연구에서는 얻어진 나노입자 분말의 고체화와 밀집화 과정이 중요하다. 열처리와 냉각을 빠르게 할 수 있는 방전 플라즈마 소결법은 시료의 입자성장을 막을 수 있으므로 물질을 고체화시키는 데 많이 사용되어왔다. 최적의 소결(sintering) 조건을 찾는 것은 계속 연구 중이다.

또 하나의 이슈는 화합물 소결 과정 동안의 상 안정성이다. 시료를 빠르게 가압(pressing) 함에도 불구하고 $Zn_{1+x}Sb$ 화합물에서는 부분적으로 분해가 일어남을 방사광 엑스선 회절 분석을 통해 관찰하였다.

각각 다른 압축된 물질의 형태와 밀도를 주사전자현미경과 레이져현미경을 통해 관찰하였다. 격자 역학은 열용량과 비탄력적 핵 산란 실험에 의해 시행되었다. 나노구조체 물질의 열전도성은 벌크 물질에 비해 급격히 떨어졌다 – $FeSb_2$ 나노입자의 경우 두 배 이상 감소. 고체화된 나노물질의 구조와 기계적 강도에 따라 Seebeck 계수, 전기 전도성, 열 전도성과 같은 열전성질이 결정되었다.

Acknowledgements

First of all, I would like to thank [redacted] for providing this interesting project for my PhD thesis. He has always encouraged me to participate in as many conferences and research visits as possible which I appreciate a lot and which allowed ongoing exchange with other scientists working in this area.

Many thanks to [redacted] for the extensive powder X-ray diffraction measurements and the useful discussions. Special thanks to [redacted] for the support when I was writing this thesis.

I would like to acknowledge all our collaborators within the University of Mainz and from the [redacted]

- [redacted] for their great Elecron microscopy, Electron diffraction and Automated electron tomography work on my compounds,
- [redacted] for the SQUID measurements,
- [redacted] for the PPMS measurements,

- [redacted] for helping me with the TEM measurements and the Laser microscopy images,
- [redacted] for the SEM measurements,
- [redacted] for his help with my project. I hope he will continue his good work.
- [redacted] for providing the Spark plasma sintering facilities at the [redacted] in Dresden. Thank you for hosting me.
- [redacted] for ^{57}Fe-Mößbauer, NIS and heat capacity measurements,
- [redacted] for assistance in setting up the beamline for the synchrotron diffraction,
- [redacted] at the [redacted] for the Seebeck scan measurements
- [redacted] for many useful thermoelectrics discussions.

Thanks to the [redacted] and the [redacted] for all their financial support!

Thank you very much to [redacted] for hosting me in his group at Seoul National University for a total of six months. I would like to acknowlegde [redacted] for our collaboration on the template-assisted syntheses.

One big thank you to [redacted] who contributed many hours of lab work to my thesis.

Furthermore, I would like to thank [redacted] from the administration staff

- [redacted] who does a great job as our group secretary,
- [redacted] who where always very helpful concerning any Korea subjects,
- [redacted] who helped with any issues regarding [redacted]

Many thanks to [redacted] and also [redacted] who have become great advisors during the last couple of years.

I would also like to mention all [redacted] whom I love to meet regularly at conferences and meetings as well as on private visits. [redacted] and everybody else, I really hope we will continue these meetings in the future!

One big thank you to [redacted] for being such a great friend in Seoul and for translating the abstract into Korean (I almost would have been able to do it without you).

Many thanks to the [redacted] in Mainz, especially [redacted] Work would have been much less fun without you! Many special thanks to [redacted] for not only being a great Praktikum partner during our studies but also for being a fantastic fume hood buddy and great scientist. All the best for you in the future!!

Last but not least, I would like to thank [redacted] for all their great help during the last couple of years. I know I will never lose their support which means a lot to me and makes me believe I can achieve my goals in life.

Finally millions of thanks to [redacted] I am not sure if I would be, where I am right now, without him since he has always supported me in every possible way. He is also a huge part of the fun I am having during my work and I would never want to miss that. Let´s stay on that successful and happy track together and never forget

„*Die schönsten Erinnerungen sammelt man immer zu zweit*“.

Contents

List of Figures

List of Tables

Chapter 1

Introduction and motivation

1.1 Energy and thermoelectrics

One of the most crucial problems facing our society today is to address the issue of energy management. To adequately address this challenge, both the supply and the demand side must be considered. Research on the supply side focuses on energy generation and distribution dealing with the different energy sources on our planet. On the demand side the research is focused on the efficiency in delivery and consumption, like buildings that use less energy due to a certain building strategy involving photovoltaics, sensors and passive heating.

1.1.1 Energy landscape

Because of the availability of cheap energy, mainly from fossil fuels, humankind has experienced industrialization and development through all parts of the world during the past few centuries. The energy demand is growing with further development of the industrial countries in the world.

On the other hand, less developed countries only consume a small percentage of the energy the industrialized world uses while these more developed nations struggle daily to cope with an ever increasing demand for more energy. The energy atlas of the world is uneven: Statistics show that Sub-Saharan countries use only one tenth of the energy that North America enjoys and China, in 2006 alone, built more electric power plants than the total installed capacity of Great Britain [4]. The question of what will happen if every country in the world reaches this highest level of development must be asked. From a materials point of view there are three different classes of materials involved in energy management. One are naturally occurring materials which release energy through chemical or nuclear reaction which can be extracted from the ground and are converted into energy through combustion (coal, gas and oil). Other materials are engineered to transform one type of energy into a more useful kind (solar, wind). Finally, there is an ever growing research effort on materials which are designed to store energy from various renewable energy sources which only intermittently produce energy.

Keeping all this in mind, there are two major concerns we have to worry about. Currently, most people rely on the natural energy sources (coal, oil and gas, see figure 1.1) but the question is how long these sources will last, especially with the increasing technological development and energy demand of all the countries in the world.

Some analysts suggest that oil wells might be depleted in 70-80 years, natural gas might run out a little later and coal will last for another 160 years [4, 5]. Even if this may not seem too alarming, the depletion of only one of these sources would make other alternatives very costly. However, running out of resources is not our major concern these days.

Since all our energy technologies leave an environmental footprint in one way or another, people need to take care of what is left behind. For example, nuclear power produces long-lived and short-term radioactive waste which has to be shielded and disposed of very carefully, making nuclear waste pollution and management a major factor in politics. Moreover, energy production from fossil fuels results in emission of CO_2, a long lasting greenhouse gas which is usually released into the atmosphere with significant environmental impact. Studies suggest that a temperature rise of 0.6 ± 0.2°C has already taken place in the 20th century [5] and that the temperature will rise further. Global warming can have irreversible effects on the planet with consequences that include rising sea levels which can threaten populations living in coastal cities and low-lying areas.

Given what is at stake, the search for renewable energy sources with reduced green house gas emissions is a scientific problem of paramount importance.

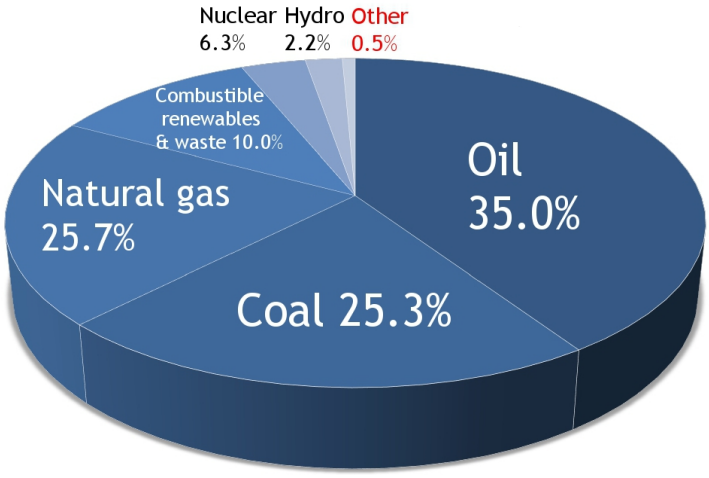

Figure 1.1: Share of the world's primary energy supply in 2007, taken from the International Energy Agency.

1.1.2 Thermoelectric materials

Figure 1.2 illustrates global energy production, various methods for storage, and what the end uses generally are. Beside the classical energy sources, renewable energies, such as hydro-, wind- and solar power, are also included on the map. However, this thesis shall focus primarily on materials which can deliver power as a result of their thermoelectric properties. Such thermoelectrics provide a mechanism to produce and save energy simultaneously which has tremendous potential in all kinds of sectors (residential/commercial, industrial and transportation) since huge amounts of energy are lost as waste heat. Therefore, thermoelectric materials are an emerging field and can play a major role in addressing various associated issues.

Clearly, one can imagine many places where thermoelectric modules could be deployed to harvest waste heat: everywhere from cars to apartment buildings and industrial plants. They have already found their place in distant space missions where they have been working reliably in radioisotope thermoelectric generators which convert heat coming from a radioactive decay into electrical power. However, many current applications are very specialized to small scale applications. The reason for that and why thermoelectrics are not (yet) a part of the energetic landscape (as drawn in figure 1.2) is that their conversion efficiency is still too low for them to function economically.

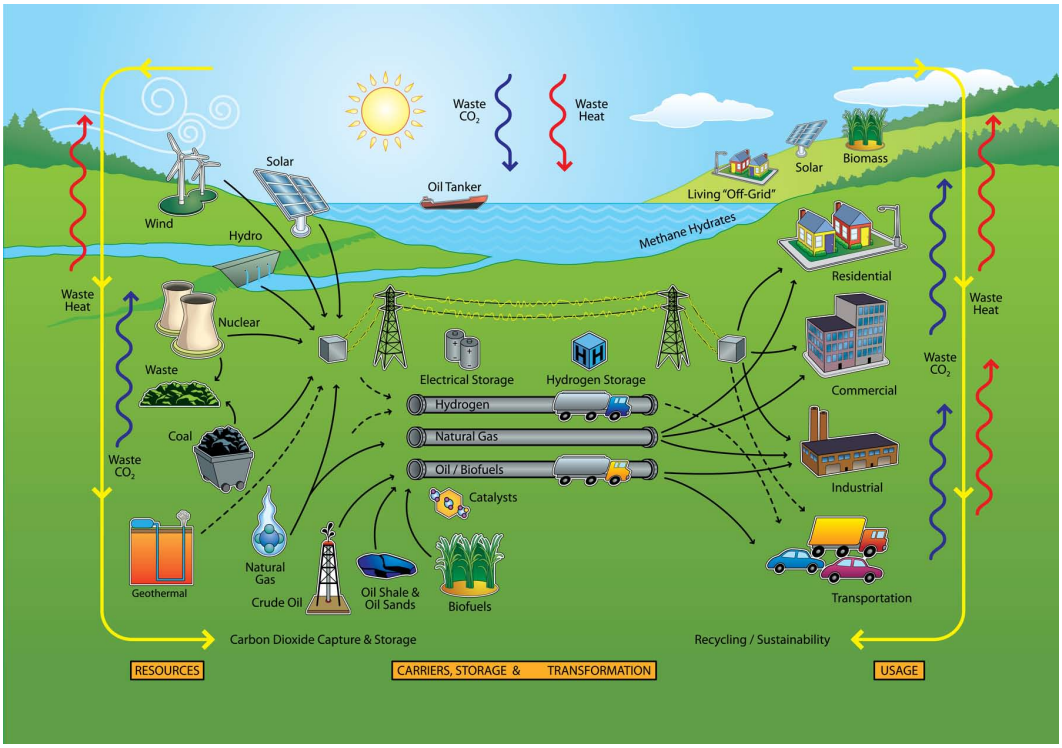

Figure 1.2: Illustration of the energy landscape, reproduced by permission of the *MRS Bulletin* [6].

1.2 General physical concepts

To understand the requirements for a good thermoelectric material one has to begin from some basic physical concepts regarding solid state materials. The following subsections are meant to summarize the fundamental ideas dealing with metals and semiconductors and develop an understanding of what makes a material a good thermoelectric. Information and images have been adapted from "Solid State Physics" [7] and "Thermoelectrics Handbook" [8].

1.2.1 Drude model of metals

In the early 1900's after J. J. Thomson discovered the electron, P. Drude proposed his theory of electrical and thermal conduction by applying the kinetic theory of gases to a metal. His theory treats a metal as a gas of electrons consisting of immobile positive ions and detached moving electrons (figure 1.3).

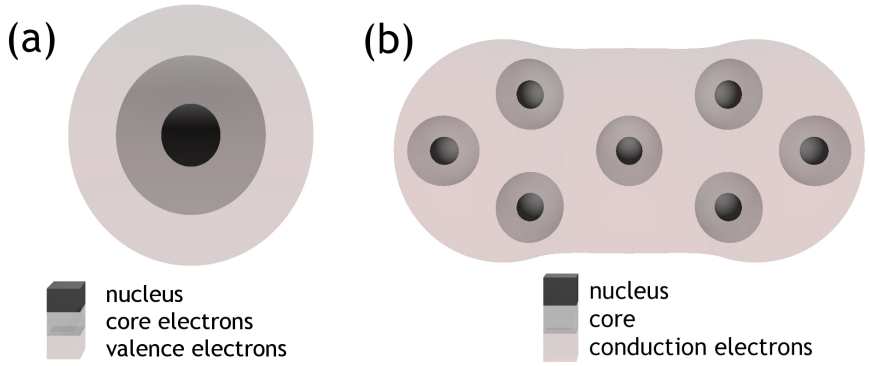

Figure 1.3: a) Schematic picture of an isolated ion (not to scale), b) in a metal the core electrons remain bound to the core to form the metallic ion while the valence electrons leave the atom to form the electron gas and are called conduction electrons.

Drude's theory is formulated around the following basic assumptions:

1. Electron-electron and electron-ion interactions between collisions are neglected.

2. Collisions abruptly alter the velocity of an electron; while Drude originally attributed them to electrons bouncing off the ion cores, more complex scattering mechanisms should also be considered.

3. Drude assumed that an electron experiences a collision with a probability per unit time $1/\tau$, where τ is called the relaxation time, collision time or mean free time.

4. Electrons are assumed to achieve thermal equilibrium with their surroundings only through collisions. This means that the hotter the region in which the collision occurs, the faster a typical electron will emerge from the collision.

We will see later how the last assumption affects the background of thermoelectric properties.

The Drude model is a very powerful tool for predicting and explaining many of the observed phenomena in metals. However, there are also some discrepancies and numbers that differ significantly from the observed ones which cannot be explained with this model.

1.2.2 Sommerfeld model of metals and band/electronic structure

In Drude´s time it was reasonable to assume that the electronic velocity distribution was given in equilibrium at temperature T by the Maxwell-Boltzmann distribution, like that of an ordinary classical gas. With the dawn of quantum theory it was recognized that for electrons the Pauli exclusion principle requires the replacement of the Maxwell-Boltzmann distribution with the Fermi-Dirac distribution. The Pauli exclusion principle states that no two electrons can simultaneously occupy the same quantum state.

The Sommerfeld model is an improvement upon the Drude model in that the electronic velocity distribution is taken to be the quantum Fermi-Dirac distribution rather than the classical Maxwell-Boltzmann distribution.

The Fermi-Dirac distribution is used to find the probability that a fermion occupies a specific quantum state in a system at thermal equilibrium. This probability function is often combined with the so-called density of states (DOS) describing the number of states at each energy level that can be occupied which results in the number of occupied states per unit volume at a given energy for a system at thermal equilibrium. According to Drude´s model, solids can be considered as periodic arrays of valance orbitals embedded in a matrix of atomic cores where the core electrons are very tightly bound at each site which allows for their dynamics to be ignored. This is known as the tight-binding approach. Because of the translation symmetry of the crystal structure, one can simplify the solid by considering it as a single atom and studying the mechanism which binds the lattice into a periodic structure.

When a solid is formed, the energy levels of the atoms broaden and form bands with forbidden bands between them (figure 1.4). The electrons can have energy values existing within one of the bands but cannot have energies corresponding to values in the gaps between the bands. As mentioned before, the lower-energy bands due to the inner atomic levels are narrower and full of electrons with the result that they do not contribute to the electronic properties of the material.

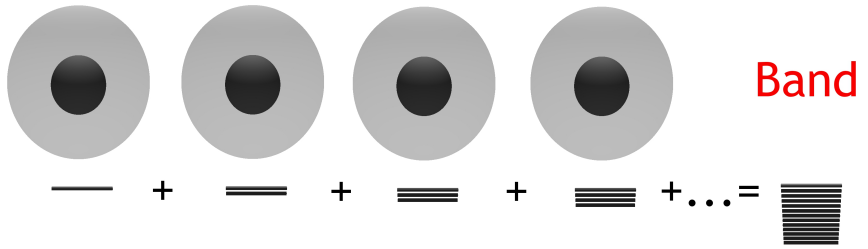

Figure 1.4: If we bring many orbitals into proximity so that they may exchange electrons (hybridize), then a band is formed centered around the location of the isolated orbital, and with width proportional to the strength of the hybridization.

We will see later why the concept of the band structure of different classes of materials is so important in thermoelectric research.

1.2.3 Thermoelectric figure of merit

If a material is to work economically, its conversion efficiency must be as high as possible. One key issue in energy management is to design and optimize efficient conversion modules for electrical power generation. For thermoelectrics, their efficiency is described through the equation:

$$\eta = \frac{T(hot) - T(cold)}{T(hot)} \cdot \frac{\sqrt{1+ZT}-1}{\sqrt{1+ZT}+\frac{T(cold)}{T(hot)}} \tag{1.1}$$

This equation contains the Carnot efficiency as well as a factor ZT which is called the thermoelectric figure of merit. Figure 1.5 shows how the efficiency raises depending on the temperature on the hot side (T(hot)) and the value of ZT.

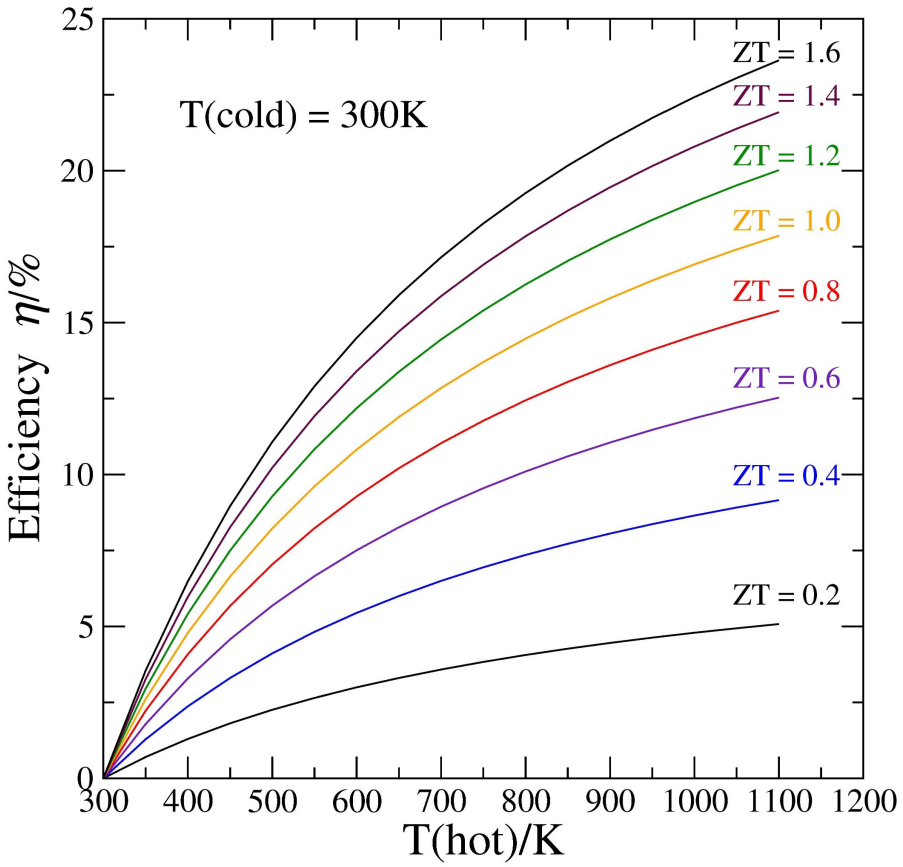

Figure 1.5: The conversion efficiency increases with increasing temperature difference between the hot and the cold side and with increasing ZT value.

ZT contains many different materials properties, including the Seebeck coefficient S, electrical conductivity σ, and thermal conductivity κ as well as the absolute temperature T (see equation 1.2). In the following sections we will discuss each in detail.

$$ZT = \frac{S^2\sigma}{\kappa} \cdot T \tag{1.2}$$

1.2.3.1 Thermoelectric power - the Seebeck effect

In 1826 Thomas Johann Seebeck discovered that if the junction of two dissimilar metals are at different temperatures an electrical current is produced (see figure 1.6). This can be understood if we assume that the electron gas can move freely through the material, the electrons coming from a hotter region will have a higher thermal energy than the ones coming from a colder region. This means that the "hot electrons" move faster towards the cold region than the "cold electrons" move towards the hot region which results in a nonvanishing mean electronic velocity directed towards the cold region. Since the electrons are charged, this velocity will result in an electrical current directed opposite to the temperature gradient.

The voltage produced is proportional to the temperature difference between the two junctions. The proportionality constant (S) is known as the Seebeck coefficient, and often referred to as the thermoelectric power or thermopower:

$$V = S(T(hot) - T(cold)) \tag{1.3}$$

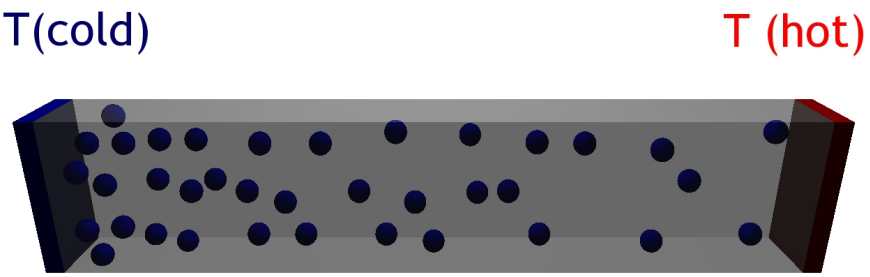

Figure 1.6: Scheme of the electric field built up by a temperature gradient inside a material, electrons (blue circles) moving faster to the cold region on the left side.

In order to measure the thermopower one needs a circuit of two dissimilar metals (figure 1.7).

The voltmeter must connect points of the specimen at the same temperature, otherwise there would be a temperature gradient within the circuit of the meter itself resulting in an additional thermoelectric voltage. One can exploit the fact that no thermoelectric voltage develops across a superconducting metal, thus if one of the materials is a superconductor, the measurement yields directly the thermoelectric voltage across the other material. Beside this effect, thermoelectric materials can also be used in cooling devices, such as refrigerators or laser cooling systems. This force which acts opposite to the Seebeck effect is called the Peltier effect [9]. If you apply a voltage to such kind of material one side of the material will cool down while the other one is heating up. Those Peltier system are already used in laser cooling and other refrigeration devices.

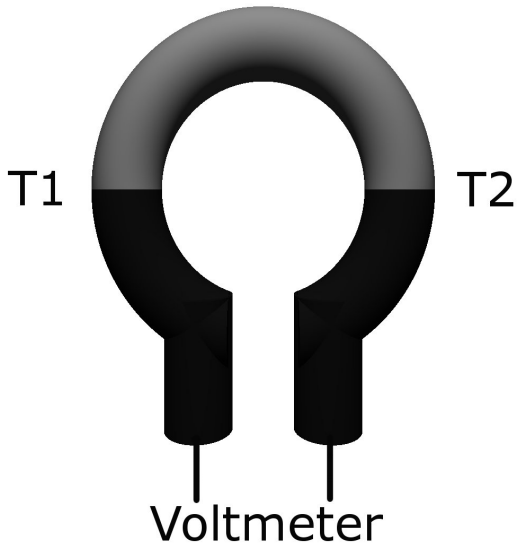

Figure 1.7: Circuit of two different metals where the thermopower can be measured if T1 and T2 are different temperatures.

1.2.3.2 Transport properties

Since thermoelectric materials convert a temperature gradient into electrical energy, one must study the transport of charge (electrical conductivity) as well as heat (thermal conductivity) in the corresponding material. Thermal conductivity in thermoelectric materials comes from two sources: (a) electrons and holes transporting heat (κ_e) and (b) phonons traveling through the lattice (κ_l).

$$\kappa = \kappa_e + \kappa_l \tag{1.4}$$

Most of the electronic term is directly related to the electrical conductivity through the Wiedemann-Franz law (1853):

$$\frac{\kappa}{\sigma T} = L \tag{1.5}$$

where L is the Lorenz factor which is 2.4×10^{-8} $J^2K^{-2}C^{-2}$ for free electrons.

While the electrical conductivity of a given material simply describes its ability to conduct an electrical current, the thermal conductivity seems to be more complex. Heat transfer involves transfer of energy within a material without any motion of the material as a whole. The reasons for the thermal conduction can be quite different which can be expected from what was stated earlier, namely κ consisting of an electronic and a lattice contribution. For metals, the best electronic conducting materials are also the best thermal conductors and the relation between the two can directly be described with the Wiedemann-Franz law.

For non-metallic solids, the heat transfer is viewed as being transferred via lattice vibrations, as atoms vibrating more energetically in one part of the material transfer their energy to less energetic neighboring atoms. This heat transfer is often described by means of "phonons". Gases, on the other hand, transfer their heat through collision of molecules and their thermal conductivity is much lower compared to most solids since they are a dilute media. Among the solid materials, glasses exhibit the lowest thermal conductivity, since their conduction is viewed as a random walk of energy through the lattice, rather than a rapid transport via phonons (concept of minimum thermal conductivity [10]).

In both transport phenomena, mechanisms which disrupt the transport of charge and heat must not be ignored. Scattering mechanisms, such as electron-electron or electron-phonon interactions have to be addressed at the appropriate point.

1.3 Thermoelectric efficiency

Following these basic physical concepts, it is important to discuss the properties which make any material a good and effective thermoelectric. As mentioned before, all material properties are physically interconnected which creates a huge challenge for thermoelectric research. In the following section, the different material types, their electronic structures and their influence on the thermoelectric performance, including Seebeck coefficient, electronic and thermal conductivity, shall be discussed.

1.3.1 Finding a good thermoelectric

Solids can be classified by their crystal structure or by their materials properties. While their crystal structure affects the properties in many different ways, within each of the seven crystal systems one can find solids exhibiting a full range of electrical, mechanical and optical properties.

1.3.1.1 Electronic structure

It can be useful - especially from the thermoelectric point of view - to establish a scheme which is based on the configuration of the valence electrons. The electronic structure (or band structure) of three material classes looks very much different and one can distinguish between metals/conductors, semiconductors and insulators (figure 1.8).

The outer or valence electrons binding the crystal together occupy a valence band, which, for an insulating material, is full of electrons which cannot move since they are fixed in position in chemical bonds. The conduction band is far above the valence band in energy and it remains empty.

For a semiconductor, the gap between the valence and the conduction bands is much less and the energy of the gap is closer to the thermal energy $k_B T$. This means that the heat content of the material at room temperature can thermally excite some of the electrons from the valence to the conduction band where they carry current. A material of this type is called intrinsic semiconductor. There are also extrinsic semiconductors which exhibit conduction due to impurities within the material. A metal/conductor is a material with a full valence band and a conduction band partly full with delocalized conduction electrons which are efficient in carrying electric current.
In actual crystals, the band structures are much more complicated than is suggested in the sketches in figure 1.8, with the bands depending on the direction in the crystal lattice.

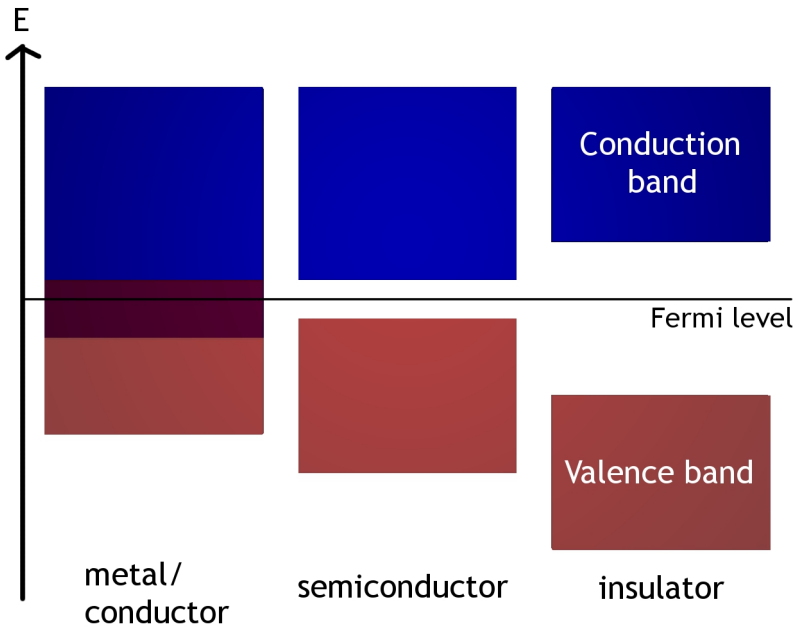

Figure 1.8: Scheme of the electronic band structures of metals, semiconductors and insulators; the gap between the valence and the conduction band is called band gap.

1.3.1.2 Conflicting material properties

Which class of materials is the best thermoelectric material? To answer this question we have to look once again into the material properties of the different materials. According to the thermoelectric figure of merit which determines the thermoelectric efficiency, the Seebeck coefficient as well as the electrical conductivity must be high, while the thermal conductivity should be as low as possible.

A large Seebeck coefficient needs only one type of charge carrier. Mixed n- and p-type conduction leads to both carriers moving to the cold side and canceling out the desired thermoelectric effect. Low carrier concentration insulators and also semiconductors have large Seebeck coefficients. The downside of these materials is that their electronic conductivity is quite low. In general, the Seebeck coefficient decreases with increasing carrier concentration while electrical and thermal conductivity decrease. Thus, there is an area between 10^{19} and 10^{21} carriers per cm^3 where the power factor ($S^2\sigma$) and the figure of merit have a maximum. This area falls in between common metals and semiconductors, which is concentrations found in heavily doped semiconductors.

Another important number is the effective mass m^* which refers to the density-of-states effective mass increasing with flat, narrow bands with high density of states at the Fermi surface. This provides another challenge, since large effective masses are responsible for high thermopowers but low electrical conductivity. The exact relation between the effective mass and the transport properties is complicated depending on electronic structure, scattering mechanisms and anisotropy. One must find a balance for high effective masses which are accompanied by low mobilities and it is not obvious which effective mass is the optimum.

In order to increase ZT, one must decouple the electronic (Seebeck S, electrical conductivity σ) from the thermal properties (thermal conductivity κ). This can be realized using the "phonon-glass electron-crystal" approach proposed by Slack [10]. This idea requires a material where the phonons (responsible for the heat transport) behave in a glass-like manner with a high degree of phonon scattering which lowers the thermal conductivity. The electrons, on the other hand, must experience it as a crystal with low electron scattering and a high electronic conductivity. In classical thermoelectric materials, this was realized through site substitution with isoelectronic elements preserving the crystalline structure of the material while inserting large mass contrast to disrupt the phonon path [11]. Prominent examples of thermoelectric materials based on the "phonon glass-electron crystal" concept [12, 13] are the skutterudites [12] or "Zn_4Sb_3" studied here.

1.3.2 State of the art thermoelectric materials

As mentioned before, the materials best suited for application in thermoelectric modules are usually highly doped semiconductors, since they provide the best compromise in terms of the conflicting material properties. Every material possesses an ideal working temperature where it exhibits the highest conversion efficiency.
The most commonly used materials in thermoelectric applications are alloys of Bi_2Te_3 and Sb_2Te_3 (group V chalcogenides). These compounds, with rather low melting points, are used in cooling units which are required to operate around room temperature. A lot of work has been done on these kinds of materials, much of which was published decades ago [14–16].

Peak ZT values which can be realized with these materials are typically in the range of 0.8 to 1.1 [11].

On the search for thermoelectric materials operating in an extended temperature range, group IV chalcogenides have been investigated [16, 17], such as PbTe, GeTe and SnTe. PbTe for example exists in a wide range of stoichiometries and its conductivity sign and magnitude can be varied from n-type to p-type by controlling the lead and tellurium content [18]. The highest ZT in optimized n-type material ranges around 0.8. Higher ZT values (ZT>1) have been reported for $AgSbTe_2$ alloys, both n- and p-type [19]. The p-type alloy $(GeTe)_{0.85}(AgSbTe_2)_{0.15}$ (referred to as TAGS) with a maximum ZT greater than 1.2 [20] has been used in long-life thermoelectric generators. In the high temperature region above 900 K Si-Ge alloys (both n- and p-type) are used, although their ZT values are rather low due to the high thermal conductivity of the diamond structure.

1.3.3 Approaches to improve the thermoelectric efficiency

Thermoelectric research almost exclusively focuses on strategies to enhance the thermoelectric figure of merit ZT. Among the four parameters involved in the figure merit, three of them are mainly related to the electronic structure of the material (S, σ and κ_e) and one is mainly related to the lattice (κ_l). One approach to increase ZT is to reduce the lattice thermal conductivity without significantly influencing the electronic properties of the material.

This idea has been followed extensively in the past, e.g. Goldsmid *et al.* have calculated how the different kinds of phonons contribute to the thermal conductivity [21].

They showed that in solid solutions heat is primarily carried by the low-frequency phonons which are particularly sensitive to boundary scattering. Spitzer has collected the lattice thermal conductivities of many semiconductors and discussed them in the terms of their crystal structure and valence states of the containing ions [22]. In this work, Spitzer states that in general, increasing coordination of the ions is associated with decreasing thermal conductivity and that low κ can also be caused by cation or anion vacancies. Goldsmid has also summarized that thermal conductivity falls with increasing average atomic weight and increasing ionicity of the bonds between the atoms (observation by Ioffe) [14].
According to his work, semiconductors can be divided into two general groups: normal valence semiconductors are defined as consisting of elements with normal chemical valances; non-normal valence semiconductors are those requiring anion-anion and/or cation-cation bonds. This is accompanied by fundamental differences in crystal structure and it is generally observed that complex crystal structures are associated with low thermal conductivities.

Toberer *et al.* argue that chemical control of carrier concentration (n) is the most important step in the optimization of the thermoelectric figure of merit. They showed that one can start with a valence balanced composition and substitute elements of a different formal valence to change in the desired manner [23].

1.3.4 Nanostructured thermoelectrics

In the early 1990s, Hicks and Dresselhaus [24, 25] pioneered the concept that quantum confinement of electrons and holes in low-dimensional materials could drastically increase ZT by independently changing $S^2\sigma$. These predictions triggered some intensive research in the field of nanostructured thermoelectrics and many groups could proof them experimentally [19, 26, 27]. However, these structures mainly benefited from a reduced thermal conductivity and quantum confinement has not yet played a major role in increasing ZT. Nanostructures may be prepared with one or more dimensions smaller than the mean free path of the phonons and yet larger than that of electrons and holes. This potentially reduces κ without decreasing σ (figure 1.9).

Different approaches to decrease κ_{ph} by reducing the mean free path of phonons while maintaining the electronic properties of doped semiconductors have been attempted: (i) alloying [28], (ii) nanostructuring [19, 29], and (iii) guest atom inclusion [30, 31].

One strategy for creating the required scattering interfaces relies on the synthesis of nanoparticles and multiphase composites mixed on the nanometer scale. These nanostructured materials can be formed as thin-film superlattices or as intimately mixed composite structures. The first demonstration that a low-dimensional material system could enhance thermoelectric performance was for a 2D superlattice consisting of PbTe quantum wells, $Pb_{1-x}Eu_xTe$ barriers [32] and $(Bi,Sb)_2Te_3$ superlattices [33, 34]. Epitaxial-type superlattice structures are formed and their sizes can be controlled by phase separation of metastable ternary compounds into their corresponding binaries [29, 30, 35, 36].

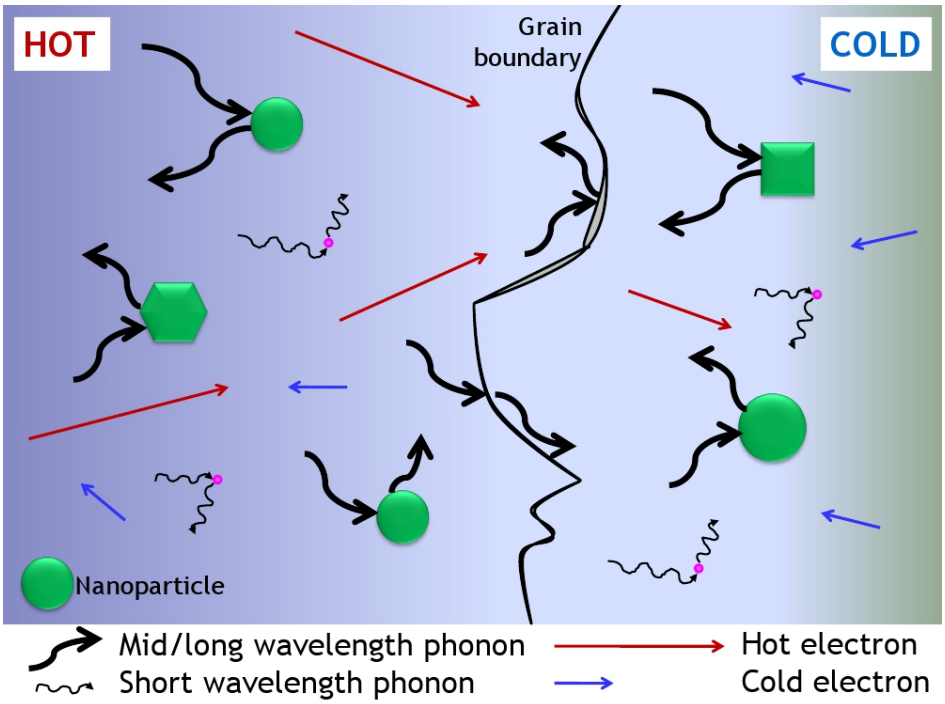

Figure 1.9: Schematic diagram illustrating various phonon scattering mechanisms within a thermoelectric material, adapted from [37].

Chapter 2

Aims and contents of the project

Nanoparticles of thermoelectric materials have been shown to increase the material´s conversion efficiency due to reduced thermal transport as a result of phonon scattering on the particle interfaces. The bulk binary antimonides "Zn_4Sb_3" and $FeSb_2$ are hot candidates in thermoelectric research these days due to reports on their promising thermoelectric performances.
Therefore, the synthesis of nanoparticles of different transition metal antimonides shall be the main target of this work.

Different from conventional solid state reactions established in bulk materials synthesis, the synthesis of nanoparticles has to avoid agglomeration and Ostwald ripening. Thus, reasonable reaction times at comparable low temperatures afford small diffusion path ways and low activation barriers.
The aim of this work shall be to optimize a solution-based synthesis route for "Zn_4Sb_3", ZnSb, $FeSb_2$ and $Fe_{1+x}Sb$ nanoparticles, avoiding intrinsic as well as extrinsic impurities.

Since thermoelectric devices require solid materials but not loose powders, the solidification and densification of the obtained nanoparticular powders shall be an additional target within this work. Taking into account the metastable nature of nanosized samples, a special pressing technique, Spark plasma sintering (SPS), shall be applied.
All materials, powders and solidified workpieces, will be investigated carefully in order to gain comprehensive knowledge on their structure, composition and morphology.
Finally, data on their thermoelectric performance shall be obtained by lattice dynamics and transport properties measurements.

In the following, the target materials as well as the solidification method and the characterization techniques of the products shall be introduced.

2.1 Investigated materials

2.1.1 Zn-Sb system

Within the Zn-Sb system, two materials are known to exhibit strong thermoelectric properties which are ZnSb and Zn_4Sb_3. "Zn_4Sb_3" (more precisely $Zn_{3.9-x}Sb_3$) exhibits an outstanding figure of merit between 450 K and 670 K with $ZT = 1.3$ at 670 K, owing to its exceptionally low thermal conductivity [1,38]. "Zn_4Sb_3" is polymorphic with two solid-solid phase transitions: $\alpha \leftrightarrow \beta$ over the 253-263 K temperature range and $\beta \leftrightarrow \gamma$ at ca. 763 K and melts congruently at 857 K [39–41]. Bokii and Klevtsova determined the crystal structure of the β-modification and determined the stoichiometry to be Zn_6Sb_5 [42]. Later, Mayer *et al.* [43] introduced and refined a Zn/Sb mixture on one of the two Sb sites to retain the initial Zn_4Sb_3 sample composition. Furthermore, it was shown by Tapiero [44] that Zn_4Sb_3 is zinc deficient and instable at elevated temperatures.

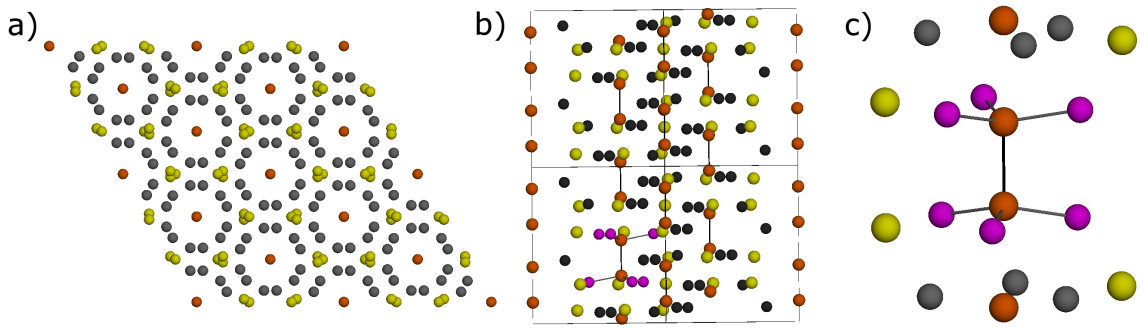

Figure 2.1: a) View along the [110] direction, b) view along [110], showing the channel-like structure of the Sb anions (yellow, orange), c) enlargement of one Sb_2 dumbbell (orange) showing the metaprism of Zn cations (purple).

Structure and precise stoichiometry of "Zn_4Sb_3" have been studied for decades [1,43, 45–53].

Common to all known phases in the phase diagram is a framework of isolated Sb^{3-} anions (yellow in figure 2.1) and $Sb_2{}^{4-}$ dumbbells (orange in figure 2.1), the latter being centered in a metaprism formed by six Zn cations (purple in figure 2.1 c). Apart from the high temperature γ-phase, all low temperature phases exhibit occupational disorder in the Zn partial structure and occupation of interstitials with decreasing level of order upon decreasing temperature. The amount of occupation of interstitials seems to be sample dependent, thus "Zn_4Sb_3" has become a generic term for the group of structurally comparable compounds $Zn_{6-\delta}Sb_5$ ($\delta = 0.62, 0.76$) [50], $Zn_{3.83}Sb_3$ [52], and $Zn_{84}Sb_{65}$ [51].

The proposed structures are variants of a Zn_6Sb_5 basis structure with structural disorder due to additional Zn interstitials and Zn vacancies [46–49, 52] and have been derived from comprehensive X-ray diffraction studies and analyses using maximum entropy methods. Recent Inelastic neutron scattering investigations relate the low thermal conductivity not to a phonon glass, but to a soft localized vibration of dumbbell Sb_2 units in the Sb sublattice [38, 53].

The structure of orthorhombic ZnSb was first reported in 1948 [54]. Zn and Sb show a five-fold coordination by one like and four unlike neighboring atoms (figure 2.2 a). One way to explain the structure is to focus on the planar rhomboid rings Zn_2Sb_2 (diamonds) containing the Zn-Zn contact as central building units [55]. Each of these diamonds is linked to 10 neighboring diamonds, figure 2.2 b) showing a layer of diamonds in the *ac* plane. In this layer each diamond is surrounded by six others, whereas two are attached to the Sb atoms and one to the Zn atoms. This leaves one coordination site per atom to bind diamonds in the b direction, two up and two down.

The thermoelectric properties of hot-pressed Zn_4Sb_3 and ZnSb samples at room temperature are compared in table 2.1.

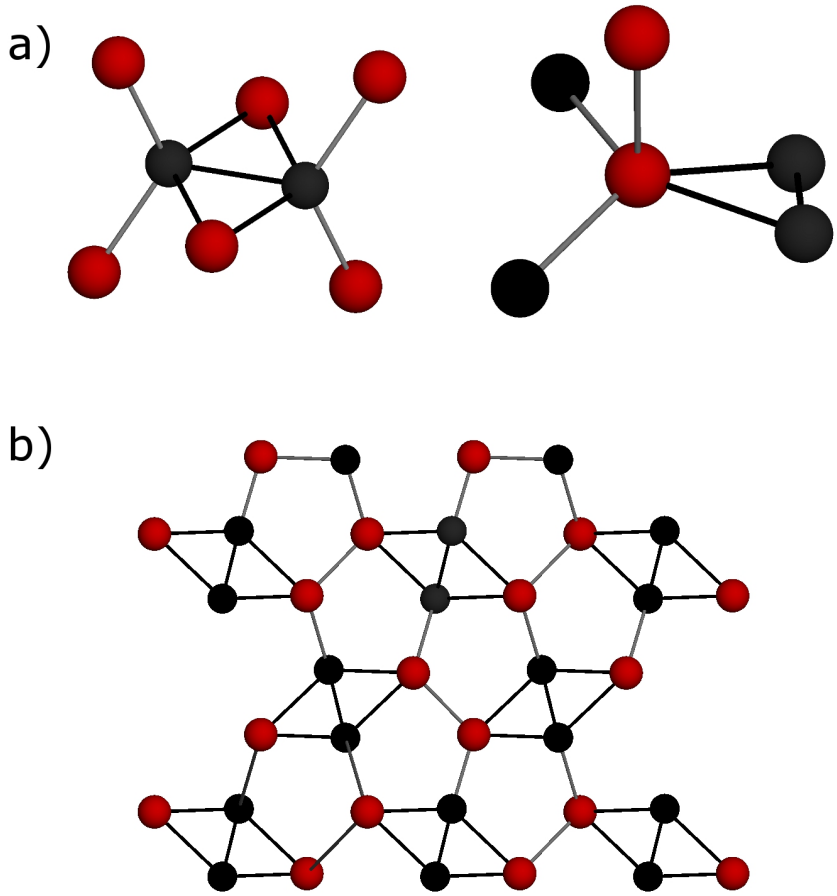

Figure 2.2: Crystal structure of orthorhombic ZnSb (Zn atoms in black, Sb atoms in red). a) Coordination environment of Zn (left) and Sb (right), b) layer of Zn_2Sb_2 diamonds in the *ac* plane.

Table 2.1: Thermoelectric properties of Zn_4Sb_3 and ZnSb at room temperature, adapted from [1–3].

Property	**Zn_4Sb_3**	**ZnSb**
Conductivity type	P	P
Electrical resistivity (Ωcm)	2.2×10^{-3}	1.1×10^{-3}
Hall mobility (cm^2/Vs)	32	94
Hall carrier concentration (cm^{-3})	6.8×10^{19}	6.3×10^{18}
Seebeck coefficient (μV/K)	113	196
Thermal conductivity (W/mK)	0.97	2.3
Lattice thermal conductivity (W/mK)	0.74	2.26

2.1.2 Fe-Sb system

The iron-antimony phase diagram shows two intermetallic phases: $Fe_{1+x}Sb$ and $FeSb_2$. $FeSb_2$ is a stoichiometric compound crystallizing in the marcasite crystal structure and decomposes peritectically into FeSb and an antimony rich liquid. The Fe atoms (gray in figure 2.3 a) are surrounded by six Sb atoms in form of a distorted octahedra (purple in figure 2.3 a), where two octahedra share an edge in the *ab*-plane (figure 2.3 b).

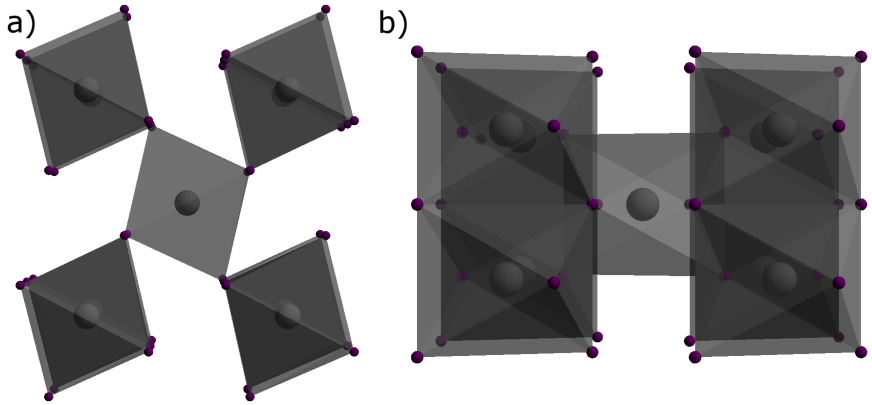

Figure 2.3: Crystal structure of orthorhombic $FeSb_2$ (marcasite structure type). a) Fe ions (gray) are surrounded by octahedra of Sb atoms (purple), b) edge sharing octahedra along c-axis.

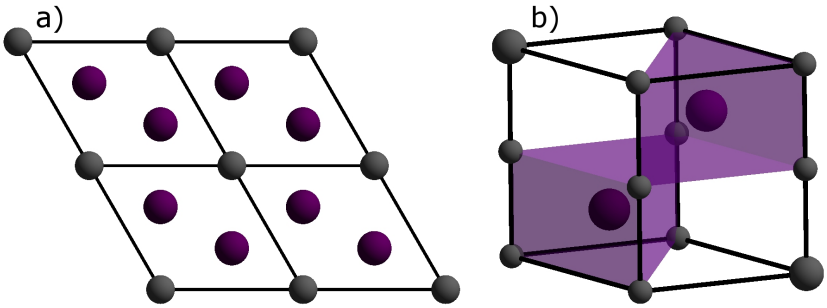

Figure 2.4: Crystal structure of FeSb (NiAs-type). a) Hexagonal crystal structure of FeSb, b) Sb anions (purple) are surrounded by a trigonal prism of Fe ions (gray).

FeSb is a nonstoichiometric compound crystallizing in the NiAs structure type (figure 2.4), better referred to as $Fe_{1+x}Sb$, which is characterized by a broad homogeneity range between about 40 and 47 at% antimony and by a congruent melting behavior [56]. The additional iron atoms occupy interstitial sites within the lattice. The compound has been investigated experimentally by a number of researchers [57–63], but their findings are quite divergent.

It has been shown that bulk $FeSb_2$ possesses a collosal Seebeck coefficient at temperatures below 0°C. Bentien *et al.* report a Seebeck coefficient of -45000 μV/K at 10K which results in the highest power factor ever reported [64]. $FeSb_2$ belongs to the class of strongly correlated semiconductors which consists of rare-earth and transition-metal compounds whose band gaps are believed to be a consequence of the hybridization between the local f- or d-band and the conduction band [65]. This results in narrow flat bands near the Fermi energy (see figure 2.5) which is responsible for a high effective mass, leading to high values of S.

In addition to a very high power factor, rather high values of the thermal conductivity are reported [66]. The question thus arises if the thermal transport can be reduced in nanostructured $FeSb_2$ without losing the high Seebeck coefficient and without decreasing the electrical conductivity.

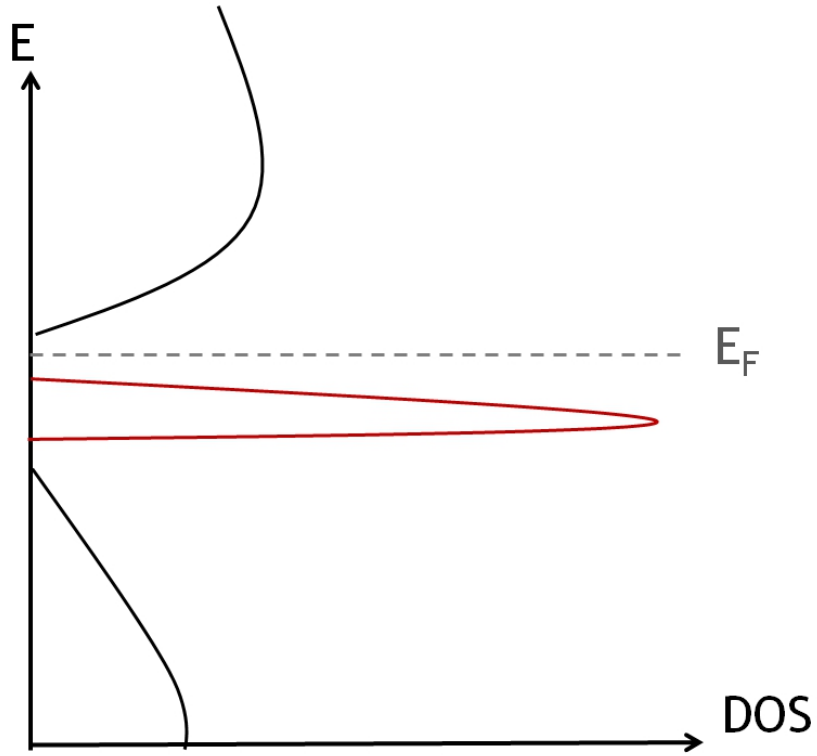

Figure 2.5: Narrow flat band (red) near the Fermi energy of a correlated semiconductor leading to a high Seebeck coefficient.

2.2 Processing of the powders

Thermoelectric modules require p- and n-doped legs consisting of dense materials. Since the described synthetic routes provide only loose powders, the products need to be solidified prior to any thermoelectric characterization. It will be shown that this densification step is far from being trivial and has a huge impact on the modules´ thermoelectric performance. Usually, materials are pressed into dense pellets through the conventional hot pressing technique. Thereby, the powder container is typically heated by radiation from the enclosing furnace through external heating elements. Thus, the sample is heated as a consequence of the heat transfer occurring by conduction from the external surface of the container to the powders. The resulting heating rate is slow and the whole densification process can last hours.

If nanoparticles are subjected to heat for a while they will start sintering together and building larger crystals. This growth will result in a bulk material eventually. Therefore, one needs to apply a pressing technique which will not destroy the nanostructure of the synthesized samples.

In our studies, Spark plasma sintering was used for the densification of the obtained powders. This process is shown schematically in figure 2.6 and simultaneously applies an electric current along with a mechanical pressure to consolidate powders or synthesize and densify specific products. This technique is characterized by application of the pulsed electric current on the graphite container acting as a heating element, leading to a very rapid and efficient heating. Heating rates of as high as 1000°C/min can be achieved reducing the processing times to fractions of seconds or minutes. This holds the advantage that nanoparticles sinter together only at common interfaces without coalescence to bigger crystallites.

Moreover, the SPS process uses input heat efficiently and is energetically favorable to conventional hot pressing techniques which apply heat for a long period of time.

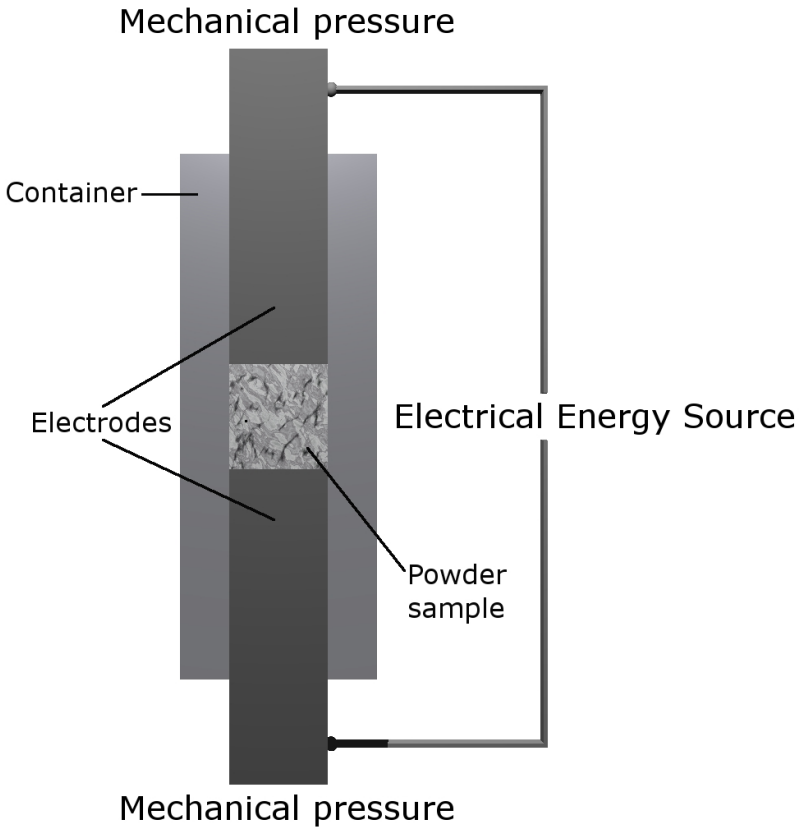

Figure 2.6: Schematic representation of the Spark plasma sintering process, the setup is placed into a vacuum chamber, adapted from [67].

Spark plasma sintering (SPS) theory is discussed to be based on an electrical spark discharge phenomenon wherein a high energy pulse current momentarily generates spark plasma at high localized temperatures (up to 10.000°) between particles [67]. The spark energy vaporizes contaminants and oxidation on the surface of the particles prior to neck formation. Joule heat is concentrated on particle surfaces producing plastic deformation which aids in high density applications.

2.3 Characterization of the compounds

All compounds shall be characterized structurally by powder X-ray diffraction before and after sintering, whereas different techniques and instruments can be used. Appearance and size of the as prepared nanoparticles as well as surface morphology of the densified samples will be determined by Laser microscopy and Transmission- and Scanning electron microscopy, respectively.

Due to the nanostructuring of the particles, broad X-ray diffraction profiles are to be expected. In order to obtain more detailed insight into the obtained sample compositions, additional characterization techniques shall be applied. A rather new electron diffraction method, Automated diffraction tomography (ADT), shall be performed on some of the nanoparticle systems. The iron-containing samples will also be investigated by ^{57}Fe-Mößbauer measurements. In comparison to XRD measurements, this technique is not only sensitive to crystalline components but to all species which contain iron.

Lattice dynamics are to be investigated by heat capacity measurements and Nuclear inelastic scattering investigations.

A key requirement for thermoelectric measurements is mechanical strength since the workpieces will have to be cut into a bar and have to be contacted. The thermoelectric properties shall be determined accordingly.

2.4 Collaborations within the SPP 1386

Within the SPP 1386 on nanostructured thermoelectrics, different collaborations are conducted.

The solidification by Spark plasma sintering is performed by [redacted] at the Fraunhofer Institute (Fertigungstechnik und Angewandte Materialforschung IFAM) in Dresden.

The study of the lattice dynamics of the nanostructured materials, whose results are summarized here, is the subject of the thesis of [redacted] from the Forschungszentrum Jülich and Université de Liége.

^{57}Fe-Mößbauer measurements are performed by [redacted]

Seebeck mapping is performed by [redacted]

Seebeck coefficient, electrical and thermal transport are measured by [redacted]

Chapter 3

Solution synthesis of a new thermoelectric $Zn_{1+x}Sb$ nanophase and its structure determination using Automated electron diffraction tomography

3.1 Introduction

The interdependency of transport properties in the thermoelectric efficiency makes the engineering of thermoelectric materials a difficult task. However, the physics of nanostructures allows varying S, σ and κ independently, thus enhancing ZT under appropriately selected conditions.

From a synthetic point of view, it is crucial to control the nanostructure and morphology of these complex binary materials and their performance in potential thermoelectric applications.

Controlling nanostructure and morphology is important, as they are critical for the intended applications.

Intermetallics are typically made at high temperatures (usually $\geq 1000°C$) with long annealing times (often days or weeks). Due to the intrinsically metastable nature of nanoscale matter, we have devised a low-temperature synthetic route for "Zn_4Sb_3" nanoparticles, where weakly stabilized Zn and Sb nanoparticles aggregate to form binary nanocomposites [68] reacting subsequently to form intermetallic nanocrystals. The synthesis can be scaled up to yield bulk amounts of material. The novel solution-based approach uses activated metal nanoparticles as precursors for the synthesis of a $Zn_{1+x}Sb$ nanophase, containing ZnSb and a new binary phase $Zn_{1+\delta}Sb$, segregated from a nano-Zn_4Sb_3 precursor in a peritectoid reaction.

Traditional single crystal X-ray diffraction techniques cannot be applied to nanostructures. Powder X-ray analysis meets serious problems when the size of the crystals is below 50 nm and different phases are present in the sample, all attributes of the Zn-Sb system. Therefore, the crystallographic investigation was performed using electron diffraction. In contrast to X-rays, an electron beam can be focused on a very small area allowing the selection of a single nanocrystal of only a few nanometers. As scattering factors for electrons are significantly higher in comparison to X-rays, diffraction information with a reasonable signal-to-noise ratio can be collected even from such small volumes.

Two types of problems are usually attributed to electron diffraction data, which diminishes its usability for structure solution: electron diffraction data often miss a sufficient number of reflections and the intensities of the reflections are strongly modified due to dynamical effects.

In order to overcome these problems and to develop a well established routine for electron diffraction data collection, techniques like Automated diffraction tomography (ADT) [69, 70], and Precession electron diffraction (PED) [71–73] have been developed in the last years.

By combining these two techniques, a rich sampling of the reciprocal space can be achieved and thus almost complete quasi-kinematical electron diffraction data sets can be collected. Mugnaioli *et al.* [74] demonstrated that this method, comprising basically the 3D reconstruction of the reciprocal space with quasi-kinematically data, allows solving inorganic structures *ab initio* in one step. This data collection/structure solution strategy was applied to the $Zn_{1+x}Sb$ nanophase containing a known ZnSb phase and a hitherto unknown $Zn_{1+\delta}Sb$. Both phases were identified by electron diffraction and high-resolution TEM imaging, and *ab initio* structure determinations were performed using combined ADT/PED.

3.2 Results and discussion

3.2.1 Synthesis

$ZnCl_2$ (anhydrous, 98%, ABCR) was first dried with thionylchloride, washed with toluene, dried *in vacuo* and stored in a glovebox under N_2 atmosphere. Tetrahydrofuran was dried with $CaCl_2$ and Na/K and freshly distilled before use. Lithium triethylboronhydride Li[Et_3BH] (Aldrich, 1 M in THF, referred to as "superhydride"), and $SbCl_3$ (99%, ABCR) were used as obtained, $SbCl_3$ was stored in a glove box. Trioctylamine (Aldrich) was degassed and stored under Ar before use.
Zn particles were synthesized by reaction of $ZnCl_2$ with 2 equivalents of the 1 M solution of "superhydride" in THF at ca. 65°C. The particles were washed several times with THF, dried *in vacuo* and stored in a glovebox. Sb particles were produced by reducing $SbCl_3$ with 3 equivalents of the 1 M "superhydride" solution at room temperature. The black particles were repeatedly re-dispersed in THF and decanted from the solution, dried *in vacuo* and kept in a glove box.

Both, Zn and Sb nanoparticles, are highly reactive in ambient air leading primarily to the oxides. ^{1}H NMR data of Sb nanoparticles kept in inert gas atmosphere show an intense signal according to surface bond stibane ($\delta \approx 1.05$ ppm, c.f. figure 3.1) which broadens, when the particles were in contact with air.

The activated elements were heated to 300°C at a rate of ca. 20 K/min in a polar strongly coordinating solvent (trioctylamine) in order to prevent nanoparticle aggregation. Products were collected by centrifugation, washed with ethanol and subsequently dried *in vacuo*.

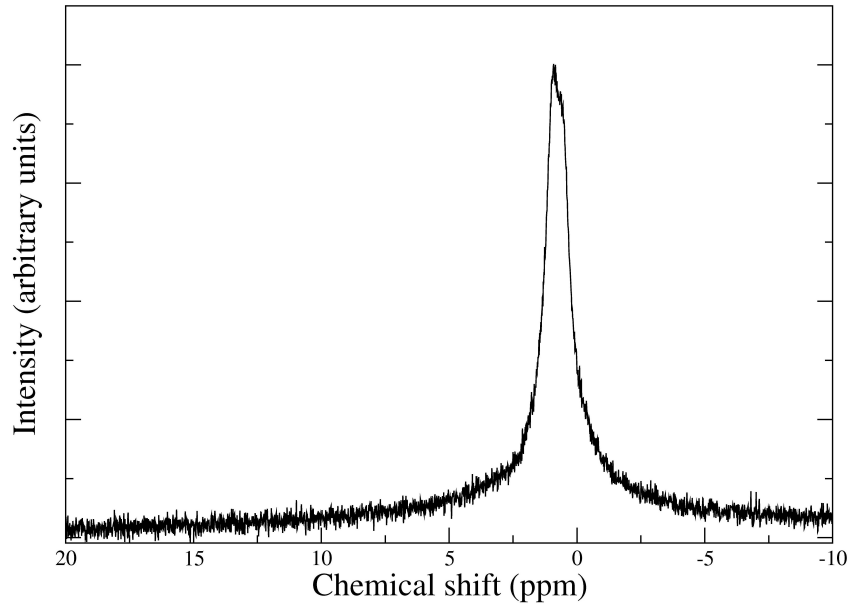

Figure 3.1: ^{1}H-NMR data of Sb nanoparticles prepared in a glovebox.

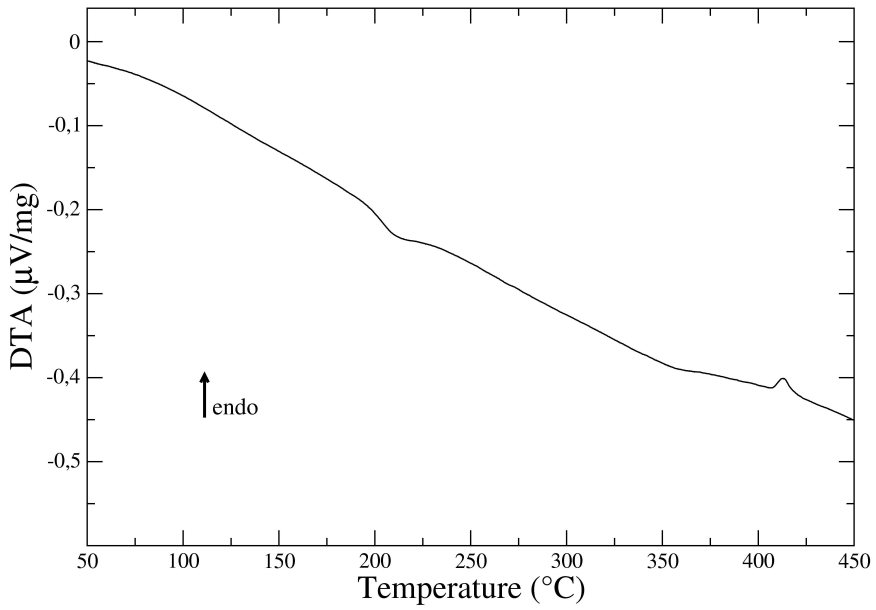

Figure 3.2: DTA data of the $Zn_{1+x}Sb$ sample showing the exothermic decomposition of the $Zn_{1+\delta}$ phase (ca. 200°C) and the endothermic melting of Zn (ca. 410°C).

The syntheses had to be carried out using an excess of zinc metal which is removed after reaction by repeated treatment of the solid residue with dilute acetic acid.

Prior to heating, both Zn and Sb were crystalline, and the XRD pattern matched that expected for a superposition of both elements. After several minutes of heating at 300°C, the intermetallic compound ZnSb was formed; further heating increased its crystallinity. The product is stable in air at least over the period of several months. Combined TG/DTA of the product (see figure 3.2) in the range from ambient temperature to 450°C showed an exothermic effect at 200°C corresponding to the peritectoid decomposition of $Zn_{1+x}Sb$, forming ZnSb and Zn. Upon further heating, the melting of Zn (ca. 410°C) was observed, while only a minor weight loss occurred.

It was observed that the size of an "activated" metal particle is crucial for the outcome of the reaction. In conventional high-temperature reactions the energy required for the solid state diffusion of the reactants would exceed the nucleation energy of metastable phases. In contrast, reactions, in which solid state diffusion plays only a minor role, are kinetically controlled, and a phase may nucleate and grow until its growth exhausts the supply of the reactants. The sequence of phases formed depends upon the relative activation energies for nucleation of the various compounds, and compounds in the equilibrium phase diagram may be temporarily skipped if they have large activation energy for nucleation.

The size of the "activated" metal particles allows for a reaction with minimum solid state diffusion, low activation barriers, and low reaction temperatures, thereby eliminating solid-solid diffusion as the rate-limiting step in conventional bulk-scale solid-state synthesis.

It follows the strategy proposed by Johnson *et al.* [75,76] on elementally modulated thin films that was utilized later for the synthesis of fullerene-type chalcogenide nanoparticles [77] or in the so-called polyol synthesis for nanoparticles of noble metals [78] and intermetallics [79]. The nanosize dimensions support low-temperature diffusion without the high-temperature melting step that is necessary in traditional metallurgy.

Clearly, nanoscale intermixing of pre-reduced metal particles significantly increases the reaction kinetics relative to conventional high-temperature syntheses involving micrometer-sized powders. Likewise, the solvent confines the crystallite size to nanoscale dimensions, allowing atomic ordering to occur rapidly without long-term annealing.

3.2.2 X-ray diffraction

X-ray powder diffraction profiles recorded from reaction intermediates after specified time intervals (figure 3.3) revealed that ZnSb was formed within 1 h. From the X-ray powder data it was evident that the primary product transformed into a new phase with cell parameters geometrically related to those of "Zn_4Sb_3" in the subsequent reaction steps. The data collected after reaction intervals of 2 h and 3 h indicated the formation of a mixture of ZnSb and nominal "Zn_4Sb_3", which was the major product when the reaction was complete after 3 h 45 min.

Upon further heating a re-formation of ZnSb due to decomposition of "Zn_4Sb_3" (mostly into Zn) was observed (figure 3.4). If the amount of Zn was less than a 9-fold excess, the major product of the reaction was ZnSb instead of "Zn_4Sb_3".

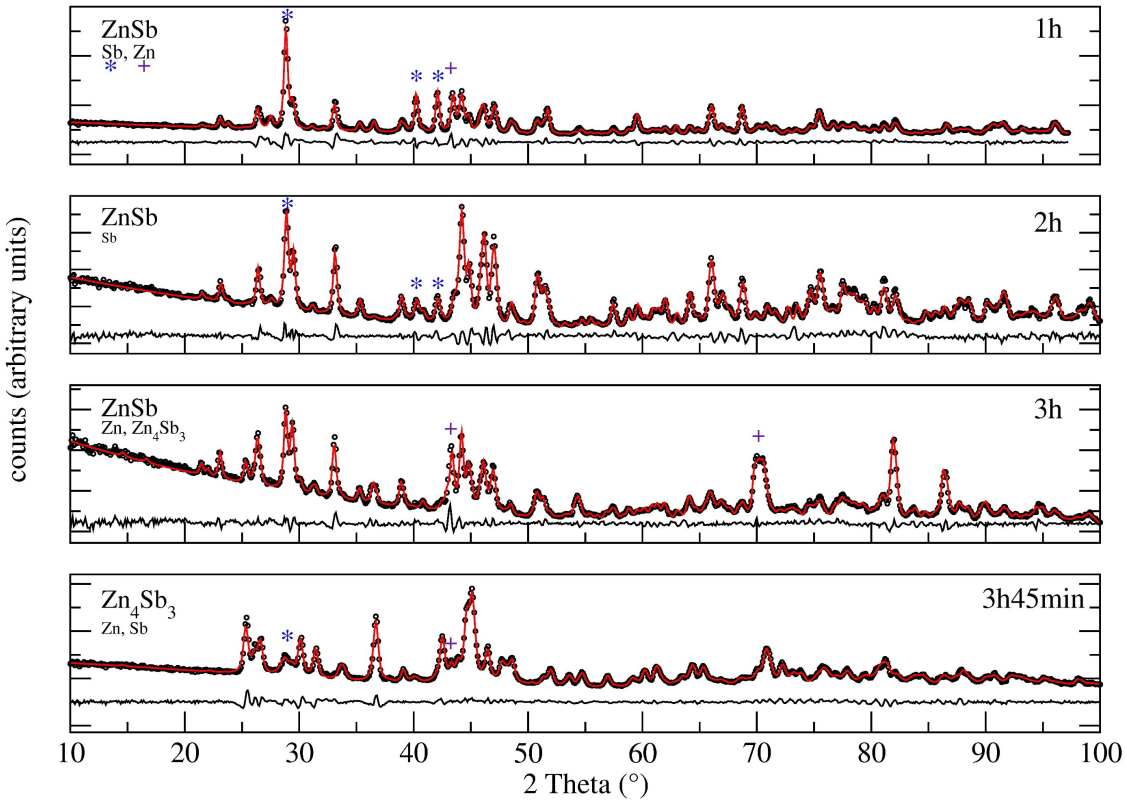

Figure 3.3: Time-dependent (ex situ) X-ray diffraction (experimental data: black circles), le Bail fits (red line) and corresponding difference plots (black line) after reaction times of 60, 120, 180 (as prepared) and 225 min (after two washing cycles with dilute acetic acid).

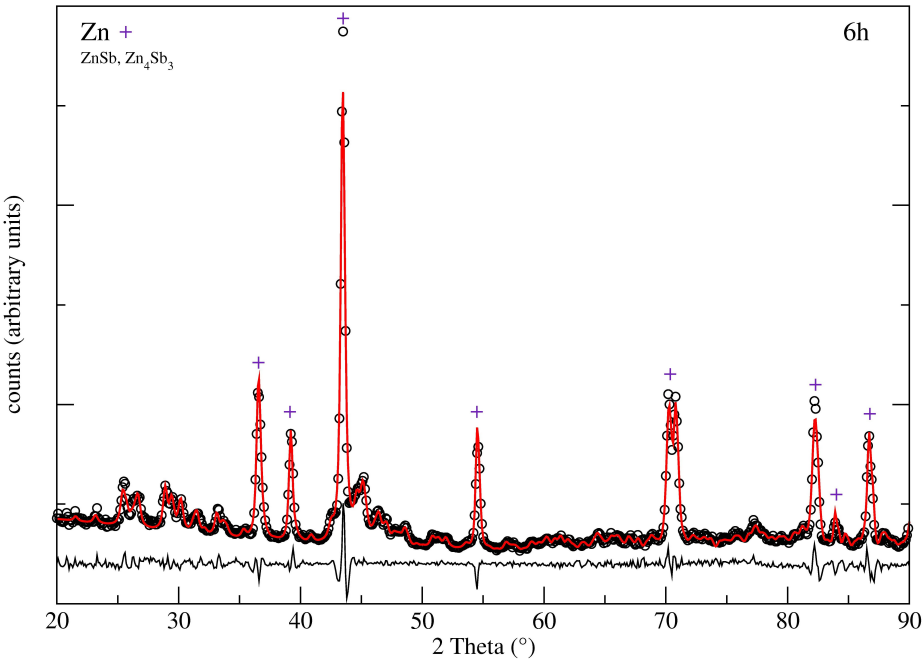

Figure 3.4: X-ray diffraction (experimental data: black circles), le Bail fits (red line) and corresponding difference plots (black line) of product (after two washing cycles with dilute acetic acid) after 6 h reaction time.

All diffraction profiles included reflections of metallic Sb and Zn (marked in figure 3.3 by blue stars and magenta crosses, respectively). The final product obtained after 225 min contains only minor amounts of these impurities. The powder patterns of all crystalline phases were refined using le Bail fits with lattice cell parameters of ZnSb and Zn_4Sb_3 [48]. The fitting of the final product was carried out using the crystallographic data of Zn_4Sb_3 and gave an almost straight difference curve indicating that there are no further crystalline impurities. The crystallite size of the "Zn_4Sb_3" nanoparticles as determined from the refinement was approx. 30 nm.

3.2.3 TEM overview

In all TEM investigations the samples proved to be extremely stable, i.e. no alteration was observed either in short term or after hours of data acquisition. TEM images as well as SEM images show that both, the intermediate and the final products, consist of porous agglomerates built of tens to hundreds round particles (figures 3.5 and 3.6) with diameters between 5 and 70 nm. The mean particle size determined from TEM is therefore in harmony with the crystallite size obtained from the powder X-ray studies. Despite intensive sonication during TEM sample preparation, individual crystals were never observed and even the smallest aggregates consisted of several crystals (figure 3.7).

HRTEM images of the final $Zn_{1+x}Sb$ nanophase demonstrated that all particles but the smallest contain a crystalline core surrounded by an amorphous shell of 3-10 nm (figures 3.9 and 3.8). Although the sample crystallinity judged from the powder X-ray profiles did not differ much for the products after different reaction times, HRTEM imaging showed that the final product has significantly higher crystallinity.

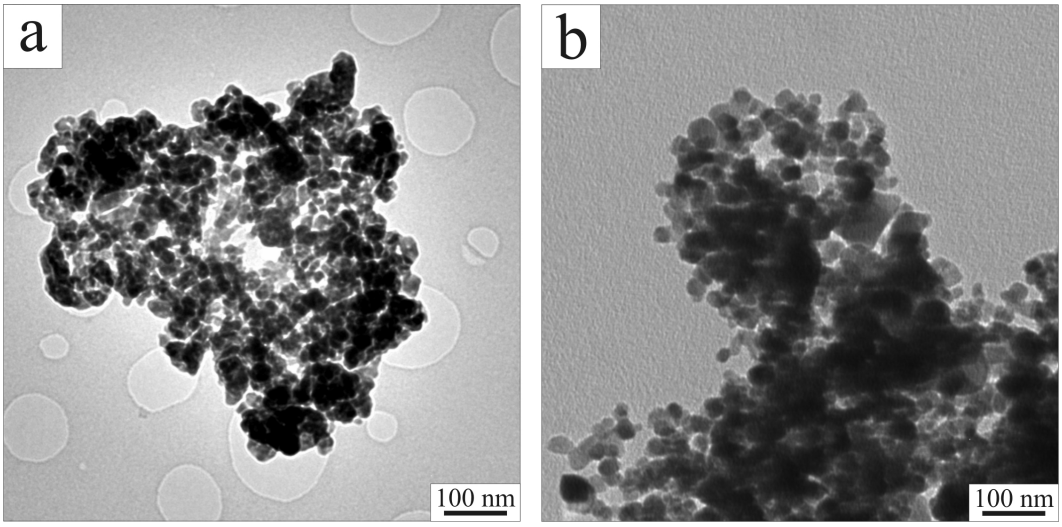

Figure 3.5: Overview TEM images of typical aggregates obtained after (a) a reaction time of 1 h and (b) the final product after 3 h 45 min.

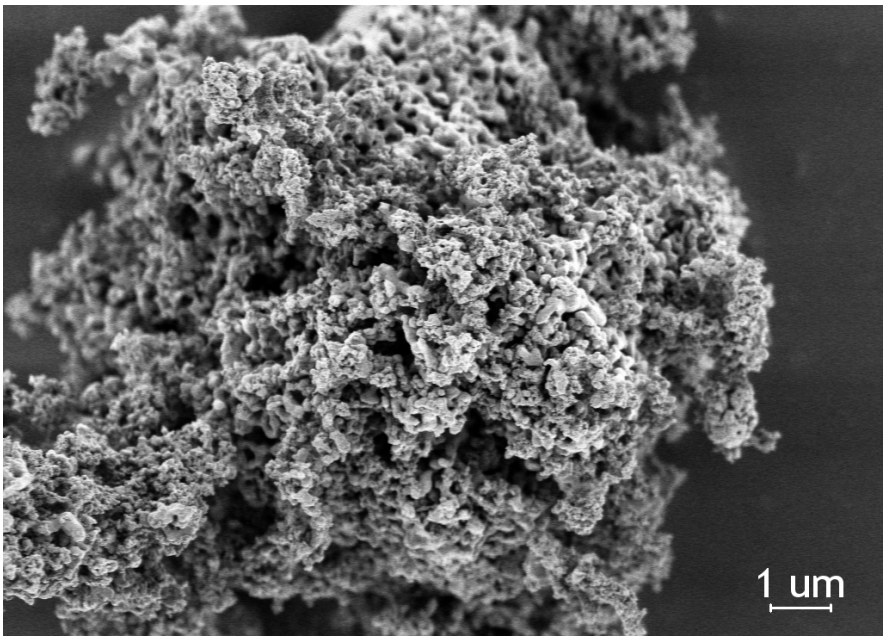

Figure 3.6: SEM overview image of $Zn_{1+x}Sb$.

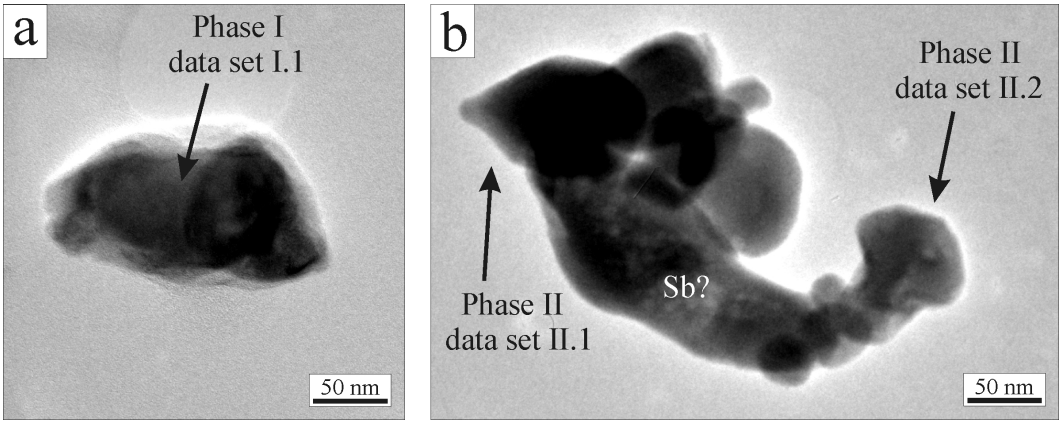

Figure 3.7: Small aggregates used for ADT data collections. a) Data for structural analysis of phase I was collected from the middle part of the agglomerate, b) two data sets for structural analysis of phase II were collected from crystals indicated by arrows. In the middle part of this aggregate diffraction patterns with interplanar distances of 11.2 Å were observed, likely due to the presence of metallic Sb.

High-resolution TEM measurements of the final product as well as electron diffraction patterns clearly revealed the presence of a crystallographic phase different from any known "Zn_4Sb_3" phase. Although powder X-ray profiles could be fitted using the crystallographic data of Zn_6Sb_5 [48], TEM delivered a pseudo-hexagonal lattice and interplanar distances which could not be described by any known phase. Obviously, the lattice parameters of the new phase should be strictly geometrically related to Zn_6Sb_5. The cell volume of the new phase, calculated by high order Laue zones (figure 3.8), is approximately 1630 $Å^3$. EDX analyses of multiple regions of the samples confirm that Zn and Sb are present in an approximate 1:1 atomic ratio with a slight excess of Zn (53% Zn, 47% Sb; figure 3.10).

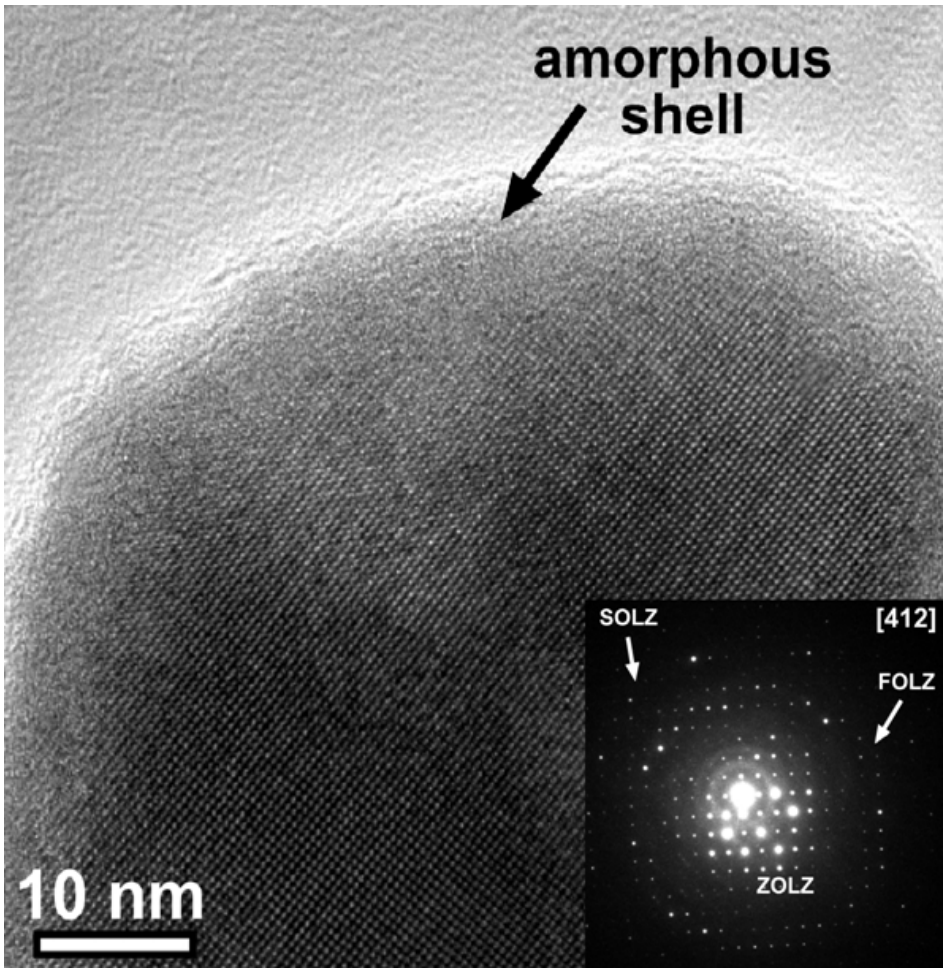

Figure 3.8: HRTEM image of a $Zn_{1+x}Sb$ nanoparticle not oriented along a main axis and corresponding nano electron diffraction pattern, in which high order Laue zones (HOLZ) are visible. ZOLZ, FOLZ and SOLZ are abbreviations for zero-order Laue zone, first-order Laue zone, second-order Laue zone, respectively.

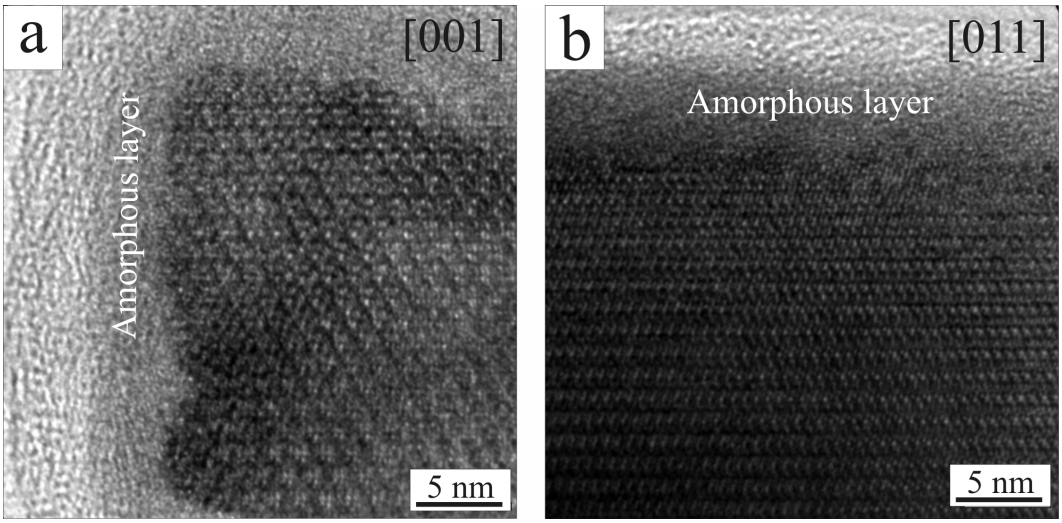

Figure 3.9: HRTEM images of $Zn_{1+\delta}Sb$ nanoparticles viewed along (a) the [001] and (b) the [011] directions.

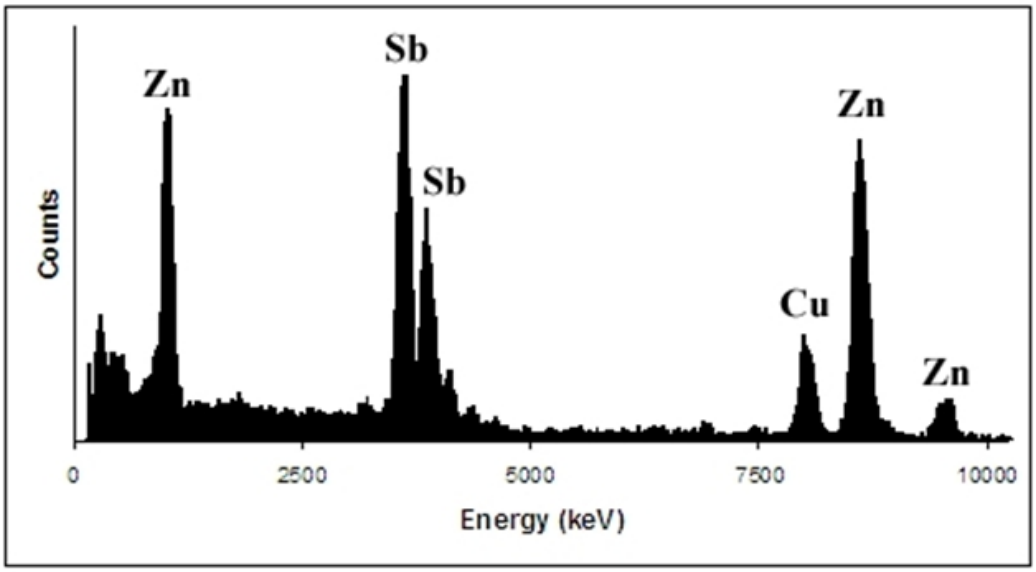

Figure 3.10: EDX data of $Zn_{1+\delta}Sb$.

Table 3.1: Crystallographic data of the two different crystalline phases.

		ZnSb		**$Zn_{1+\delta}Sb$**	
Cell parameters	**ADT**	**refined XRPD**	**[48]**	**ADT**	**XRPD**
Space group		*Pbca*		*P-1*	
a (Å)	6.46	6.54	6.20	15.31	15.25
b (Å)	8.11	8.06	7.74	15.51	15.72
c (Å)	8.43	8.31	8.10	7.81	7.81
α (°)	89.31	90	90	88.87	90
β (°)	89.86	90	90	89.42	90
δ (°)	89.38	90	90	119.4	120

3.2.4 Electron crystallography by ADT

For structural investigations ADT data were collected from prominent crystals in relatively small aggregates (figure 3.7) using an electron beam with 50 nm diameter (for details see [69, 70]). 3D reconstruction of the reciprocal space for different crystals showed unambiguously that the sample consisted of at least of two different phases. While the first phase had an orthorhombic cell (phase I), the second one showed a lattice with *pseudo*-hexagonal metric (phase II). Approximate average compositions determined from EDX spectra did not allow an unambiguous determination of the two phases, as for both the Sb:Zn ratio was close to 1:1.

Figure 3.11 shows projections of the reconstructed reciprocal volume from ADT data for orthorhombic phase I. The unit cell parameters agree well with the known structure of ZnSb (table 3.1) [48]. The systematic extinctions are compatible with the space group *Pbca*. Lattice parameters determined directly from ADT data, as well as subsequently refined against powder X-ray diffraction data, are approximately 4% larger than those reported for the ZnSb bulk phase.

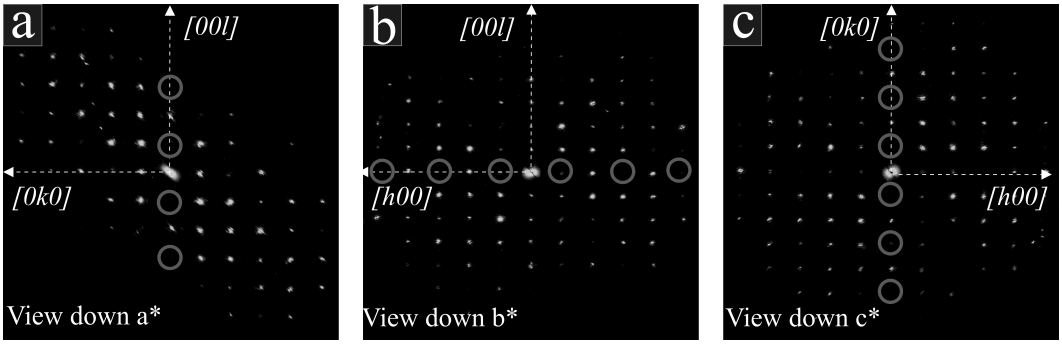

Figure 3.11: Projections of the full 3D reciprocal space for the orthorhombic phase I of the dataset I.1 exhibiting the systematic extinctions of space group *Pbca* (see comment). The volume was visualized using ADT-3D package applying volume rendering technique with manually determined opacity transfer functions.

Please note: These are full 3D projections of the reciprocal space, but not individual layers of the reciprocal space. In the latter, serial and zonal systematic extinction will be identified by extinct intensities along one reciprocal axis and one full reciprocal plane, respectively. In full 3D projections serial extinctions cannot be identified in principle. Zonal extinctions are identified as systematic extinctions along one line perpendicular to the corresponding reciprocal axis, e.g. the *c*-glide-mirror plane perpendicular to the real space axis *b* in space group *Pbca* is identified from systematic absences along the reciprocal axis perpendicular to b^* i.e. [00l] (see circles in figure 3.11).

The most important information about the ADT data set used for structure analysis of phase I is compiled in table 3.2. The structure was solved *ab initio* in one step using direct methods implemented in SIR2008 [80] from ADT data without electron beam precession (figure 3.12).

Table 3.2: Summary of the ADT data sets employed for structure determination.

	ZnSb	**$Zn_{1+\delta}Sb$**	
Data set	I.1	II.1	II.2
Data type	ADT	ADT + PED	ADT + PED
Tilt range	60°	76° + 76°	90°
Total reflections	388	6271	4486
Independent reflections	106	3651	2745
Resolution (Å)	1.1	0.8	0.8
Reflection coverage, %	70	57	44
R_sym, % of the data set	30.60	16.86	17.45
U isotropic (Å^2)	0.037	0.030	0.031
Final R, %	27.10	36.19	42.52

A fully kinematical approach was used (intensities proportional to ${F_{hkl}}^2$), and no correction was applied to the data. Four potential peaks were identified by the program. The most intense peak (the height of 1596) was assigned to a Sb atom; the second peak (the height of 910) was assigned to Zn. The ratio between the heights of these two peaks corresponds nicely to the ratio between the atomic numbers of the two atoms 51:30, which in turn reflects the maximal amplitudes of the scattering factors for electrons. The other two peaks found by SIR2008 were much lower (305 and 300), and therefore were treated as ghosts. The structure model exhibits a close match to the known crystal structure of ZnSb [48] with the errors in atomic positions of 0.02 Å for Sb and 0.05 Å for Zn.

Main projections of a 3D reconstructed data set recorded for phase II ($Zn_{1+\delta}Sb$) are shown in figure 3.13 a-b). The corresponding lattice parameters are listed in table 3.1. ADT data confirms that the cell parameters did not match those of any known Zn-Sb phase, even if the new phase has to be strictly geometrically related with rhombohedral Zn_6Sb_5 [48]. No systematic extinction was detected.

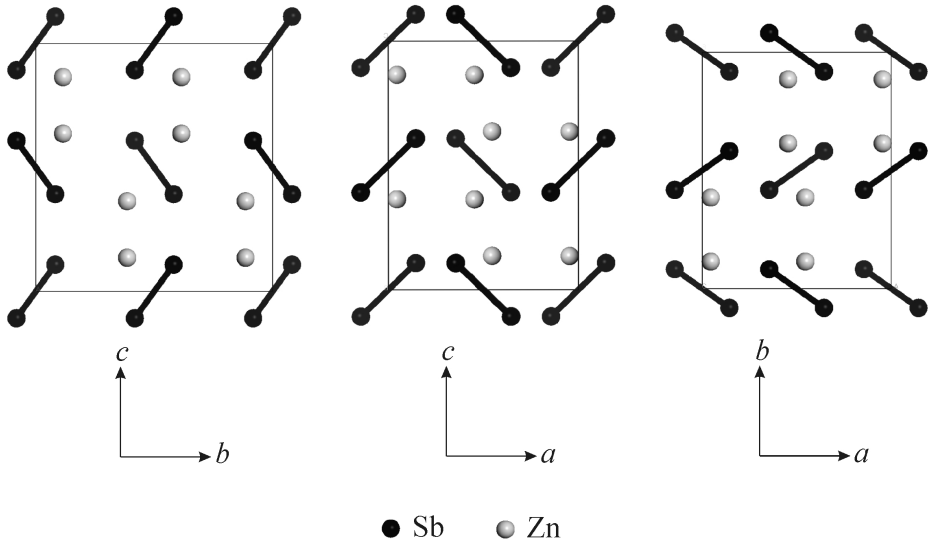

Figure 3.12: ZnSb structure determined by SIR2008. The Sb_2 dumbbells are connected.

The lattice parameters obtained from electron diffraction allowed reasonable le Bail fitting of the powder X-ray diffraction profile, taking into account impurities of Sb and ZnSb (table 3.1).

In order to determine the correct crystal system for phase II, single zone diffraction patterns taken at optimized electron beam precession conditions were recorded (figure 3.13 c-d). Both, zone [100] and zone [001], exhibit strong *pseudo*-symmetry. However, a careful inspection of the [100] zone shows that the only true symmetry element present is the inversion center (due to Friedel's law). Figure 3.13 e) shows an intensity scan along the row marked in figure 3.13 c) by dotted arrows: these reflections do not have mirror symmetry along the [010] direction. The [001] zone shows no mirror symmetry (figure 3.13 f) and a careful analysis of prominent spots, as for example (400), (040), and (-440), leads to an exclusion of a 3-fold axis. Therefore, the true zone symmetry is inversion only and the structure is triclinic.

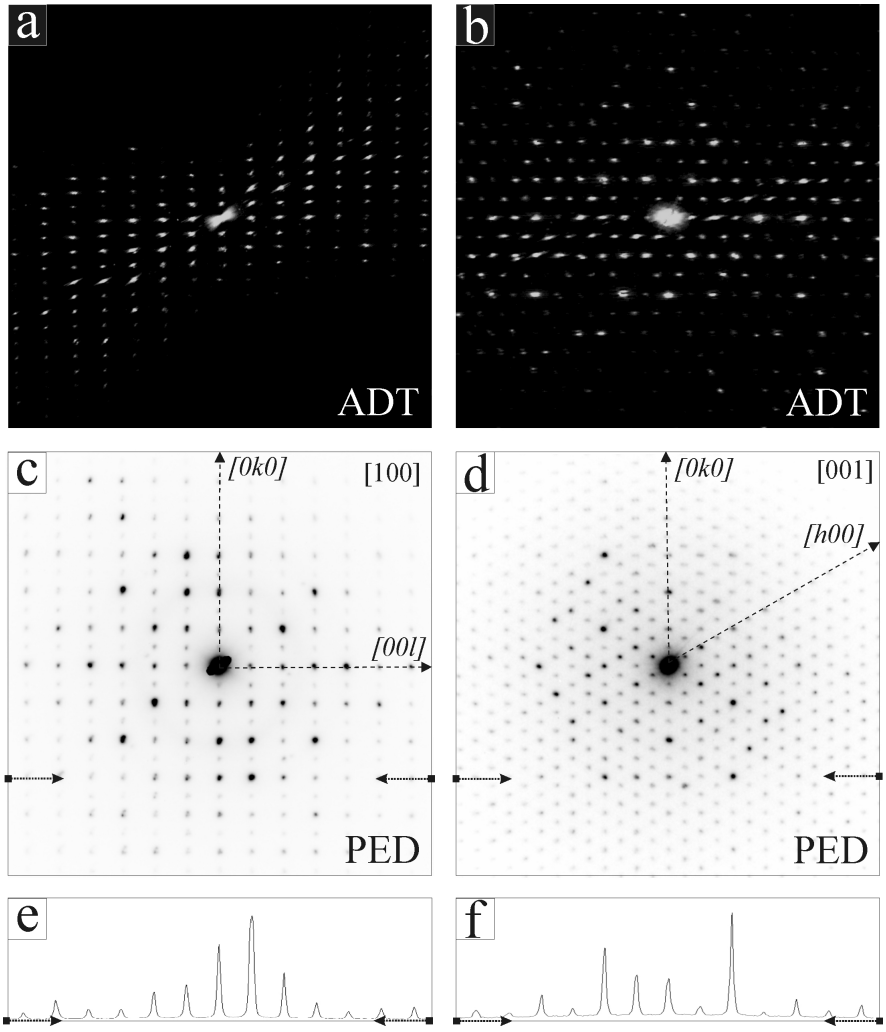

Figure 3.13: Electron diffraction data for phase II ($Zn_{1+\delta}Sb$): a) projection of the reconstructed reciprocal space along the a* direction, b) projection of the reconstructed reciprocal space along the c* direction, c) single PED pattern zone [100], d) single PED pattern zone [001], e+f) intensity scans of patterns shown in c) and d) (line marked by arrows).

For structure analysis of phase II two independent tilt series were collected. The first crystal was tilted in a range of 76°, rotated in-plane by approximately 90° and tilted again by 76° collecting an additional tilt series in the same tilt range. These two tilt series acquired from the same crystal were subsequently merged (merging factors 1 to 1) and gave data sets II.1 (table 3.2). The second data set II.2 was collected from another crystal within a tilt range of 90° (table 3.2). The diffraction camera length was reduced in order to achieve a resolution of 0.8 Å. Both data sets include around 3000 independent reflections.

For phase II, structure solution by direct methods based on standard ADT data did not result in a chemically meaningful structure model. ADT-PED coupled data set should be superior for structure solution [74] therefore as a next step these data were tried.

Indeed, a first solution in space group $P1$ converged to a reasonable structural model in one step. A check of the atomic positions displayed immediately the presence of an inversion center in the structure. This additional symmetry element was also evident from the correlation coefficient matrix in the initial structure model refinement. Therefore the structure was finally solved in space group $P\text{-}1$. A fully kinematical approach was used and no correction was applied to the data set.

The correct solution was well recognizable as it exhibited by far the lowest final residual factor and the highest figure of merit at the same time. The first 30 maxima in the electron density map determined by SIR2008 [80] showed reasonable interatomic distances. The 14 strongest maxima were attributed to Sb and the remaining 16 to Zn. The structure was subsequently refined using SHELXL97 [81], showing an appreciable stability without any constraints.

The final refinement converges at R = 0.362 and 0.425 for data I and II respectively, which is in the typical level of quality for crystal structure analysis by ADT and electron diffraction in general [74].

As the "Zn_4Sb_3" compounds are known to exhibit occupational disorder of the Zn partial structure, the atomic occupancies for all atoms were tentatively refined based on the available electron diffraction data. Even if the reliability of site occupation factors derived from electron diffraction data is a subject of discussion, values significantly lower than 1 are usually taken as a hint towards occupational disorder [82]. Taking into account the partial occupancies the final stoichiometry of $Zn_{1+\delta}Sb$ phase is $Zn_{28.1}Sb_{26.3}$. A full occupancy of the positions results in a density of 5.63 g/cm^3, which is in a good agreement with the density of 5.68 g/cm^3 calculated for the orthorhombic ZnSb phase. If the refined occupancies are taken into account the density drops to 5.10 g/cm^3. A possible explanation is that the vacancies are partially compensated by interstitials as often found for such compounds [48]. Final residual electron density maps still displayed intermediate to weak maxima which point to further Zn positions. Yet, within the given level of detail of electron diffraction an expansion of the structure model, taking these maxima into account would not be appropriate. Albeit the occupational disorder of the Zn partial sub-structure, the isotropic displacement factors were refined stable and exhibited reasonable values (table 3.3).

In order to confirm the above model, the second ADT+PED data set II.2 was analyzed using the same routine. The result confirms the structure model described above. The maximal difference of the atomic positions was 0.41 Å, the average difference was 0.18 Å.

Table 3.3: Atomic coordinates of Zn and Sb for ZnSb obtained using non-precessed electron diffraction data versus expected positions.

Present study	**x**	**y**	**z**	**U isotropic (Å^2)**
Sb	0.145	0.082	0.108	0.08
Zn	0.454	0.115	0.864	0.11
Ref. [48]				
Sb	0.1416(2)	0.0822(2)	0.1090(2)	
Zn	0.4580(3)	0.1104(2)	0.8673(4)	

3.2.5 Crystal structure of $Zn_{1+\delta}Sb$

Projections of the crystal structure are presented and compared with $Zn_{13}Sb_{10}$ [50] in figure 3.14. Single zone diffraction patterns of phase II (figure 3.11 c+d) show a strong superstructure imprint with hexagonal symmetry. In fact, the Sb substructure displays $6/m$ symmetry with all Sb placed on special positions according to the 2e, 2d, 6i, 6j, 6j, 6k Wyckoff sites of space group $P6/m$. The Zn sub-structure reduces the symmetry of the complete structure to -1. Yet, parts of the Zn substructure exhibit some higher symmetry: i.e. some of the non symmetry equivalent coordination polyhedra are very similar. For example, the polyhedrons in the middle row arranged along [010] show very similar organization (c.f. figure 3.14 a). This result is quite impressive as no specific symmetry constraints were imposed during the structure model refinement.

The structure can be classified within the Zintl-Klemm concept [83–85]. Antimony being more electronegative than Zn forms two types of anions: isolated Sb^{3-} anions, and $(Sb_2)^{4-}$ dumbbells (molecule-anions). The Sb^{3-} anions (Sb1, Sb2, Sb3, and Sb7) in $Zn_{1+\delta}Sb$ form a flat hexagonal net at z = $\frac{1}{2}$ with the distances of 4.4-4.6 Å between the nodes (figure 3.15). This net is placed at $\frac{1}{2}$ height of the unit cell (in [001] direction). The remaining Sb species belong to two different kinds of $(Sb_2)^{4-}$ dumbbells.

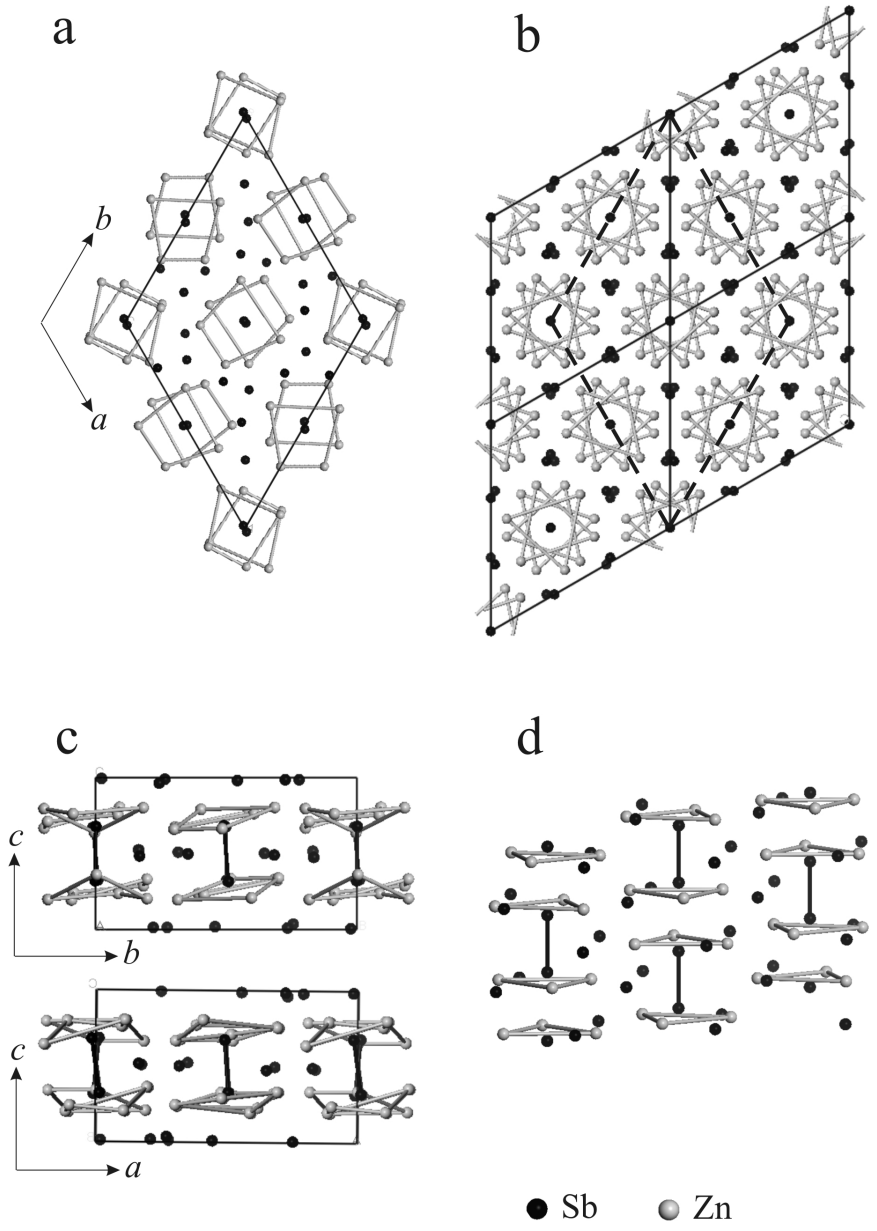

Figure 3.14: Relation between the crystal structure of $Zn_{1+\delta}Sb$ and $Zn_{13}Sb_{10}$ [50]. a) [001] View of the structure solved in the previous work, b) [001] view of the $Zn_{13}Sb_{10}$, c) coordination motives of the found structure d) coordination motives of the $Zn_{13}Sb_{10}$.

The first ones are those aligned in [001] direction and placed with the centers of gravity at virtually the same height as the hexagonal net (figure 3.15 b). These antimony species are located at four corners of the unit cell (Sb9), at four faces (Sb6, Sb8), and in the center (Sb10). In total there are four $(Sb_2)^{4-}$ dumbbells of this kind (figure 3.15 b). The second type of dumbbells (Sb4, Sb5, Sb11, Sb12, Sb13, Sb14) is placed at the z = 0 and is aligned within the (001) plane in a wind-mill pattern (figure 3.15 c).

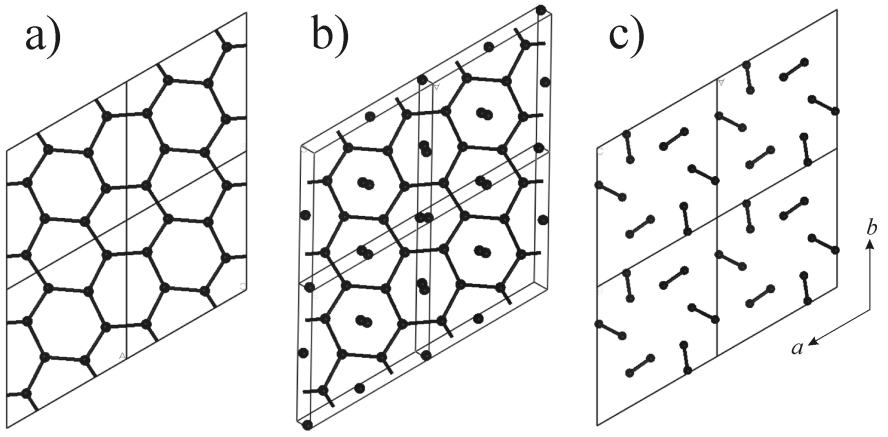

Figure 3.15: Arrangement of different Sb species in $Zn_{1+\delta}Sb$. a) Hexagonal arrangement of Sb^{3-}, b) $(Sb_2)^{4-}$ dumbbells orthogonal to (001) plane c) wind-mill arranged $(Sb_2)^{4-}$ dumbbells in (001) plane.

Several crystalline phases are known within the Zn-Sb phase diagram close to the 1:1 composition: orthorhombic ZnSb (*Pbca*), $Zn_{13}Sb_{10}$ (three polymorphs crystallizing in space groups *R*-3*c*, *C*2/*c* and *C*-1 [48]), and α- and β-Zn_4Sb_3 [51, 52]. The structure of $Zn_{1+\delta}Sb$ is very closely related to the rhombohedral polymorph of $Zn_{13}Sb_{10}$: both display a hexagonally packed channel structure. This similarity is seen the best in [001] projections (figure 3.14 a+b). The lattice parameters a and b are connected by the transformation sketched in the figure 3.14: a_{P-1}=2/3*(a_{R-3c}-b_{R-3c}), b_{P-1}=2/3*(a_{R-3c}+2*b_{R-3c}). Yet, the two structures look very different when viewed from the side (figure 3.14 c+d).

In the rhombohedral polymorph of $Zn_{13}Sb_{10}$ the $(Sb_2)^{4-}$ dumbbells are shifted up and down along [001], while the $(Sb_2)^{4-}$ dumbbells in $Zn_{1+\delta}Sb$ are located on the same height. The orthorhombic ZnSb in turn, has a more complicated arrangement consisting of three independent intercalating sets of $(Sb_2)^{4-}$ dumbbells.
In contrast to the rhombohedral polymorph of $Zn_{13}Sb_{10}$, in which each Sb atom of a dumbbell is coordinated by three Zn atoms, the Sb atoms in Zn_8Sb_7 are coordinated by four Zn atoms (compare figure 3.14 c+d). This coordination of Sb is, in turn, consistent with the coordination observed in ZnSb. The distances between Sb atoms within the dumbbells range from 2.72 Å to 2.91 Å, and are in a good agreement with the corresponding distances for *R*-3*c* $Zn_{13}Sb_{10}$ structure and for orthorhombic ZnSb. The distances between the Sb in the dumbbells and the coordinating Zn also agree well with the known structures: for the new found structure these distances range from 2.66 Å to 3.07 Å, for the orthorhombic ZnSb phase range from 2.64 Å to 3.0 Å, and are 2.68 Å for the rhombohedral polymorph of $Zn_{13}Sb_{10}$.

All structures are related and include common motifs. Under non-equilibrium conditions it is difficult to predict which crystalline phase forms; the output of the reaction is ruled by kinetic effects rather than the Gibbs free energy. In contrast to the solid state synthesis of nano-Zn_4Sb_3 reported by Schlecht [68], this wet chemistry approach produces a "Zn_4Sb_3" related nanophase in very short reaction times. This is due to the high collision rate of individual particles in liquid dispersion. On the other hand, this reaction triggered by nanoparticle collisions leads to a comparably broad particle size distribution and low crystallinity of the particle surfaces.

3.3 Conclusion

In conclusion, a new low-temperature approach to the synthesis of atomically ordered nanocrystals using nanoparticle precursors has been demonstrated. By utilizing reduced nanosize metal precursors solid-solid diffusion is not rate limiting; therefore low reaction temperatures can be used that allow the formation of phases in the subsolidus regime.

Avoiding high-temperature annealing minimizes sintering, and the crystalline nanoparticles can be redispersed in solution for high-volume applications. $Zn_{1+\delta}Sb$ could be obtained only in the presence of a large excess of Zn that was removed subsequently by mild acid treatment. Since diffusion clearly precedes nucleation in the bimetallic precursors, it is possible to synthesize ordered intermetallic nanocrystals near 200°C without a high-temperature annealing step.

The TEM data show the presence of at least two crystalline phases. This raises the fundamental question how powerful and reliable structure determinations based on X-ray powder diffraction for nanomaterials with complex structures and mixtures really are. Further insight was obtained using high-resolution electron diffraction analysis of single nanoparticles. In all samples, two crystalline phases, ZnSb and $Zn_{1+x}Sb$, were observed, phase segregated from the nano-Zn_4Sb_3 precursor that was obtained in the primary reaction from activated Zn and Sb nanoparticles.

X-ray powder diffraction data could be fitted in a first step to the crystallographic phases Zn_4Sb_3 and ZnSb, while they do not allow the distinction between the Zn_4Sb_3 and $Zn_{1+\delta}Sb$ phase due to the quality of the XRD data, the profile broadening and the complexity of the corresponding crystal structures. Anyway, HRTEM showed immediately that most of the sample consisted of a new phase that cannot be fit inside the Zn-Sb system.

A deeper insight was obtained using Electron diffraction tomography of several single crystalline nanoparticles, obtaining cell parameters and space group of known ZnSb and a new $Zn_{1+\delta}Sb$. *Ab initio* structure solutions were performed for both the phases on the basis of electron diffraction data obtained by Automated diffraction tomography (ADT). Whereas for the orthorhombic ZnSb structure a rather limited non-precessed ADT data set was sufficient to obtain a structure solution, Precession electron diffraction data were necessary for the more complex phase $Zn_{1+\delta}Sb$. This new $Zn_{1+\delta}Sb$ phase crystallizes with a hexagonal pseudo-symmetry in the triclinic space group P-1 and show strict relations with both $Zn_{13}Sb_{10}$ and ZnSb. Remarkably, the structure was obtained by single crystal analysis of a 50 nm particle and the solution was achieved *ab initio* in one step with a fully kinematical approach. The correctness of the structure is supported by the reproducibility of the solution and the stability of Fourier and least-squares refinements.

3.4 Experimental section

X-ray powder diffraction

X-ray powder diffraction data were collected with a Bruker-AXS D8-Discover diffractometer in reflection geometry equipped with a HiStar detector using graphite monochromatized CuKα radiation. Samples were glued on top of glass and (111) silicon substrates, respectively, using VP/VA copolymer (vinylpyrrolidone/vinylacetate). Le Bail fits and Rietveld refinements were performed with TOPAS Academic V1.0 [86] applying the fundamental parameter approach.

TEM and ADT

For TEM investigations the sample was suspended in ethanol and sprayed onto carbon coated copper grid using the sonifier described in ref. [74]. The TEM work was carried out with a Tecnai F30 S-TWIN transmission electron microscope equipped with a field emission gun working at 300 kV. High-resolution (HR-) TEM and electron diffraction patterns were acquired with a CCD camera (14-bit GATAN 794MSC). EDX spectra were recorded in STEM mode and quantified in Emispec ESVision software. ADT data acquisition was performed with a FISCHIONE tomography holder, using the ADT acquisition module described in ref. [69]. STEM images and diffraction patterns were collected using mild illumination setting resulting in an electron dose rate of 10 - 15 e/Å^{2}s. STEM images were collected by a FISCHIONE high angular annular dark field detector (HAADF). Nano electron diffraction was performed employing a 10 μm C2 condenser aperture with a 50 nm beam on the sample. ADT data were collected in standard ED as well as PED mode in steps of 1°.

PED was performed using the SpinningStar unit NanoMEGAS [87]. The precession angle was kept at 0.6° and the precession frequency was 100 Hz. The self-developed ADAP package [70] written in Matlab was used for the data processing, including 3D diffraction volume reconstruction, automated cell parameter determination and intensities integration procedures. For the visualization and validation of the 3D data sets the newly developed ADT-3D software package programmed in C++ [88] was used. The *ab initio* structure solution was performed by direct methods implemented in SIR2008, included in the package Il Milione [80]. The structure refinement was performed using SHELXL97 [81].

Chapter 4

Densification of the $Zn_{1+x}Sb$ nanoparticular compound and characterization of the obtained pellets

4.1 Introduction

Thermoelectric modules require solidified materials. When not working with dense bulk materials, one needs to consider the compaction process as a crucial step prior to the thermoelectric characterization. Conventional hot pressing is not applicable to densification of nanocomposites due to the crystal growth following the high temperatures and long heating times. Therefore, a more sensitive technique is used which is called Spark plasma sintering (SPS) and is characterized by application of the electric current through a power supply, leading to a very rapid and efficient heating. While heating rates of up to 1000°C/min can be achieved, this approach allows the nanoparticular powder to be pressed in a very short time preventing particle growth within the sample.

Extensive studies of the influence of sample compaction of bulk Zn_4Sb_3 on their thermoelectric performance and optimization of pressing conditions have been conducted [89, 90]. Although a hitherto unknown Zn-Sb phase had been prepared, many issues concerning Zn_4Sb_3 also seem applicable to this new phase. Chemical stability of the compound plays a major role, since it has been reported that Zn_4Sb_3 partly decomposes into orthorhombic ZnSb and Zn at temperatures higher than 523 K [1]. High mechanical strength is an additional requirement for the good performance of thermoelectric materials which decreases with increasing porosity [90]. Besides, Pedersen *et al.* have shown that density has a large influence on the thermoelectric properties and conclude that sample compaction is a key determinant for thermoelectric performance of Zn_4Sb_3 [89].

Table 4.1: Sintering conditions of the different pellets.

Pellet number	Heating rate	Sintering temperature	Sintering time
3	160°/min	130°C	5 min
4	230°/min	120-130°C	6 min
5	230°/min	140-150°C	4 min
6	180°/min	190-200°C	3 min

4.2 Results and discussion

4.2.1 Densification of the nanoparticular compound

Synthesis and detailed structural characterization of the $Zn_{1+x}Sb$ nanophase are described elsewhere [91]. A combined batch of the $Zn_{1+x}Sb$ nanopowder was divided into four samples of equal weight of about 500 mg. These samples were pressed into pellets by means of Spark plasma sintering using different sintering conditions. In previous experiments, it was found that the $Zn_{1+x}Sb$ phase decomposes mainly into ZnSb when heated to temperatures >200°C, therefore sintering temperatures of under 200°C were applied. Prior to sintering, the $Zn_{1+x}Sb$ nanoparticular compound was heated at 100°C to remove remainders of surface bound solvent. Exact sintering conditions are summarized in table 4.1. Different sintering temperatures between roughly 130°C and 200°C were chosen and different heating rates were applied. The pressing process was finished within a couple of minutes and the sample cooled down quickly to prevent crystal growth. The temperature vs. time plots of the sintering processes of all four pellets can be found in figure 4.1.

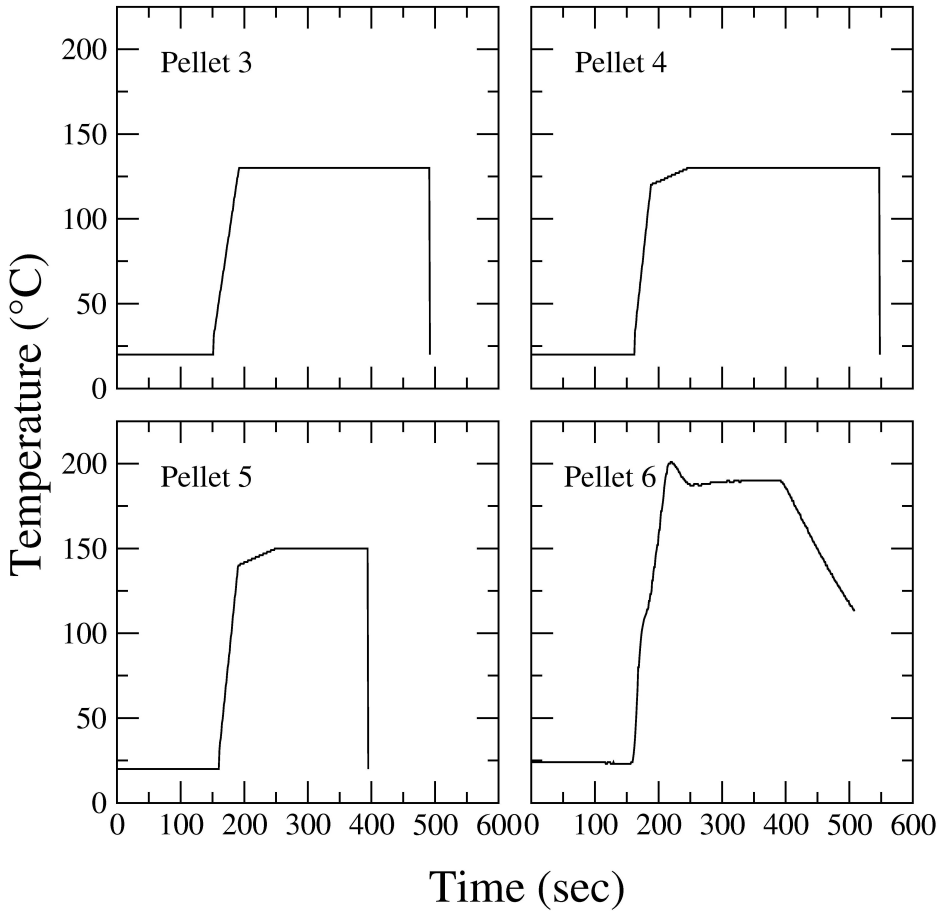

Figure 4.1: Temperature vs. time plots of the sintering processes used to solidify pellets 3-6.

4.2.2 Powder XRD after sintering - Surface composition

Some loose powder was scratched off the surface of the pellets to determine the surface composition of the workpieces. Quantitative phase analysis by Rietveld refinements of the powder X-ray diffraction data are shown in figure 4.2. The starting material (bottom graph in figure 4.2) already shows some decomposition, mainly into the ZnSb phase, due to heating at ca. 100°C. This provides additional insight into the very low phase stability of the $Zn_{1+x}Sb$ compound. With increasing sintering temperature the decomposition of the "Zn_4Sb_3" compound into ZnSb becomes more prominent. Presence of ZnO can be attributed to the oxidation of Zn which is very likely due to handling of pressed pellets at ambient conditions. In addition to ZnSb, Zn and ZnO all samples exhibit variant amounts of graphite due to the use of graphite foil in the pressing form. Of all four pellets, pellets 5 and 6 show the highest grade of decomposition, whereas pellet 6 contains almost none of the original phase (less than 10%). Due to these findings, only pellets 3, 4 and 5 were subject to further investigations.

4.2.3 Synchrotron powder XRD after sintering - Interior composition

Small pieces of the obtained pellets were subject to X-ray diffraction using high-energy Synchrotron radiation penetrating the whole object. Therefore, these data reveal the composition of the interior part of the pellets and not only the surface composition (figure 4.3). According to these data, the content of the original phase also decreases with increasing sintering time (pellet 3 vs. pellet 4) and sintering temperature. Interestingly, when comparing the data of pellets 3 and 4, already very slight changes in sintering conditions result in huge effects on the sample composition.

The data clearly show major differences in surface and interior composition of the pellets after SPS. The content of Zn_4Sb_3 is much lower inside all the pellets than on their surface, in particular in the case of pellet 5 (30% vs. 1%).

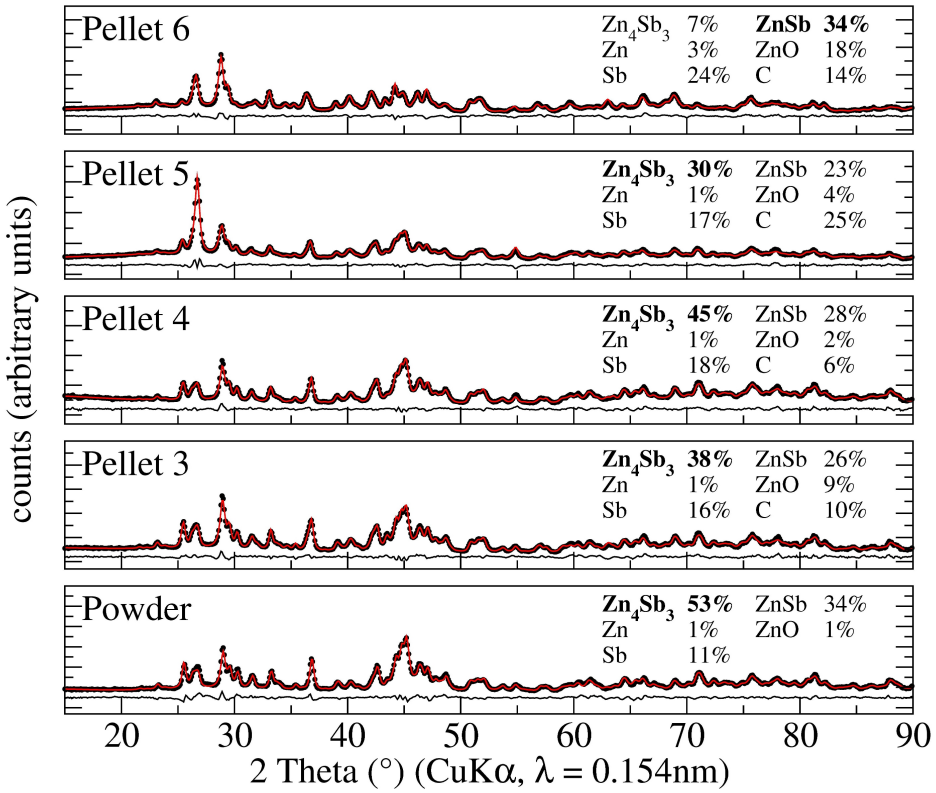

Figure 4.2: Rietveld refinements of the powder XRD data of the original material (referred to as "powder") and powders scratched off the surfaces of pellets 3-6. Major compounds are marked in bold letters.

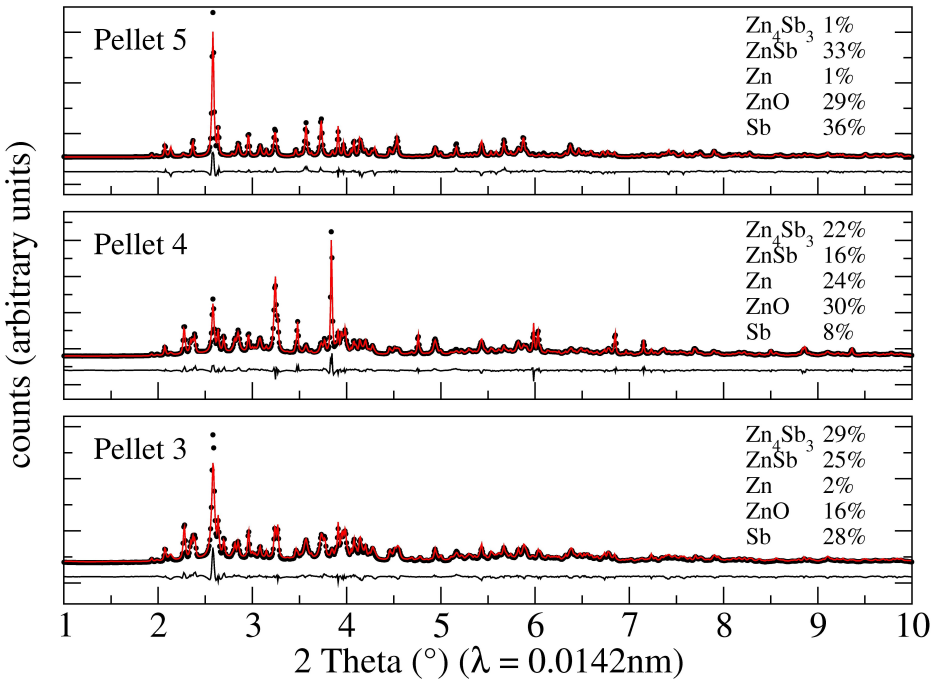

Figure 4.3: Rietveld refinements of high energy Synchrotron data of pellets 3, 4 and 5.

4.2.4 Density and morphology

The morphology after the SPS solidification has been determined by means of Laser microscopy and Scanning electron microscopy images. Density of the pellets has roughly been estimated by mass to volume ratios. The volumes have been obtained through Laser microscopy and have been calculated to be about $3\,\mathrm{g/cm^3}$. This value is independent of the sintering conditions and is about 50% of the theoretical bulk density of Zn_4Sb_3 of $6.37\,\mathrm{g/cm^3}$ [92]. Already through Laser microscopy images the inhomogeneous appearance of the surface of the pellets is apparent (figure 4.4).

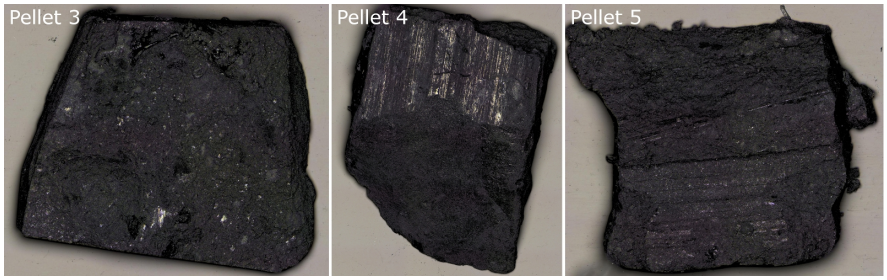

Figure 4.4: Laser microscopy images of pellets 3-5.

SEM images were obtained to provide a more detailed view of the morphology of the pellets. Figure 4.5 shows differently magnified images of the surfaces of the three investigated pellets, all of them not differing much from one another. The surfaces are rough and particularly pellet 3 shows an inhomogeneous composition with some smoother parts (figure 4.5 b). Additionally, many cracks and voids can be found (figure 4.5 a).

However, the nanostructuring of the samples seems to be maintained during the pressing process (inset in figure 4.5 a) which is promising in regard of possibly reduced heat transport. The overall character of the morphology is rather porous (inset in figure 4.5 a and figure 4.5 c) which is responsible for the low density of the pellets.

It should also be noted that all pellets were brittle and broke when cut before contacting for possible thermoelectric measurements. Due to their very low mechanical stability no adequate objects for thermoelectric characterization were obtained.

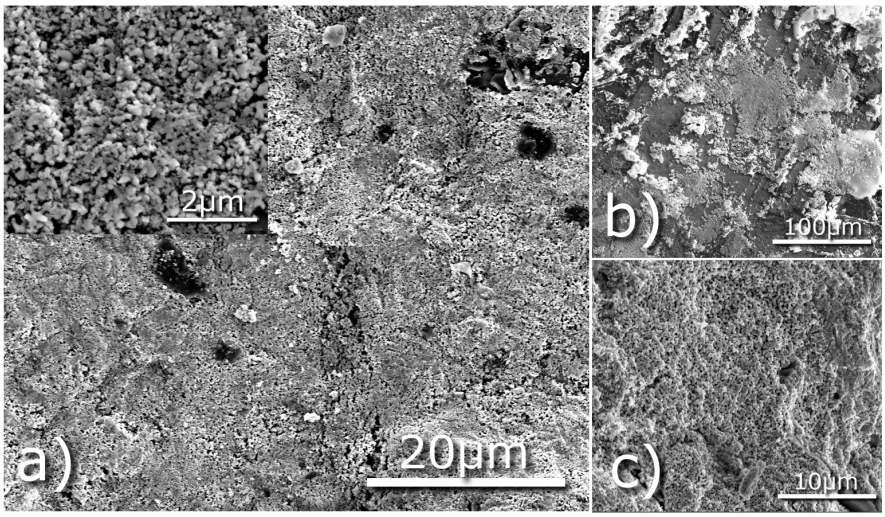

Figure 4.5: SEM images of the three different pellets. a) Pellet 4, inset showing small particles, b) pellet 3, showing different regions on the surface with lighter smoother parts, c) pellet 5 showing nanostructuring and porous structure.

4.2.5 Heat capacity

The heat capacity $C_v = \frac{\partial U}{\partial T}|_v$ or $C_p = \frac{\partial H}{\partial T}|_p$ of a system describes how much energy is required to increase its temperature by an infinitesimal amount. As long as no phase transformations occur and electronic or magnetic contributions can be neglected, the change of internal energy resp. enthalpy results from increased thermal oscillations of atoms in the solid, e.g. from the increase population of phonon states.

Three simple models exist to describe these oscillations [93]: The Dulong-Petit model, which expresses that in the high temperature limit the heat capacity of a solid is close to a constant value ($C = 3Nk_B$, where N is the number of atoms). The Einstein model, representing a collection of individual, non-interacting quantum oscillators, yields acceptable results at intermediate and high temperature. The Debye model which is based on the quantization of macroscopic vibrational modes and relates the heat capacity of crystalline solids to the speed of sound and yields the correct low-temperature T^3 behavior. A more complete approach is to relate the heat capacity to the density of phonon states and the thermal population thereof according to Bose-Einstein statistics, a statistic that describes the number of states of a given energy that are occupied at a given temperature.

The heat capacity measurements done on all three $Zn_{1+x}Sb$ pellets (figure 4.6) shows a deviation from the Debye law, which states that for low temperatures the heat capacity divided by T^3 should be a constant which is directly related to the average speed of sound.[1]

[1] Detailed investigation of this phenomenon is the topic of the thesis of T. Claudio at the Forschungszentrum Jülich.

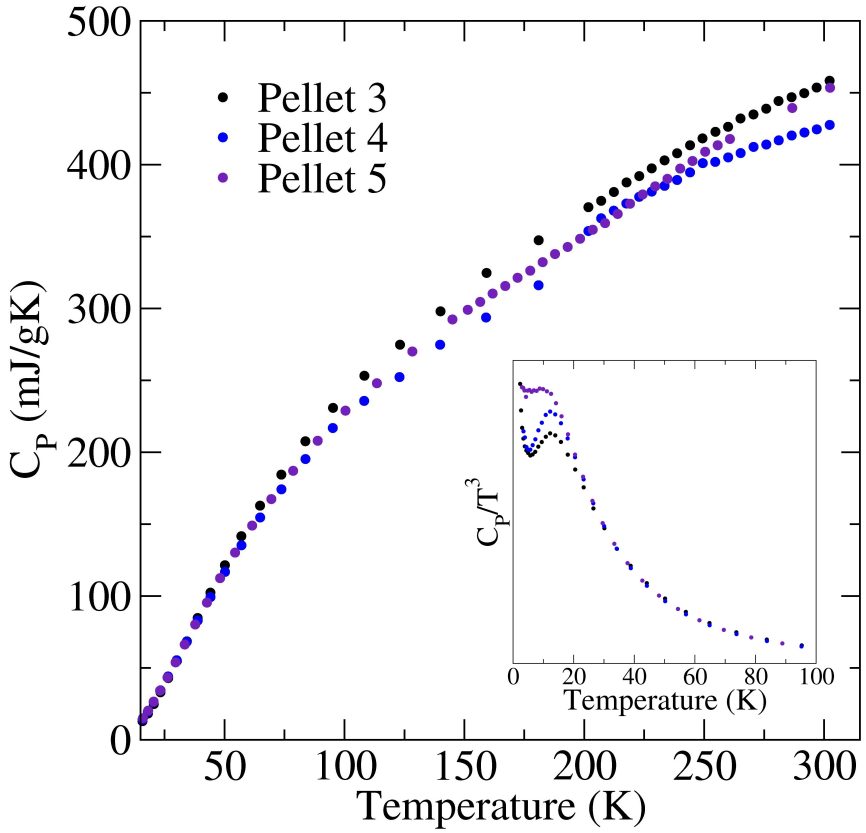

Figure 4.6: Heat capacity of the three pellets of $Zn_{1+x}Sb$ sintered under different conditions as a function of temperature. The inset shows a plot of the heat capacity divided by T^3.

4.2.6 Seebeck scan

Seebeck scan measurements were performed on the surface of pellet 4, which exhibits the smallest grade of decomposition, and pellet 5 showing a higher grade of decomposition. This was conducted by using a Potential Seebeck microprobe, a device for spatially resolved measurement of the Seebeck coefficient (and the electrical conductivity) on a sample´s surface. This Seebeck mapping allows information on the homogeneity or distribution of the components.

Figure 4.7 b) shows an inhomogeneous spatial distribution of the Seebeck coefficient resulting from an inhomogeneous surface composition which is also observed in the optical micrograph in figure 4.7 a). The peak value (from the abundance distribution plot in figure 4.7 c) of 15 μV/K corresponds to distinct grains, while Seebeck coefficients of ca. 80-140 μV/K are typical for the Zn_4Sb_3 phase [94].

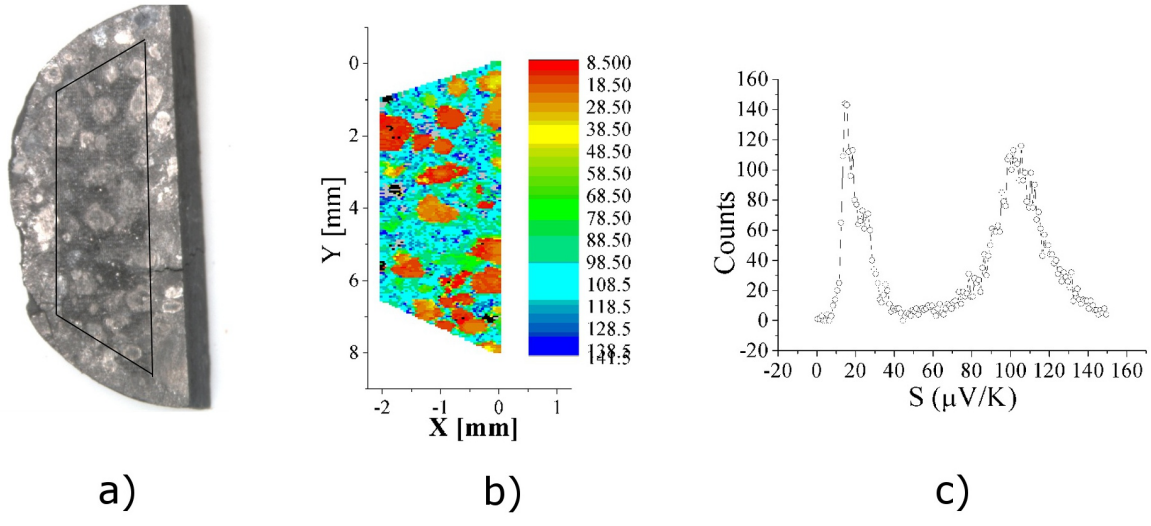

Figure 4.7: Optical micrograph of pellet 4, indicating the scan area (a), Seebeck scan (b) and abundance distribution plot (c) of pellet 4.

Figure 4.8 presents the results from the Seebeck scan measurements performed on the surface of pellet 5.

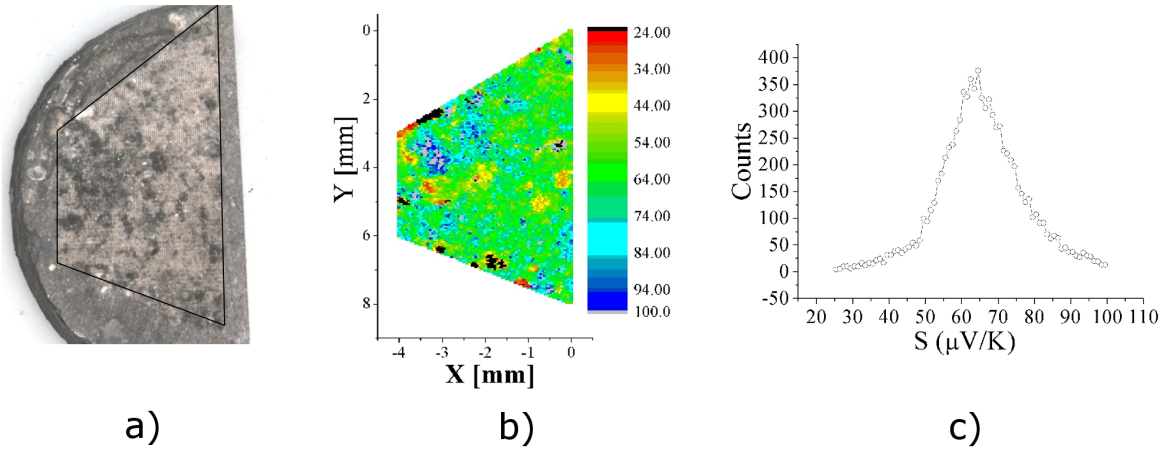

Figure 4.8: Optical micrograph of pellet 5, indicating the scan area (a), Seebeck scan (b) and abundance distribution plot (c) of pellet 5.

A more homogeneous distribution is found in the case of this pellet which had been sintered at a higher temperature. The mean peak value of about 65 μV/K is much lower than the values found for pellet 4.

All these findings are in accordance with results by Stiewe *et al.* [94]. They compared thermoelectric data of both, zone-melted and quenched Zn_4Sb_3 samples and found a varying grade of decomposition as well as varying Seebeck coefficients. According to their findings, lower Seebeck coefficients of around 60 μV/K correspond to mixtures of Zn_4Sb_3 and metals, such as Zn or Sb.

The Seebeck mapping reflects very nicely the results from XRD investigations of the surface of the two pellets. Pellet 4 shows a very inhomogeneous distribution due to distinct grains but also Seebeck coefficients corresponding to the Zn_4Sb_3 phase. Pellet 5, that had been sintered at a higher temperature, exhibits a more homogeneous distribution but a lower Seebeck coefficient which corresponds to mixtures of Zn_4Sb_3 and metals.

4.3 Conclusion

The solidification of a new $Zn_{1+x}Sb$ nanophase by means of Spark plasma sintering was reported. To investigate the influence of the sintering process on the densified samples, different SPS conditions were applied. Powders of the surface of the pellets were subject to "regular" powder X-ray diffraction yielding information about the surface composition. Small pieces of the pellets were also measured using high-energy Synchrotron radiation showing the phases inside the pellets. It was found that small changes in sintering conditions already influence the resulting composition. Additionally, the phase compositions on the surface differ significantly from the ones inside the pellets which show a much higher grade of decomposition.

The density and morphology of the pellets were determined by means of Laser microscopy and Scanning electron microscopy. Estimated densities resemble only 50% of the theoretical bulk value and were not influenced by the sintering conditions. Top view images show the inhomogeneous composition due to the presence of different phases. A more detailed view on the morphology was provided by SEM images which show rather porous structures resulting in the low density of the materials. On the other hand, the nanostructure of the $Zn_{1+x}Sb$ compound was preserved which is crucial for an expected reduced heat transport.

Heat capacity measurements showed decreased thermal conductivity due to nanostructuring. Seebeck mapping of pellet 4 exhibited again the inhomogeneous surface composition and revealed peak Seebeck coefficients typical for Zn_4Sb_3. The Seebeck scan of pellet 5, that had been sintered at a higher temperature, exhibited a more homogeneous distribution but also a lower mean Seebeck coefficient. This can be explained by the higher grade of decomposition in the case of pellet 5.

Due to major decomposition, presence of multiple phases and low densities, no complete set of thermoelectric measurements was collected. The main challenge will be achieving high density materials while maintaining the $Zn_{1+x}Sb$ phase.

4.4 Experimental section

Spark plasma sintering

The Spark plasma sintering was performed using a HP D 5 (FCT Systeme GmbH) system. The samples were heated by a pulsed electric current which flows through the punch-die-sample-assembly using a high current and low voltage. In this study, the pressing tools were made of high-performance graphite. According to the SPS technique, the powder mixture is heated stepwise from room temperature to desired sintering temperature with a heating rate of ca. 100 K/min in a dynamic vacuum. Temperature measurement was done by a thermocouple inside the die, approximately 1 mm away from the sample. After the isothermal dwell time, the electric current was switched off and the pressing tool including the sinterbody cooled down without additional cooling.

X-ray powder diffraction

X-ray powder diffraction data were collected with a Bruker-AXS D8-Discover diffractometer in reflection geometry equipped with a HiStar detector using graphite monochromatized CuKα radiation. Samples were glued on top of glass and (111) silicon substrates, respectively, using VP/VA copolymer (vinylpyrrolidone/vinylacetate). Le Bail fits and Rietveld refinements were performed with TOPAS Academic V4.1 [95] applying the fundamental parameter approach.

Synchrotron X-ray diffraction

Synchrotron X-ray diffraction was performed at the XOR-6 sector (MU-CAT) on the ID-D high energy station of the Advanced Photon Source. The photon wavelength was tuned to 88.4 keV and the scattered radiation collected by a General Electric amorphous silicon 2D-detector with 2048x2048 pixels. Angular rocking of the sample by ±3° was used in order to minimize texture effects. The diffraction patterns were recorded in transmission geometry.

Quantitative phase analysis

Quantitative phase analyses were performed by means of full pattern profile analysis of the corresponding X-ray- and Synchrotron-diffraction data according to the published structural data of "Zn4Sb3" [47], ZnSb [96], Zn [97], ZnO [98], Sb [48] and graphite [99], respectively, using Topas Academic V 4.1 [95].

Laser microscopy

Laser microscopic pictures were recorded using a Keyence VK-8710 Laser microscope equipped with a movable x/y-stage.

Scanning electron microscopy

SEM data were obtained from small pieces of the pellets using a FEI NovaNano FEG-SEM 630. The pieces were attached to an aluminum stub using adhesive conductive carbon tape and were additionally contacted on the surface with an adhesive copper band. An acceleration voltage of 7.5 kV was used and the working distance was set to roughly 6 mm.

Heat capacity measurements

The heat capacity measurements were performed on the sintered pellets between 2 and 300 K in a commercial instrument, the Physical Property Measurement System (PPMS) from Quantum Design. A hybrid adiabatic relaxation method was used to determine the heat capacity with the PPMS software.

Seebeck scan

The measurement of the spatially resolved Seebeck coefficient was performed using a Potential Seebeck microprobe (PSM). Details can be found in reference [100].

Chapter 5

Novel synthesis and characterization of $FeSb_2$ nanostructures

5.1 Introduction

$FeSb_2$ has attracted a lot of attention due to reports on its colossal Seebeck coefficient at low temperatures around 10 K. The synthesis of nanoparticles of this compound may help increase the figure of merit since that approach should decrease its rather high thermal conductivity.

Based on the successful synthesis method for $Zn_{1+x}Sb$ nanoparticles, a similar route was optimized to form the $FeSb_2$ nanostructures. Instead of starting with both kinds of nanoparticles, only antimony nanoparticles were heated in a high-boiling solvent and an iron precursor was added right before its decomposition temperature which then reacted with the antimony to form the final product. Through careful control and choice of the iron precursor, solvent, heating rate, heating temperature and heating time, $FeSb_2$ nanoparticles were obtained.

5.2 Results and discussion

5.2.1 Synthesis

Synthesis of the $FeSb_2$ nanoparticles was achieved through the reaction of "activated" Sb nanoparticles and cyclopentadienyl iron(II) dicarbonyl dimer ($(cpFe(CO)_2)_2$) (99%, Aldrich) in tetraethyleneglycol. "Activated" Sb was produced by reduction of $SbCl_3$ in lithium triethylboronhydride $Li[Et_3BH]$ at room temperature in tetrahydrofuran. The black metal powder obtained was re-dispersed repeatedly in dry tetrahydrofuran to remove residual lithium salts and was subsequently dried *in vacuo*. Sb nanoparticles are highly reactive in ambient air leading primarily to the oxides. ^1H NMR data of Sb nanoparticles kept in inert gas atmosphere show an intense signal according to surface bond stibane ($\delta \approx 1.05$ ppm, c.f. figure 3.1 in chapter 3) which broadens, when the particles were in contact with air. The Sb nanoparticles were dispersed in tetraethyleneglycol and then heated at a rate of 15 K per min under an inert Ar atmosphere. At around 100°C a dispersion of the Fe precursor in tetraethyleneglycol was added and the mixture was heated to 300-310°C at a rate of 10 K per min. Reaction intermediates were taken from the solution at 200°C, 250°C, 300°C and after 60 min at that temperature. The obtained products were collected by centrifugation, washed with ethanol and subsequently dried in a steady Ar flow.

5.2.2 Powder X-ray diffraction

X-ray powder diffraction profiles recorded from the reaction intermediates and the final product (figure 5.1) revealed that the crystalline $FeSb_2$ phase forms in the temperature region between 200°C and 250°C.

At reaction temperatures of 300°C $FeSb_2$ is the only crystalline phase observed. Even after prolonged heat treatment, no decomposition products are detected. According to quantitative phase analysis by Rietveld refinement [101, 102], the samples prepared at 200°C, 250°C and 300°C contain pure Sb, approximately 20% Sb and 80% $FeSb_2$, and virtually pure $FeSb_2$, respectively.

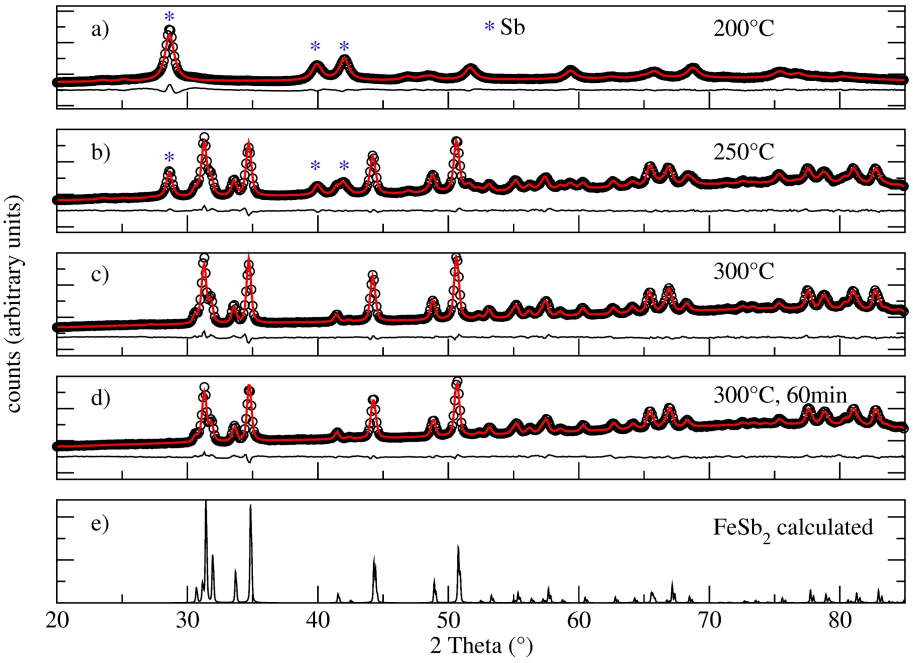

Figure 5.1: Time-dependent (ex situ) X-ray diffraction (experimental data: black circles), Rietveld fits (red line) and corresponding difference plots (black line) at different reaction temperatures and times. Data from samples taken a) at 200°C, b) at 250°C, c) at 300°C, d) at 300°C after 60 min, e) calculated $FeSb_2$ data.

5.2.3 TEM overview and HRTEM

Overview TEM images of the final product (figure 5.2) obtained after heating the reaction mixture at ca. 300°C for 30 min show porous agglomerates of particles with particle sizes of ca. 20-30 nm. Despite intensive sonication during TEM sample preparation, individual crystals were never observed and even the smallest aggregates consisted of several crystals.

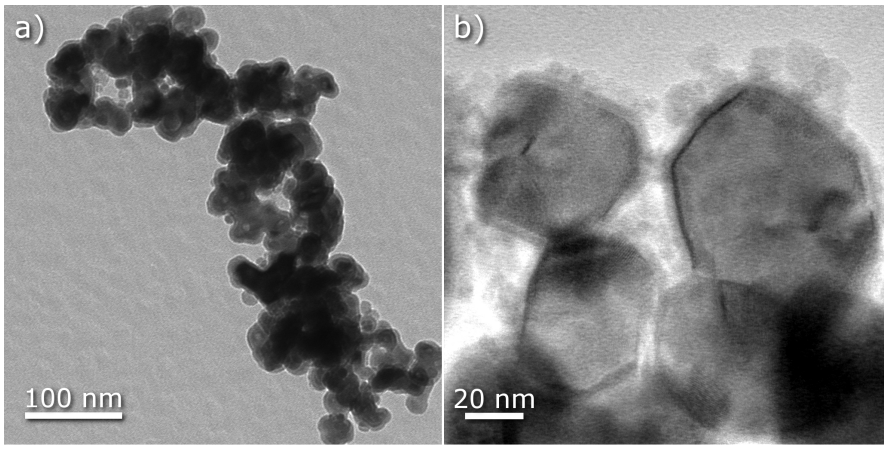

Figure 5.2: a) Overview TEM micrograph of the final $FeSb_2$ product consisting of agglomerates of 20-30 nm sized nanoparticles. b) TEM image showing larger particles ($FeSb_2$) surrounded by smaller particles (Fe_3O_4).

High resolution TEM images reveal the presence of smaller particles covering the outside of the larger particles (figure 5.3). According to d-values determined from FFT of HRTEM micrographs, the larger particles consist of a $FeSb_2$- core and a comparably thin shell of Fe_3O_4. The latter one can be removed by treatment with 1 M HCl which can be shown by SQUID measurements (see figure 5.4).

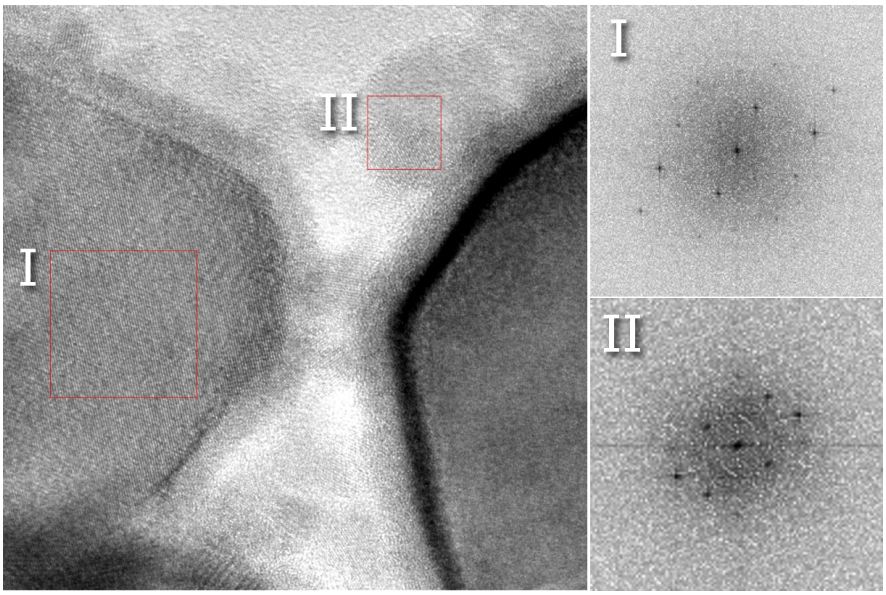

Figure 5.3: HRTEM image and FFTs of the larger $FeSb_2$ particles (I) and smaller Fe_3O_4 particles (II).

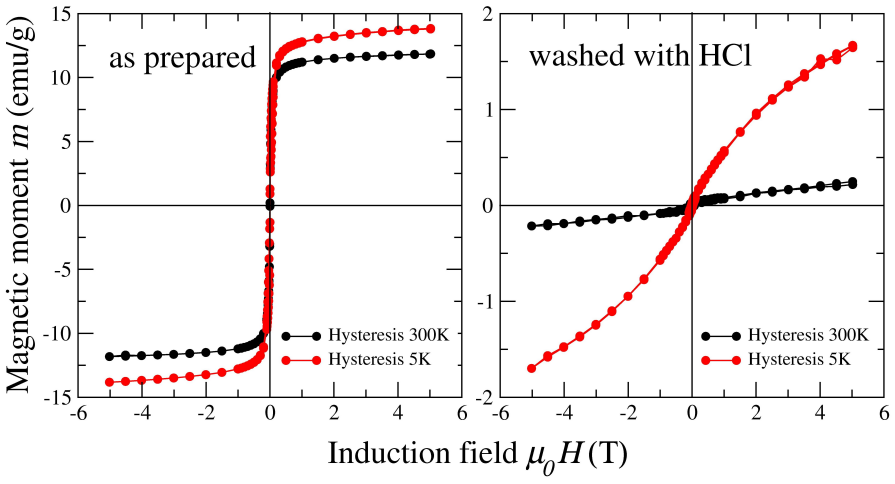

Figure 5.4: SQUID data of as prepared and washed $FeSb_2$ particles.

5.2.4 ^{57}Fe Mößbauer

^{57}Fe Mößbauer measurements were performed at room temperature for intermediate compounds and at temperatures between 90 K and 295 K for the final product. A clear difference between the graphs in figure 5.5 a-d) can be observed. It should be noted that these data were collected from varying small amounts of samples of about 10-50 mg which prevents quantitative statements about the absolute iron content and leads to limited statistics even after long data acquisition.

The red-fit component corresponds to $FeSb_2$ and its content in the samples increases with proceeding synthesis. This finding is in agreement with the formation of the crystalline phases observed in the X-ray diffraction data. Whereas at the beginning of the synthesis (figure 5.1 a) only crystalline antimony can be detected through X-ray diffraction, ^{57}Fe-Mößbauer measurements show a weak signal originating from iron containing species in the reaction mixture.

Cyclopentadienyl iron(II) dicarbonyl dimer was used as the iron source during the reaction. It is known to decompose at 130°C into an intermediate compound with the empirical formula $FeC_2H_2O_6$ which then decomposes at ca. 230°C [103]. In this temperature region iron is released which reacts with the antimony particles and $FeSb_2$ nanoparticles start forming below 250°C, according to the XRD data. The apparent iron content in the samples of the preliminary stages of the reaction (figure 5.5 a+b) is surprisingly low which might be due to the iron being weakly bound, i.e. having a low recoil free fraction, in a molecular complex.

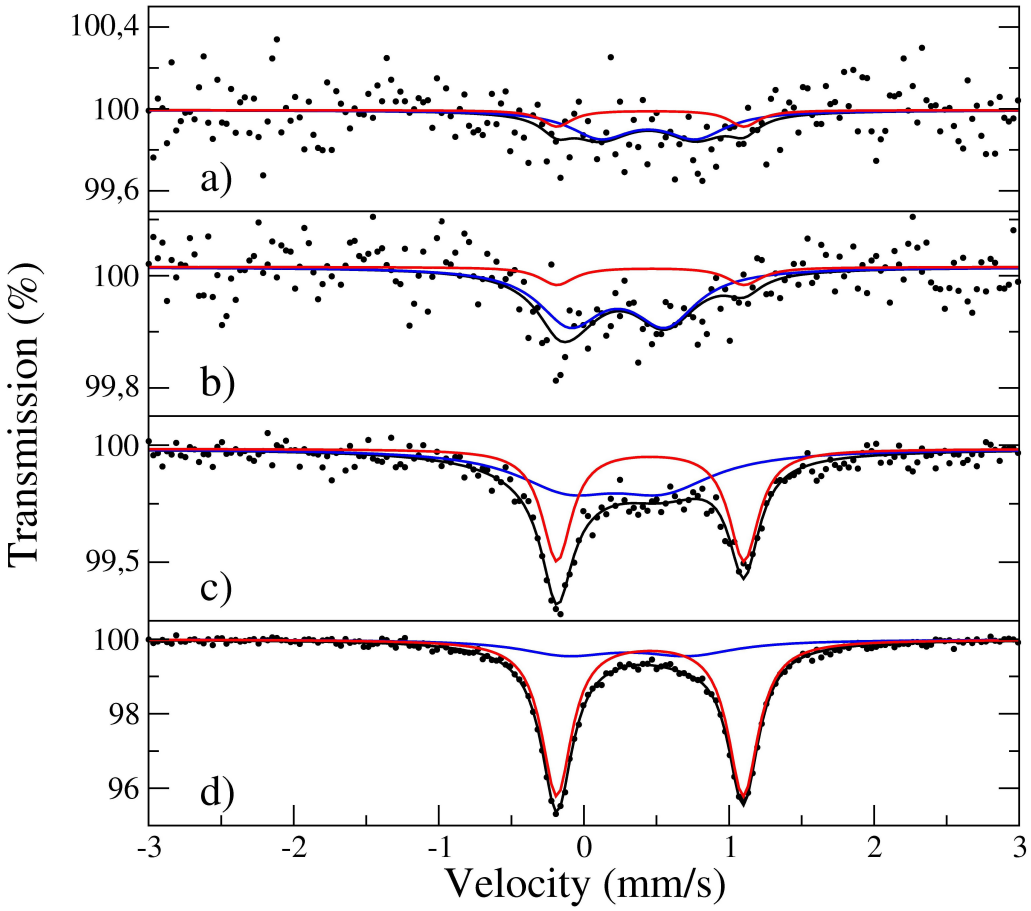

Figure 5.5: Fe-Mößbauer data of intermediate compounds, taken at a) 200°C, b) 250°C, c) 300°C and d) 300°C after 60 min.

Temperature-dependent ^{57}Fe-Mößbauer data are shown in figure 5.6. The data were fitted with two doublets, one corresponding to $FeSb_2$, the other to impurity phases, modeled as a broad doublet component attributed to Fe(III). The final decomposition product of $(cpFe(CO)_2)_2$ is iron oxide which can be observed in the HRTEM images as well as detected by the ^{57}Fe-Mößbauer measurements [104].

The quadrupole splitting (QS) of $FeSb_2$ nanoparticles ranges between 1.3 and 1.5 mm/s and increases with decreasing temperature.

In figure 5.6 b), the dependence of the QS on the temperature is compared with the findings of Steger and Kostiner and the slightly smaller temperature-dependence can be related to a somewhat larger band gap [105]. Thus, the small difference in the temperature-dependence is related to slight variations in the semiconducting properties.

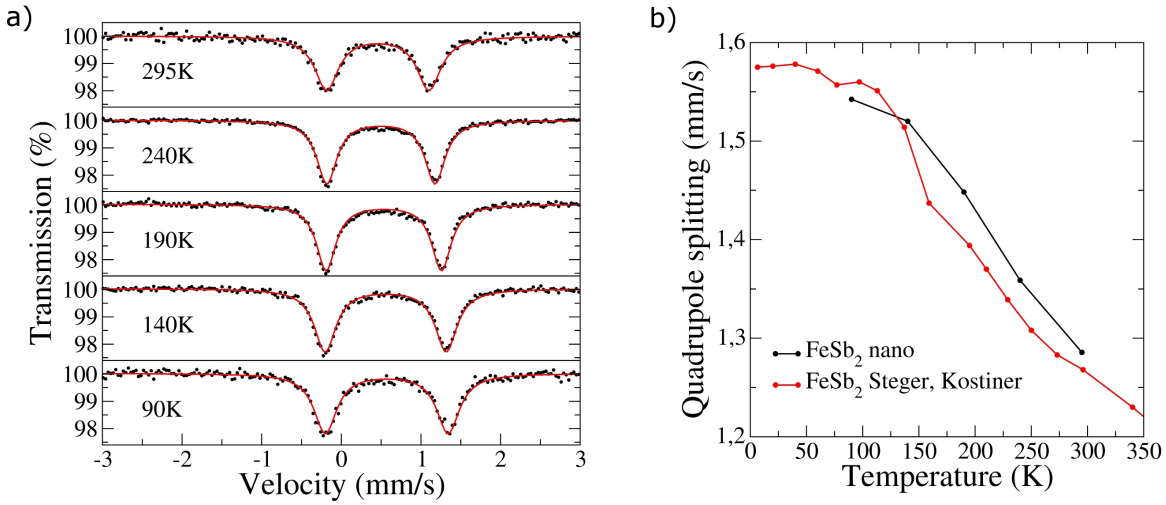

Figure 5.6: a) Temperature-dependent Fe-Mößbauer data and b) quadrupole splitting of $FeSb_2$ nanoparticles.

5.2.5 Nuclear inelastic scattering

The Mößbauer effect, i.e. recoil-free absorption and emission of high-energy X-rays by nuclei of atoms that are bound in a crystal lattice, is also indirectly exploited in Nuclear inelastic scattering to measure the phonon density of states. This method is an element-specific technique for probing lattice vibrations [106, 107].

The Sb element specific density of phonon states in nanostructured $FeSb_2$, obtained from the Nuclear inelastic scattering measurements, reveals first an excellent overall agreement of the phonon modes as compared to the bulk, which confirms the good phase purity (inset in figure 5.7), and second a difference at low energies when compared with the bulk material : the Debye level in the reduced density of states (figure 5.7) is higher for the nanostructured material, which corresponds to a slightly larger heat capacity at low temperatures. A calculation of the velocity of sound in this nanostructured material from this data reveals a decrease for the nanostructured material with respect to the bulk [1].

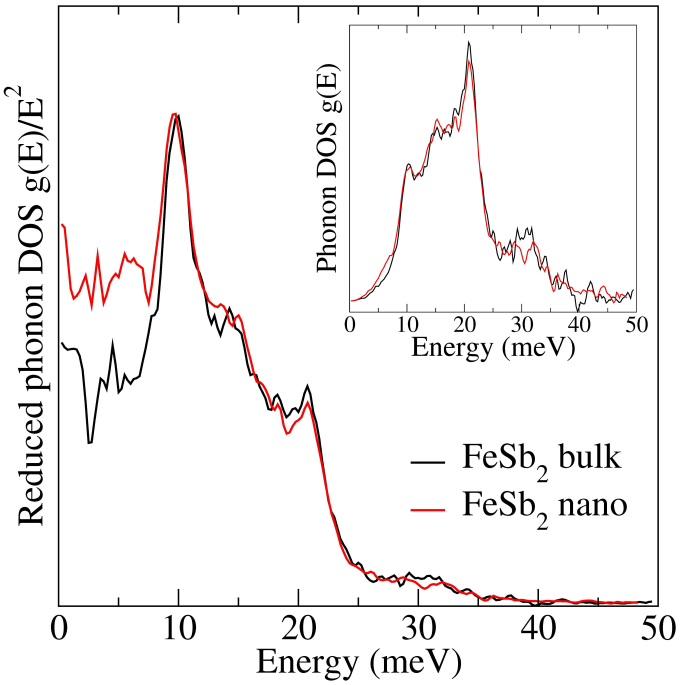

Figure 5.7: Reduced phonon density of states of bulk and nano $FeSb_2$.

[1]The study of the lattice dynamics of the nanostructured materials which is summarized here is the subject of the thesis of Tania Claudio from the Forschungszentrum Jülich and Université de Liége.

5.3 Conclusion

A novel solution-based synthesis of $FeSb_2$ nanoparticles is presented, starting from antimony nanoparticles and a molecular iron precursor. The synthesis process was investigated through a time-dependent X-ray diffraction study showing the formation of the $FeSb_2$ phase between 200 and 250°C. TEM micrographs exhibit small particles of about 20-30 nm in size covered by a small "shell" of iron oxide, corresponding to HRTEM studies. The iron oxide can be removed by HCl treatment which was shown by SQUID measurements of an as prepared and a washed sample.
To provide a more detailed insight into the formation process and the final product, ^{57}Fe-Mößbauer measurements were conducted on intermediate samples as well as the final $FeSb_2$ nanoparticles. As can be expected from the synthesis, ^{57}Fe-Mößbauer data of the intermediate compounds show an increasing $FeSb_2$ content in the samples with increasing reaction temperature and time. Samples taken at 200°C and 250°C show none or only a small amount of $FeSb_2$, respectively. Together with the X-ray diffraction study, this shows the presence of crystalline antimony and likely molecular iron species at temperatures of around 200-250°C which react to form the final $FeSb_2$ nanoparticles.

Phonon density of states of $FeSb_2$ nanoparticles were obtained by measuring Nuclear inelastic scattering on the prepared sample and compared to bulk values. The thermal conductivity in the nanomaterial is decreased which is related to phonon scattering at the nanoparticle boundaries but is also partly due to reduced speed of sound.

5.4 Experimental section

X-ray diffraction

X-ray powder diffraction data were collected with a Bruker-AXS D8-Discover diffractometer in reflection geometry equipped with a HiStar detector using graphite monochromatized CuKα radiation. Samples were glued on top of glass and (111) silicon substrates, respectively, using VP/VA copolymer (vinylpyrrolidone/vinylacetate). Le Bail fits and Rietveld refinements were performed with TOPAS Academic V4.1 [95] applying the fundamental parameter approach.

TEM and HRTEM

For TEM investigations the sample was suspended in ethanol and dropped onto a carbon coated copper grid. The images were obtained using a Philips EM420 instrument with an acceleration voltage of 120 kV.

For HRTEM investigations the sample was also suspended in ethanol and sprayed onto carbon coated copper grid using the sonifier described in ref. [74]. The TEM work was carried out with a Tecnai F30 S-TWIN transmission electron microscope equipped with a field emission gun working at 300 kV. High-resolution (HR-) TEM and electron diffraction patterns were acquired with a CCD camera (14-bit GATAN 794MSC).

^{57}Fe-Mößbauer

Approximately 10-40 mg of the powder sample were mixed with boron nitride in order to obtain a homogeneous absorber. The mixture was filled densely into a titanium frame to prevent movement of the sample during the measurement. The ^{57}Fe-Mößbauer spectra, at temperatures ranging from 90 to 295 K, were measured on a constant-acceleration spectrometer that utilized a rhodium matrix cobalt-57 source. The instrument was calibrated at 295 K with alpha-iron powder. The sample temperature in the Janis SV-300 cryostat was controlled with a Lake-Shore 330 temperature controller and a silicon diode mounted on the copper sample holder. The accuracy of the sample temperature is better than $\pm 1\%$.

Nuclear inelastic scattering

The phonon DOS was measured with Nuclear inelastic scattering (NIS) at the beamline ID22 of the European Synchrotron Radiation Facility (Grenoble, France) with a 16 bunch mode. An energy resolution of 1.2 meV - determined by the scattering of photons in forward direction - was obtained. A detailed description of the measurement and the experimental arrangement is reported in [108]

Chapter 6

Densification of $FeSb_2$ nanostructures by Spark plasma sintering and thermoelectric characterization

6.1 Introduction

In order to determine any thermoelectric data of the obtained $FeSb_2$ nanoparticles, densified and mechanically robust materials had to be obtained which was also done by means of Spark plasma sintering. The nanoparticles were heated in tetraethyleneglycol up to 300°C and no decomposition could be noted. Based on these heating experiments, the $FeSb_2$ nanoparticles should be able to tolerate the SPS treatment at higher temperatures than were used for solidification on the "$Zn_{1+x}Sb$" pellets.

Table 6.1: Sintering conditions of the different $FeSb_2$ pellets.

pellet	Sintering temperature	Sintering time
1	200°C	3 min
2	250°C	3 min

6.2 Results and discussion

6.2.1 Densification of the $FeSb_2$ nanoparticles

A combined batch of $FeSb_2$ nanoparticles was divided into two equal amounts of about 500 mg which were pressed using two different sintering conditions (see table 6.1).

Time vs. temperature plots of the two different sintering processes are compared in figure 6.1.

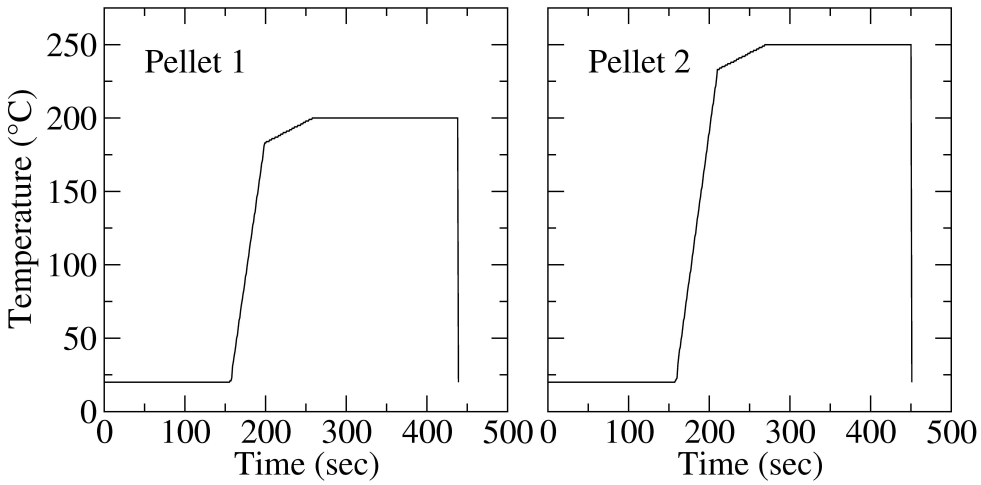

Figure 6.1: Temperature vs. time plots of the sintering processes used to solidify the $FeSb_2$ pellets (1 and 2).

6.2.2 Powder X-ray diffraction data - Surface composition

Some loose powder was scratched off the surface of the two pellets which was subject to powder X-ray diffraction measurements (figure 6.2). All data were refined using the $FeSb_2$ structural model and no crystalline impurity was detected in the as prepared $FeSb_2$ compound (referred to as "powder" in figure 6.2). For the refinement of the XRD data of pellets 1 and 2, graphite was added as an additional crystalline phase which is responsible for the reflection at around 26° (2θ). Pellet 1 contains about 12% and pellet 2 about 2% of Graphite remaining from the pressing tool used during Spark plasma sintering. No decomposition (at least on the surface of the pellets) of the $FeSb_2$ phase during the sintering could be detected by means of XRD investigations.

6.2.3 ^{57}Fe Mößbauer

^{57}Fe-Mößbauer data obtained from powderized samples extracted from the two different pellets are presented in figure 6.3. The red-fit component corresponds to $FeSb_2$ whereas the blue component is associated with impurity phases. Despite the promising X-ray diffraction data of both pellets, the ^{57}Fe-Mößbauer data reveal signs of decomposition.

In pellet 1 and pellet 2 about 30% and 50% of impurity phases are observed, respectively, which indicates a higher grade of decomposition in the case of the pellet sintered at higher temperatures (250°C instead of 200°C).

The impurity phases have hyperfine parameters indicating iron(III) phases, a part of which is likely superparamagnetic alpha-Fe_3O_4, because the 90 K spectrum, not shown, reveals the onset of magnetic hyperfine splitting.

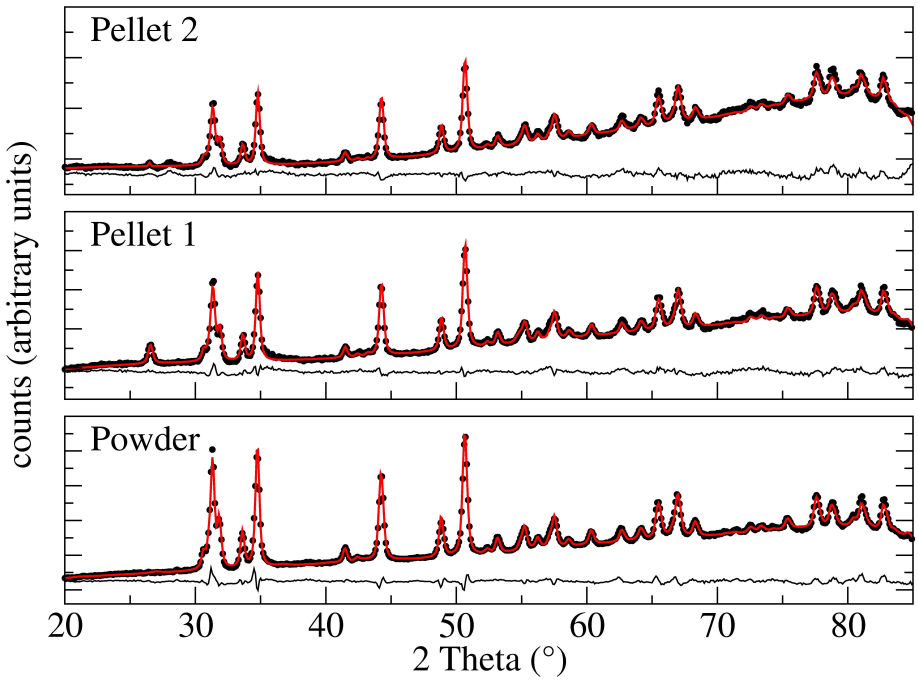

Figure 6.2: Rietveld refinements of the powder XRD data of the original material (referred to as "powder") and powders scratched off the surfaces of the $FeSb_2$ pellets (1 and 2).

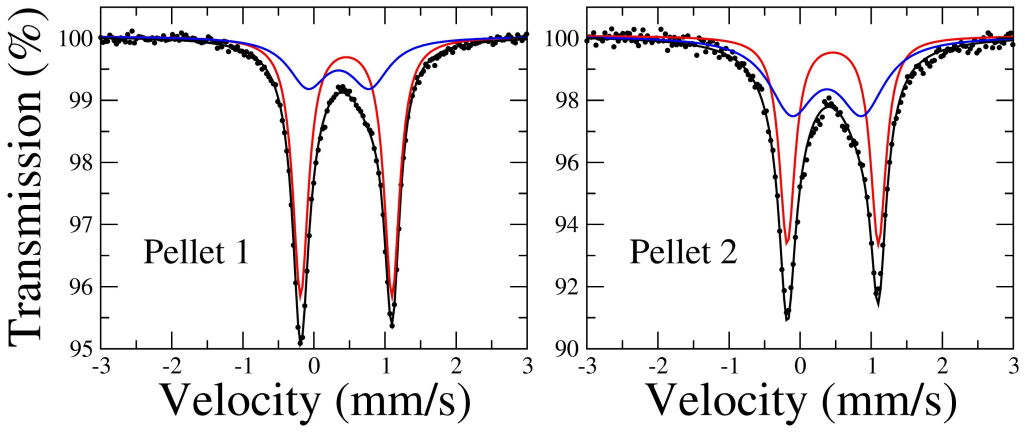

Figure 6.3: ^{57}Fe-Mößbauer data of the $FeSb_2$ pellets (1 and 2).

6.2.4 Density and morphology

Laser microscopy images allow insight into the morphology of the two pellets (figure 6.4) showing rough surfaces with a shiny metallic appearance. Densities of these pieces could also be estimated through weight by volume which was determined by Laser microscopy. The calculated values are about 4 g/cm^3 and 4.4 g/cm^3, which correspond to about 53% and 57% of the theoretical bulk density of $FeSb_2$ of 7.7 g/cm^3 [109], respectively.

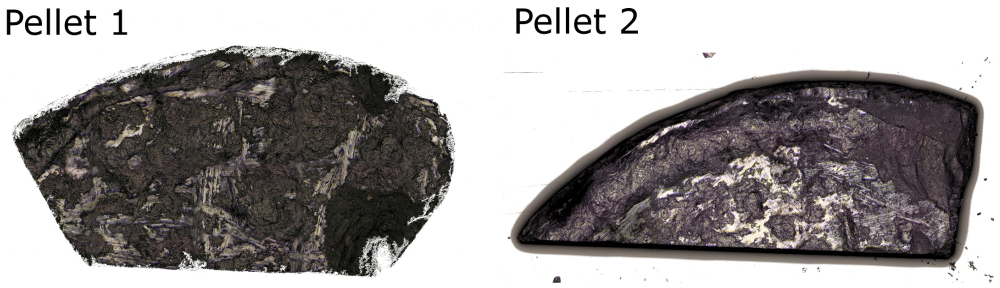

Figure 6.4: Laser microscopy images of pellets 1 and 2.

A more detailed view on the surface morphology of the pellets was obtained by Scanning electron microscopy. Images recorded with different magnifications are shown in figures 6.5 and 6.6. The micrographs show smoother parts of almost "closed" surfaces on the one side and also cracks and holes on the other. In higher magnification the structures exhibit small particles thus the size of the initial particles seems to be maintained during the sintering process. While pellet 1 shows an overall porous character, the surface of pellet 2 gives the impression of a denser material.

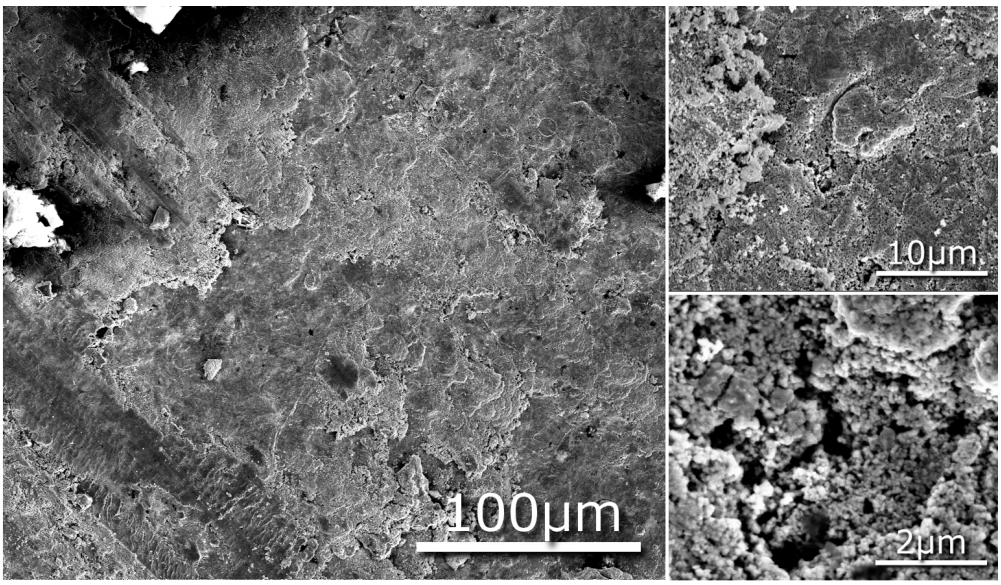

Figure 6.5: SEM images recorded with different magnifications of pellet 1.

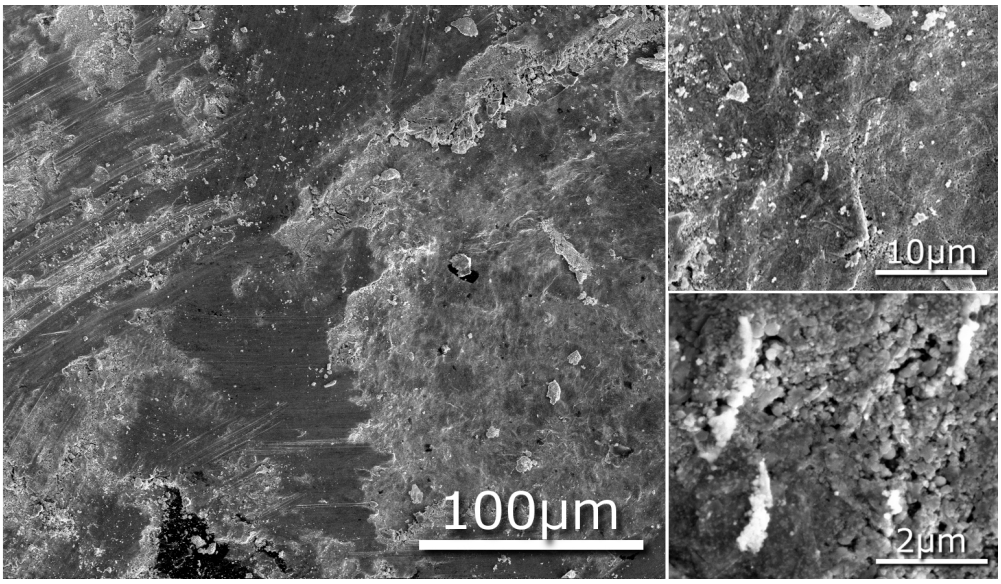

Figure 6.6: SEM images recorded with different magnifications of pellet 2.

6.2.5 Heat capacity

To study the lattice dynamics, heat capacity measurements on both pellets were performed.

Similar to the findings for the "$Zn_{1+x}Sb$" pellets, the heat capacity measurements done on both $FeSb_2$ pellets (figure 6.7) reveal a deviation from the Debye law, which states that for low temperatures the heat capacity divided by T^3 should be a constant. This deviation is indicative either of electronic contributions or, more likely, of specificities of the sound propagation due to the nanostructures.[1]

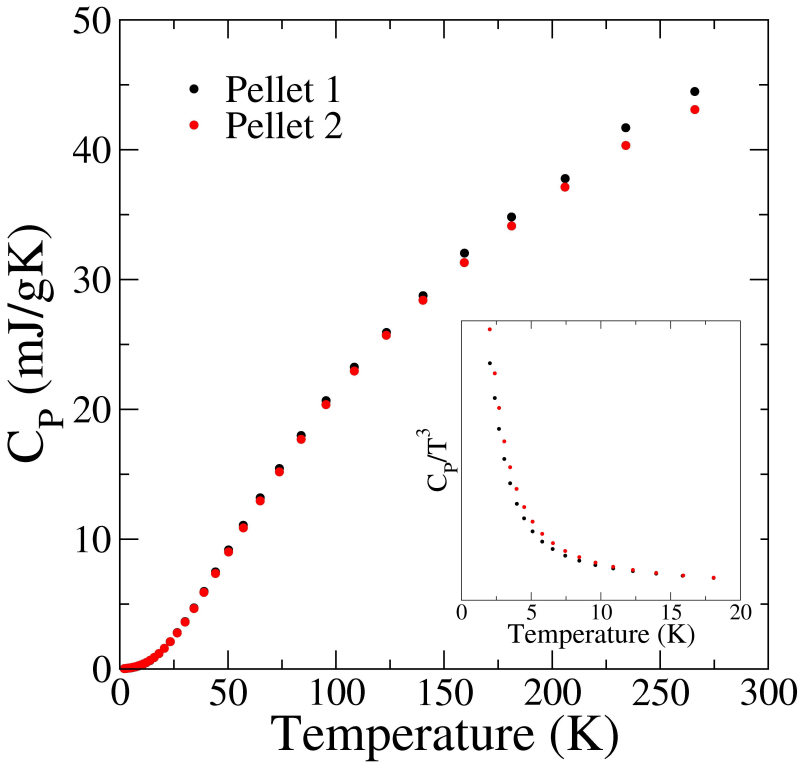

Figure 6.7: Heat capacity of two pellets of $FeSb_2$ sintered under different conditions as a function of temperature. The inset shows a plot of the heat capacity divided by T^3.

[1]Detailed investigation of this phenomenon is the topic of the thesis of Tania Claudio at the Forschungszentrum Jülich.

6.2.6 Thermoelectric characterization

After the powder had been pressed into a pellet of cylindrical shape, it was cut into a bar and contacted prior to the measurements of the transport properties (Seebeck coefficient, electrical conductivity and thermal conductivity). A schematic of the different steps during that process and images of the corresponding materials are shown in figure 6.8.

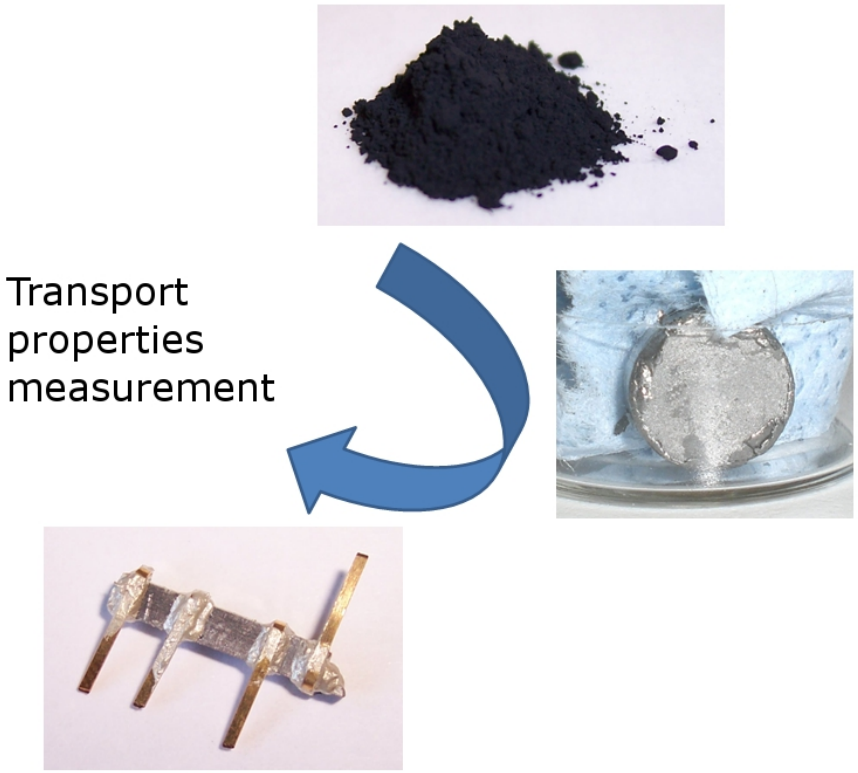

Figure 6.8: Images of the materials during each step of the process, from loose powder to a contacted bar.

Pellet 1 was cut into a bar with the approximate dimensions 2 x 2 x 10 mm. The sample was polished carefully before contacting in order to remove oxide layers that may have formed during synthesis and the measurement.

The bar was contacted with four copper stripes using silver epoxy paste, that were wrapped around the bar to homogenize the current passing through.

For the electronic contribution to ZT, Seebeck coefficient and electrical resistivity were measured and are shown in figure 6.9.

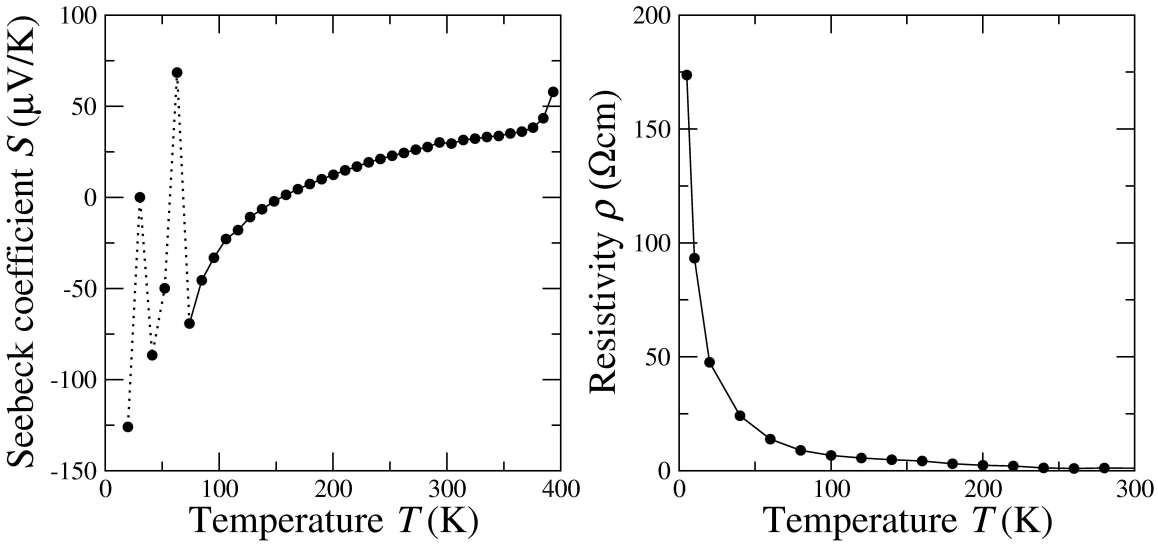

Figure 6.9: Temperature-dependent Seebeck coefficient and electrical resistivity of $FeSb_2$ (pellet 1).

The room temperature Seebeck coefficient reaches values of up to 50 μV/K and changes its sign from positive to negative values at approx. 150 K. The resistivity of the solidified $FeSb_2$ sample shows a semiconducting behavior with a rapid increase at low temperatures.

The Seebeck coefficient could not be measured at temperatures below 80 K and the values in this temperature region, which are presented in figure 6.9, have to be neglected. This is the consequence of the high resistivity at low temperatures in combination with the measurement technique (PPMS).

Unfortunately, this does not allow the determination of the Seebeck coefficient in the most interesting temperature region. As has been reported by Bentien *et al.* [64], a colossal Seebeck coefficient of -45.000 μV/K is found at temperatures around 10 K. This spectacularly high number produces a very high power factor $S^2\sigma$ (S^2/ρ). What lowers the thermoelectric figure of merit of bulk $FeSb_2$, is the high thermal conductivity in the low temperature region which reaches values of up to 500 W/mK at 10 K.

The temperature-dependent thermal conductivity of the solidified $FeSb_2$ sample (pellet 1) is presented in figure 6.10.

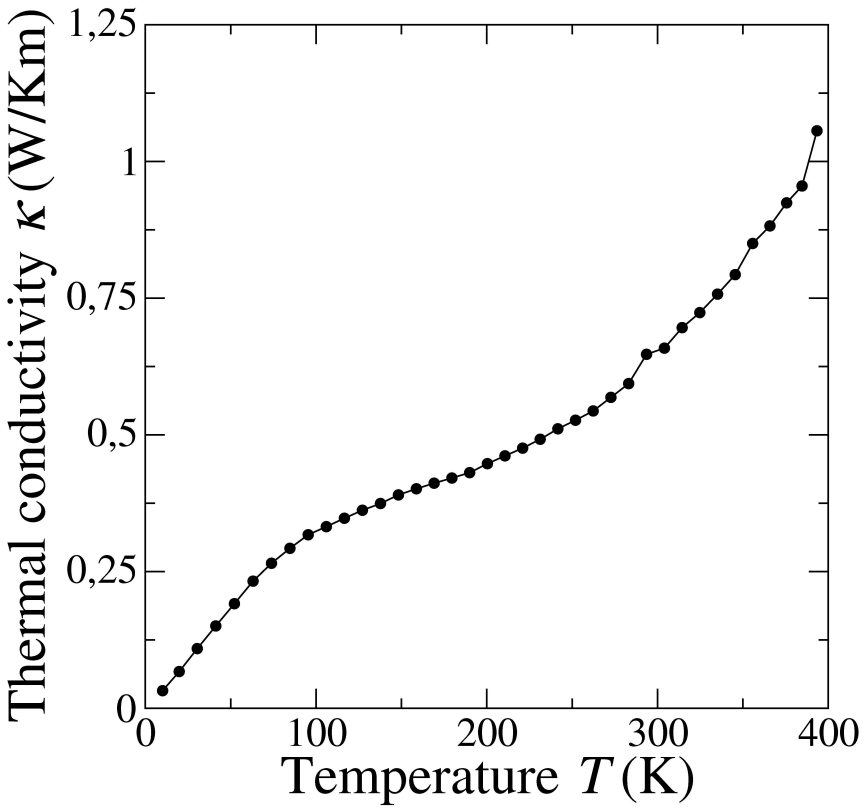

Figure 6.10: Temperature-dependent thermal conductivity of solidified $FeSb_2$ (pellet 1).

The sample shows a drastic reduction in thermal transport which is expected due to its nanostructuring. In the most important temperature region (10 K), values of as low as 0.3 W/mK can be found which decreases the thermal conductivity by three orders of magnitude compared to the reported bulk values [66].

In the temperature region between 300 K and approx. 70 K, the calculated ZT values lie in the order of 10^{-5} to 10^{-6}. The very low thermal conductivity is promising but cannot balance out the decreased power factor consisting of Seebeck coefficient and resistivity.

It was not possible to obtain all thermoelectric data for pellet 2, since it broke after attachment of the copper contacts. However, the resistivity could be determined from small pieces remaining after the bar had broken. The resistivities of both pellets are compared in figure 6.11.
Both data sets resemble a semiconducting behavior with decreasing resistivity at higher temperatures. In the case of pellet 2, the resistivity increases at low temperatures, but not as rapidly as was found in pellet 1. The lower resistivity could be due to the higher density of the pellet (4.4 g/cm^3 vs. 4 g/cm^3) possibly resulting from a higher sintering temperature.

This finding would give rise to a higher power factor and a higher figure of merit compared to pellet 1, assuming similar values of Seebeck coefficient and thermal conductivity.

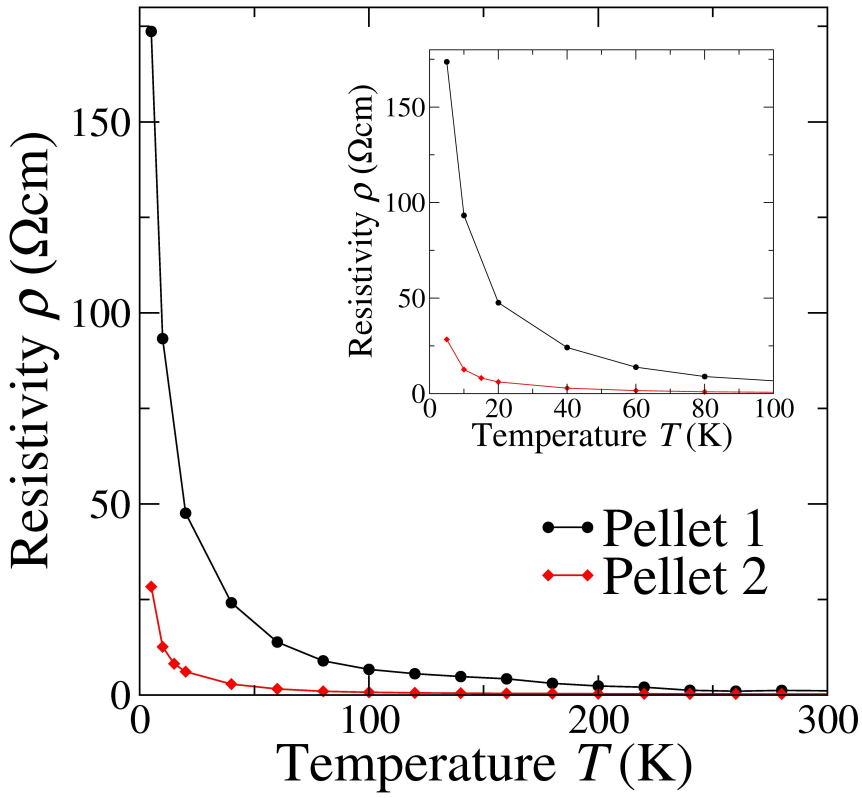

Figure 6.11: Temperature-dependent resistivity of both $FeSb_2$ pellets, inset showing the low-temperature region.

6.3 Conclusion

The solidification and characterization of nanoparticular $FeSb_2$ was reported. Two different sintering temperatures of 200°C and 250°C were applied and the properties of both pellets were compared accordingly.

Surface composition after sintering was determined by powder X-ray diffraction data obtained on loose powder scratched off the surface of the pellets. No decomposition could be detected; however, the interior composition needs to be studied by Synchrotron XRD measurements, as had been done in the case of the "$Zn_{1+x}Sb$" pellets.

^{57}Fe-Mößbauer data were obtained on both pellets providing a more detailed insight into their composition after sintering. Both data sets could be fitted with doublets, one corresponding to $FeSb_2$, the other to impurity phases, modeled as a broad doublet component attributed to Fe(III). Pellet 1 which was sintered at 200°C shows about 30% decomposition, while pellet 2, sintered at 250°C, only consists to about 50% of the original phase.

Laser microscopy allowed the estimation of the density which turned out to be about 60% of the theoretical density of $FeSb_2$. This low value was also supported by the morphology determined through SEM images. The nanoparticular structure was maintained during the sintering which is encouraging in regard to reduced thermal conductivity. On the other hand, the solidified materials exhibit some cracks and voids and provide a rather porous structure.

Heat capacity measurements performed on both pellets show decreased speed of sound and therefore reduced thermal transport.

However, only one of the two pellets could be characterized completely in terms of its thermoelectric properties.

Processing the obtained pellets turned out to be a major challenge in this work. While following the different steps of solidification, cutting the pellet, contacting the bar shaped sample and finally measuring the properties, the largest requirement is the mechanical strength of the pellets. When not robust enough, the samples break during handling, which happened for pellet 2 in this study.

Thermoelectric data were obtained on pellet 1, the sample that showed a smaller degree of decomposition. The room-temperature Seebeck coefficient is comparable with that of bulk $FeSb_2$. It changes its sign at around 150 K reaching increasing negative values until about 80 K. Simultaneously, the electrical resistivity increases rapidly which does not allow the measurement of the Seebeck coefficient in the low temperature region.

On the other hand, the thermal conductivity of the solidified $FeSb_2$ nanoparticles (pellet 1) is reduced by three orders of magnitude at 10 K. The resulting ZT values are very low ranging between 10^{-5} and 10^{-6}. The major drawback of the material is its high resistivity at low temperatures. As a result, no Seebeck coefficient in that temperature region could be obtained. Based on low Seebeck coefficients and low electrical conductivities, the thermoelectric figure of merit is rather low despite a drastical decrease of the thermal transport.

Pellet 2 shows an overall lower resistivity than pellet 1. Unfortunately, no complete thermoelectric characterization was possible. Therefore, it can only be assumed that pellet 2 would provide larger ZT values, if similar numbers for the Seebeck coefficient and the thermal conductivity were reached.

6.4 Experimental section

Spark plasma sintering

The Spark plasma sintering was performed using a HP D 5 (FCT Systeme GmbH) system. The samples were heated by a pulsed electric current which flows through the punch-die-sample-assembly using a high current and low voltage. In this study, the pressing tools were made of high-performance graphite. According to the SPS technique, the powder mixture is heated stepwise from room temperature to desired sintering temperature with a heating rate of ca. 100 K/min in a dynamic vacuum. Temperature measurement was done by a thermocouple inside the die, approximately 1 mm away from the sample. After the isothermal dwell time, the electric current was switched off and the pressing tool including the sinterbody cool down without additional cooling.

X-ray powder diffraction

X-ray powder diffraction data were collected with a Bruker-AXS D8-Discover diffractometer in reflection geometry equipped with a HiStar detector using graphite monochromatized CuKα radiation. Samples were glued on top of glass and (111) silicon substrates, respectively, using VP/VA copolymer (vinylpyrrolidone/vinylacetate). Le Bail fits and Rietveld refinements were performed with TOPAS Academic V4.1 [95] applying the fundamental parameter approach.

^{57}Fe-Mößbauer

Approximately 10-40 mg of the powder sample were mixed with boron nitride in order to obtain a homogeneous absorber. The mixture was filled densely into a titanium frame to prevent movement of the sample during the measurement. The ^{57}Fe-Mößbauer spectra, at temperatures ranging from 90 to 295 K, were measured on a constant-acceleration spectrometer that utilized a rhodium matrix cobalt-57 source. The instrument was calibrated at 295 K with alpha-iron powder.The sample temperature in the Janis SV-300 cryostat was controlled with a Lake-Shore 330 temperature controller and a silicon diode mounted on the copper sample holder. The accuracy of the sample temperature is better than ±1%.

Laser microscopy

Laser microscopic images were recorded using a Keyence VK-8710 laser microscope equipped with a movable x/y-stage.

Scanning electron microscopy

SEM data were obtained from small pieces of the pellets using a FEI NovaNano FEG-SEM 630. The pieces were attached to an aluminum stub using adhesive conductive carbon tape and were additionally contacted on the surface with an adhesive copper band. An acceleration voltage of 7.5 kV was used and the working distance was set to roughly 6 mm.

Heat capacity measurements

The heat capacity measurements were performed on the sintered pellets between 2 and 300 K in a commercial instrument, the Physical Property Measurement System (PPMS) from Quantum Design. A hybrid adiabatic relaxation method was used to determine the heat capacity with the PPMS software.

Thermoelectric measurements

Measurements of the Seebeck coefficient, the resistivity and the thermal conductivity were performed with a Physical Property Measurement System (Model 6000, Quantum System, with the options P400, P600 and P640) from 2 to 400 K. The samples were cut into bars with the approximate dimensions 2 x 2 x 10 mm. The samples were polished before contacting in order to remove oxide layers that may have formed during synthesis and the measurement. The bars have been contacted with four copper stripes that were wrapped around the bars to homogenize the current passing through. The sample chamber was flooded with helium and evacuated afterwards. The measurements were carried out at a pressure of 1.2 x 10^{-4} mbar by a standard four point ac method. An additional correction term for the heat loss at the heating shoes was introduced and applied to the thermal conductivity data as suggested by Müller *et al.* [8] and Quantum Design [110].

Chapter 7

Synthesis and characterization of $Fe_{1+x}Sb$ and ZnSb nanoparticles

7.1 Introduction

Following the previously reported synthetic methods, ZnSb nanoparticles were fabricated in a very similar manner to the $Zn_{1+x}Sb$ sample. Antimony and zinc nanoparticles were synthesized in the first step and heated in the same high-boiling solvent, trioctylamine. Through the adjustment of the detailed conditions - stoichiometry, temperature and heating time - the desired ZnSb phase was obtained.

In a very similar approach to the $FeSb_2$ synthesis, nanoparticles of the $Fe_{1+x}Sb$ phase were fabricated. Higher Fe content in the starting reaction mixture is needed and a different high boiling solvent turned out to be the reaction medium of choice.

Due to the higher amount of iron in the compound, powder X-ray diffraction data have to be considered with caution and care since fluorescence of iron in the X-ray beam (CuKα radiation) decreases the quality of the obtained data. Therefore, XRD measurements with MoKα radiation and also ^{57}Fe-Mößbauer investigations, were carried out to elucidate the structure and possible impurities of the product.

Further characterization is the content of ongoing research.

7.2 $Fe_{1+x}Sb$ - Results and discussion

7.2.1 Synthesis

Tetrahydrofuran was dried with $CaCl_2$ and Na/K and freshly distilled before use. Lithium triethylboronhydride Li[Et_3BH] (Aldrich, 1 M in THF, referred to as "superhydride"), and $SbCl_3$ (99%, ABCR) were used as obtained, $SbCl_3$ was stored in a glove box. Tetraethyleneglycol (Aldrich) was degassed and stored under Ar before use. Sb particles were produced by reducing $SbCl_3$ with 3 equivalents of the 1 M "superhydride" solution at room temperature. The black particles were repeatedly re-dispersed in THF and decanted from the solution, dried *in vacuo* and kept in a glove box.

In a typical synthesis, nanoparticles of the nominal composition $Fe_{1+x}Sb$ were prepared by heating of Sb-nanoparticles (1 mmol) in tetraethyleneglycol with a heating rate of about 15 K/min. A dispersion of cyclopentadienyl iron(II) dicarbonyl dimer (99%, Aldrich) (1 mmol) in approximately 3 ml tetraethyleneglycol was added to the reaction when the Sb solution reached a temperature of around 100°C. The reaction mixture was then heated to ca. 330°C at a rate of 10 K/min and held at that temperature for 90 min. For intermediate products, 2 ml of the solution were extracted by syringe at approximately 200°C, 250°C, 330°C and after 90 min. After cooling to room temperature, the resulting black product was collected by centrifugation (9000 rpm), washed with ethanol and dried under a steady Ar flow.

7.2.2 Powder X-ray diffraction

X-ray powder diffraction profiles recorded from the reaction intermediates and the final product (figure 7.1) revealed that the crystalline $Fe_{1+x}Sb$ phase forms in the temperature region between 200°C and 250°C (figure 7.1 b).

The reaction mixture was held at about 330°C for 60 min to ensure higher crystallinity of the obtained product (figure 7.1 c).

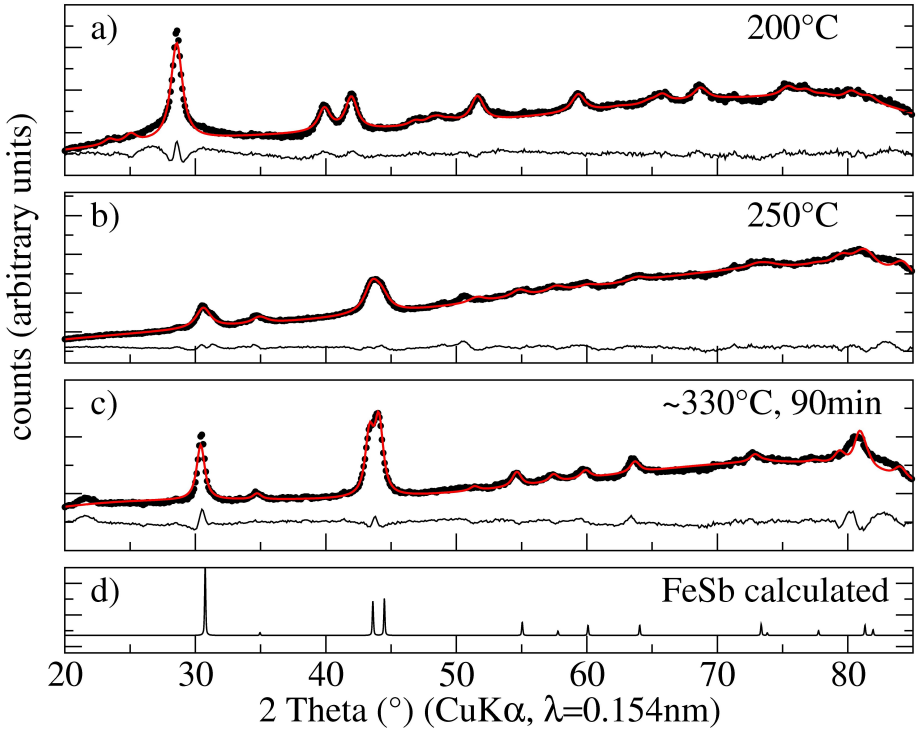

Figure 7.1: Time-dependent (ex situ) X-ray diffraction (experimental data: black dots), le Bail fits (red line) and corresponding difference plots (black line) at different reaction temperatures and times.

The fluorescence of the iron in the CuKα X-ray beam causes some high background (noise), thus decreasing the quality of the X-ray diffraction data.

To overcome this issue, XRD data using MoKα radiation were obtained of the final product (figure 7.2).

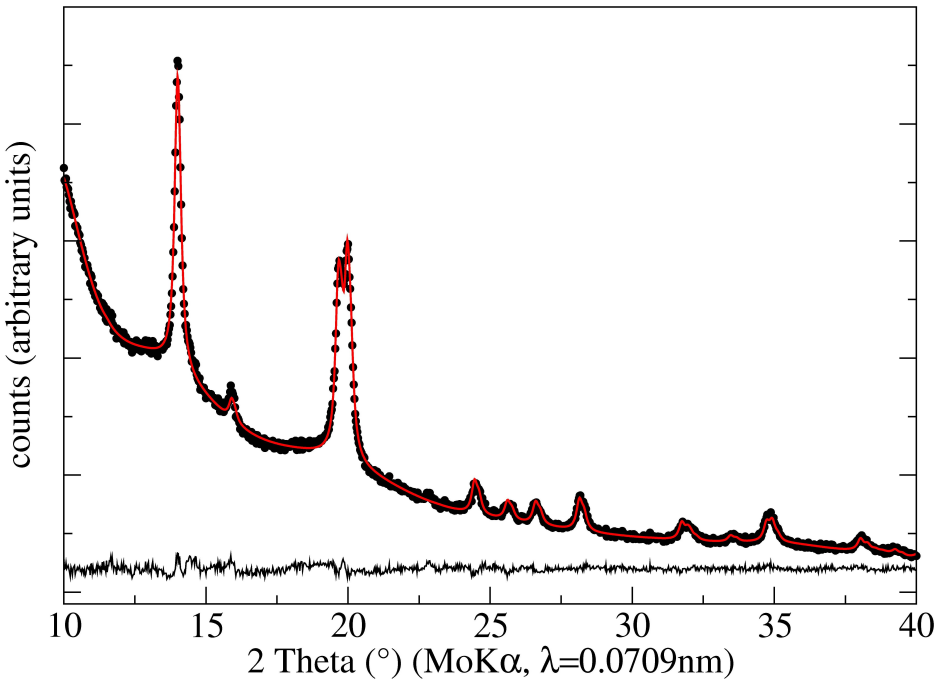

Figure 7.2: X-ray diffraction (experimental data: black dots), Rietveld fit (red line) and corresponding difference plot (black line) obtained using MoKα radiation.

Full pattern profile refinement was performed with TOPAS Academic V 4.1 [95] according to the structure model by Holseth and Kjekshus [101] applying the fundamental parameter approach.

Table 7.1: Crystallographic data of the refined $Fe_{1+x}Sb$ structure.

Lattice constants	
a/Å	4.1010(7)
b/Å	4.1010(7)
c/Å	5.146(1)
Space group	$P63/mmc$
Crystal size/nm	18.8
R_{wp}	2.514
gof	1.855

Table 7.2: Atomic coordinates, site occupancy factors and isotropic temperature factors.

	x	y	z	sof	beq
Fe1	0	0	0	Fe 1	3.91(4.19)
Fe2	$\frac{1}{3}$	$\frac{2}{3}$	$\frac{3}{4}$	Fe 0.256(8)	3.91(4.19)
Sb	$\frac{1}{3}$	$\frac{2}{3}$	$\frac{1}{4}$	Sb 1	3.91(4.19)

All atoms are located on special positions, thus only the lattice parameters, crystallite size, scale factor, one overall displacement parameter and the site occupation factor of Fe2 were refined. Due to the strong correlation between site occupation factors and displacement parameters the overall displacement parameter is not significant within the interval of 1 e.s.d.. Yet, the data clearly indicate a significant occupation of the interstitial position ($\frac{1}{3}$ $\frac{2}{3}$ $\frac{3}{4}$), see tables 7.1 and 7.2.

7.2.3 Electron microscopy

Transmission electron microscopy images (figure 7.3) show nanoparticles with sizes between approximately 20 nm and 50 nm. Despite intensive sonication during TEM sample preparation, individual crystals were never observed and even the smallest aggregates consisted of several crystals. The inset in figure 7.3 exhibits a single $Fe_{1+x}Sb$ particle at the edge of a larger agglomerate.

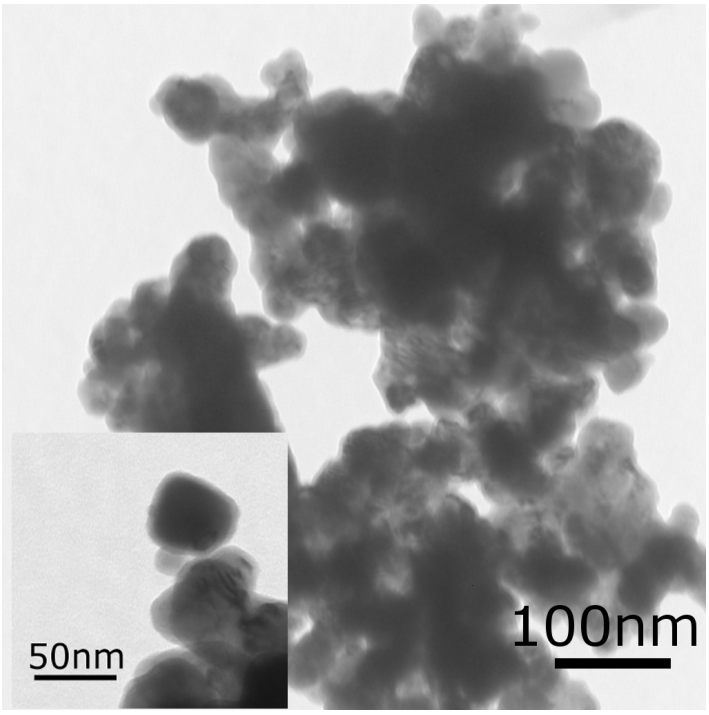

Figure 7.3: TEM micrograph of agglomerates of $Fe_{1+x}Sb$ nanoparticles, inset showing a single particle.

7.2.4 ^{57}Fe-Mößbauer

^{57}Fe-Mößbauer data of the nanoparticular $Fe_{1+x}Sb$ compound are presented in figure 7.4 a) and compared to a reference sample[1] (figure 7.4 b) pointing towards the presence of $Fe_{1+x}Sb$. The reference sample contains a $FeSb_2$ impurity (blue line).
At least two impurity phases (blue and purple fit) in the as prepared compound, which did not show up in the XRD data, can be detected next to the FeSb phase (red fitting curve). One of these impurities, in purple, exhibits magnetic hyperfine splitting, but identification of the phase (likely metallic iron) will require further data acquisition with a larger velocity range. Other likely impurities are superparamagnetic iron oxide and minor amounts of $FeSb_2$, both phenomenologically modeled by the blue line.

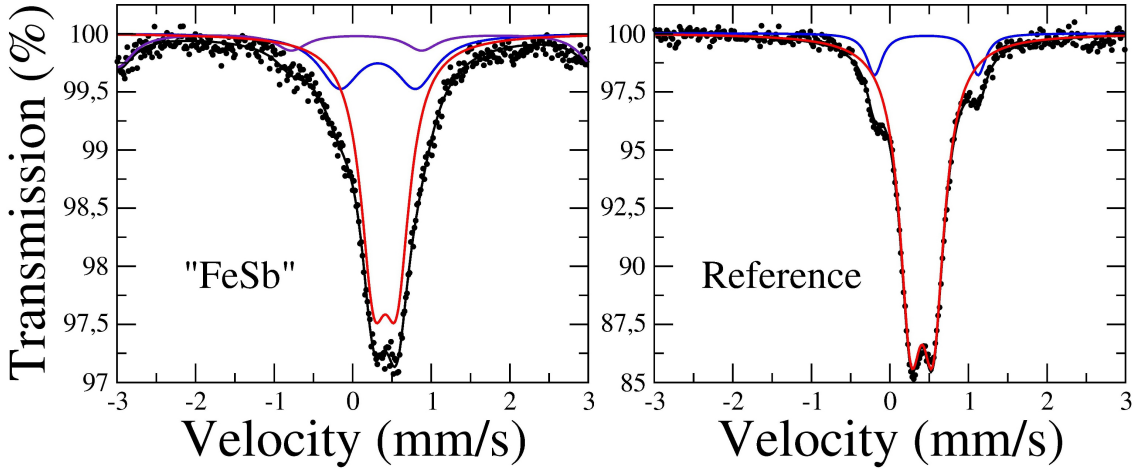

Figure 7.4: ^{57}Fe-Mößbauer data of the $Fe_{1+x}Sb$ sample (a) and reported data on FeSb as a reference (b).

[1] unpublished data by Gérard and Grandjean, Université de Liége

7.3 ZnSb - Results and discussion

7.3.1 Synthesis

$ZnCl_2$ (anhydrous, 98%, ABCR) was first dried with thionylchloride, washed with toluene, dried *in vacuo* and stored in a glovebox under N_2 atmosphere. Tetrahydrofuran was dried with $CaCl_2$ and Na/K and freshly distilled before use. Lithium triethylboronhydride Li[Et_3BH] (Aldrich, 1 M in THF, referred to as "superhydride"), and $SbCl_3$ (99%, ABCR) were used as obtained, $SbCl_3$ was stored in a glove box. Trioctylamine (Aldrich) was degassed and stored under Ar before use.

Zn particles were synthesized by reaction of $ZnCl_2$ with 2 equivalents of the 1 M solution of "superhydride" in THF at ca. 65°C. The particles were washed several times with THF, dried *in vacuo* and stored in a glovebox. Sb particles were produced by reducing $SbCl_3$ with 3 equivalents of the 1 M "superhydride" solution at room temperature. The black particles were repeatedly re-dispersed in THF and decanted from the solution, dried *in vacuo* and kept in a glove box.

Both, Zn and Sb nanoparticles, are highly reactive in ambient air leading primarily to the oxides. ^{1}H NMR data of Sb nanoparticles kept in inert gas atmosphere show an intense signal according to surface bond stibane ($\delta \approx 1.05$ ppm, c.f. figure 3.1 in chapter 3) which broadens, when the particles were in contact with air.

The activated elements were heated to 300°C at a rate of ca. 20 K/min in a polar strongly coordinating solvent (trioctylamine) in order to prevent nanoparticle aggregation. The reaction mixture was held at ca. 300°C for 60 min before it was allowed to cool down. Products were collected by centrifugation, washed with ethanol and subsequently dried *in vacuo*.

The syntheses had to be carried out using an excess (3:1) of zinc metal to ensure all Sb reacts to form the desired product. The additional Zn can be removed after the reaction by repeated treatment of the solid residue with dilute acetic acid.

7.3.2 Powder X-ray diffraction

X-ray powder diffraction profiles recorded from the final product are shown in figure 7.5. Only a minor antimony impurity (2%) was detected.

Quantitative phase analyses were performed by means of full pattern profile analysis of the corresponding X-ray diffraction data according to the published structural data of ZnSb [96] and Sb [48], respectively, using Topas Academic V 4.1 [95].

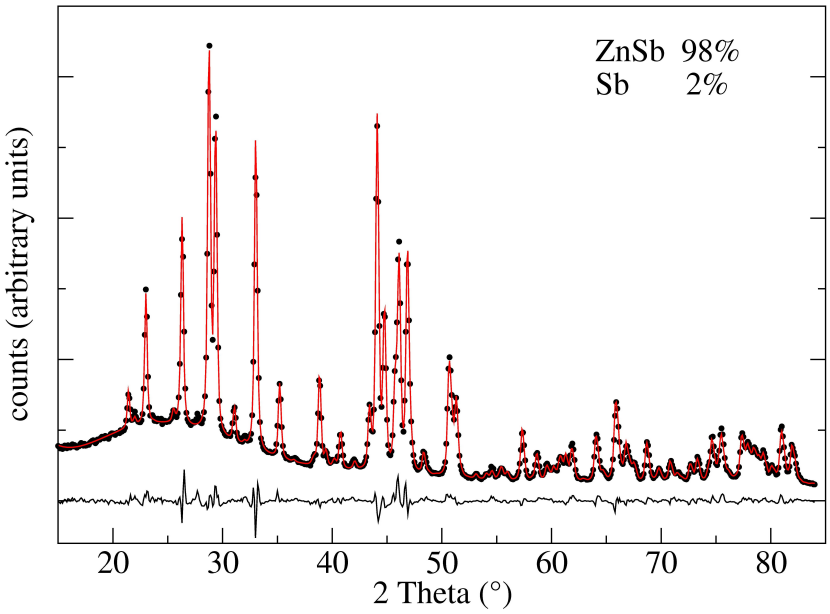

Figure 7.5: X-ray diffraction (experimental data: black dots), Rietveld refinements (red line) and corresponding difference plots (black line) of the final ZnSb product.

7.4 Conclusion

In this chapter, the syntheses of ZnSb and $Fe_{1+x}Sb$ nanoparticles, prepared similarly to $Zn_{1+x}Sb$ and $FeSb_2$, were reported. In the case of ZnSb, the refinement of the powder X-ray diffraction data shows an almost clean product with only 2% antimony impurity. Ongoing work includes further characterization and preparation of sufficient amounts of material to fabricate a pellet for thermoelectric measurements.

Time-dependent X-ray diffraction studies on $Fe_{1+x}Sb$ indicate that the phase forms at temperatures between 200°C and 250°C. The final product has also been measured using MoKα radiation since iron causes an increased background in the data obtained with CuKα radiation. Rietveld refinement of the XRD data has to be taken with care and only represent preliminary results. Due to the strong correlation between site occupation factors and displacement parameters the overall displacement parameter is not significant within the interval of 1 e.s.d.. Yet, the data clearly indicate a significant occupation of the interstitial position.

The evaluation of Automated diffraction tomography data is subject of ongoing work and is believed to provide a more detailed view on the exact structure of the $Fe_{1+x}Sb$ nanoparticles.

According to the powder XRD data, clean $Fe_{1+x}Sb$ nanoparticles were synthesized and the presence of the phase could unambiguously be shown by comparison with unpublished ^{57}Fe-Mößbauer data of bulk $Fe_{1+x}Sb$. However, those ^{57}Fe-Mößbauer measurements reveal additional impurity phases which probably result from the molecular iron precursor in the synthesis.

7.5 Experimental section

X-ray diffraction

X-ray powder diffraction data were recorded with a D8 Advance diffractometer equipped with a SolX energy dispersive detector in the range of $5 \leq 2\Theta/^\circ \leq 40$ (step size 0.025°) using unfiltered MoKα-radiation. In order to increase the S/N ratio, a total of six individual scans was summed. For this measurement the samples were prepared between two layers of Magic Scotch tape. Additionally, X-ray powder diffraction data were collected with a Bruker-AXS D8-Discover diffractometer in reflection geometry equipped with a HiStar detector using graphite monochromatized CuKα radiation. Samples were glued on top of glass and (111) silicon substrates, respectively, using VP/VA copolymer (vinylpyrrolidone/vinylacetate). Le Bail fits and Rietveld refinements were performed with TOPAS Academic V4.1 [95] applying the fundamental parameter approach.

TEM

For TEM investigations the sample was suspended in ethanol and dropped onto a carbon coated copper grid. The images were obtained using a Philips EM420 instrument with an acceleration voltage of 120 kV.

^{57}Fe-Mößbauer

Approximately 10-40 mg of the powder sample were mixed with boron nitride in order to obtain a homogeneous absorber. The mixture was filled densely into a titanium frame to prevent movement of the sample during the measurement.

The ^{57}Fe-Mößbauer spectra, at temperatures ranging from 90 to 295 K, were measured on a constant-acceleration spectrometer that utilized a rhodium matrix cobalt-57 source. The instrument was calibrated at 295 K with alpha-iron powder. The sample temperature in the Janis SV-300 cryostat was controlled with a Lake-Shore 330 temperature controller and a silicon diode mounted on the copper sample holder. The accuracy of the sample temperature is better than $\pm 1\%$.

Chapter 8

Synthesis of ZnSb nanorods and their characterization by Scanning electron microscopy

8.1 Introduction

Theoretical calculations predict factorial enhancements of the thermoelectric figure of merit of materials upon downsizing and shaping into nanorod/-tube and nanowire systems. The hollow tube channels have a strong phonon scattering effect and reduce the lattice thermal conductivity further due to the phonon blocking effect of their low-dimensional nature [111]. Boukai *et al.* combined theory and experiments to demonstrate that Si nanowires can be designed to achieve extremely increased thermoelectric efficiency [112]. They have shown that the temperature of the maximum efficiency can be tuned by changing the amount of doping and the nanowire size. Their theory predicts that this enhancement should also be found in other semiconductor systems due to phonon effects.

Most works on the synthesis of nanowires and nanorods include surfactant-assisted solvothermal techniques [113, 114] and electrodeposition into nanoscale inorganic templates [115–121].

In collaboration with Seoul National University, the synthesis of ZnSb nanorods/-wires was attempted using a template-assisted technique. The general idea and work plan included the following steps (see also scheme in figure 8.1): $Zn_{1+x}Sb$ nanoparticles are dispersed in an appropriate solvent and deposited into an anodized aluminum oxide (AAO) template or a polycarbonate template. The nanoparticle-AAO hybrid was then heated at temperatures between 150°C and 200°C in an oven allowing the conversion of $Zn_{1+x}Sb$ into ZnSb on the one hand and the nanorod growth on the other. Removal of the alumina template should then yield single nanorods/-wires.
Since the exact elemental composition of the rod-like structures has not been determined yet, the products are referred to as "Zn-Sb nanorods".

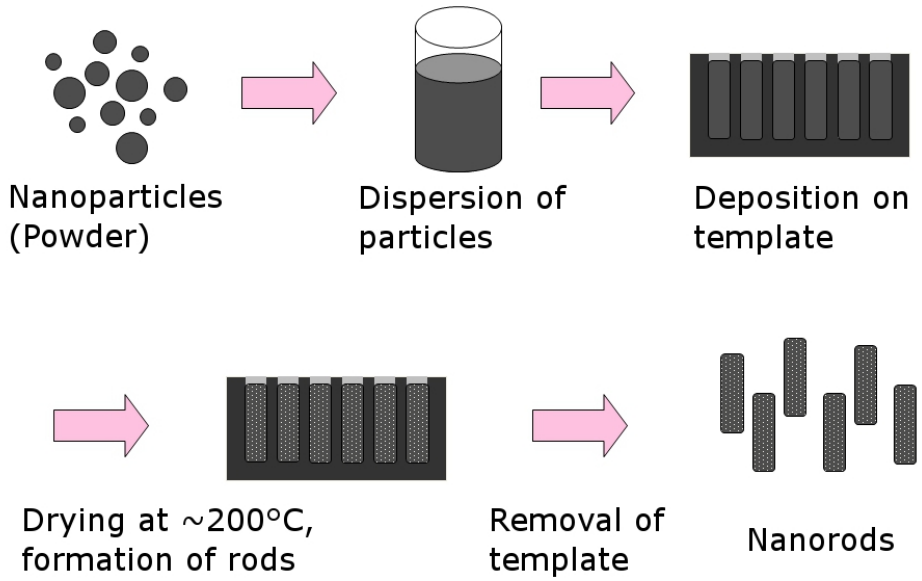

Figure 8.1: Scheme of the work plan for the formation of Zn-Sb nanorods.

8.2 Results and discussion

8.2.1 Synthesis

$Zn_{1+x}Sb$ nanoparticles were used "as prepared" according to the description in chapter 3. AAO templates with pore sizes of about 80 nm were prepared in the research group of Prof. Char (referred to as "self-made" AAO) following the synthetic route reported by Masuda et. al [122], AAO with pore diameters of around 200 nm (Anodisc 25 (200 nm)) and polycarbonate membranes with pore sizes of 800-1000 nm (Nuclepore Track-Etch Membrane) were obtained commercially (Whatman). The "self-made" AAO had a blocking layer of aluminum on the bottom, while the commercially available membranes are open on both sides. Scheme and Scanning electron microscopy images of the different templates are shown in figure 8.2. The commercially available AAO template and the polycarbonate template are similar except for the larger pore diameter of the polycarbonate membrane.

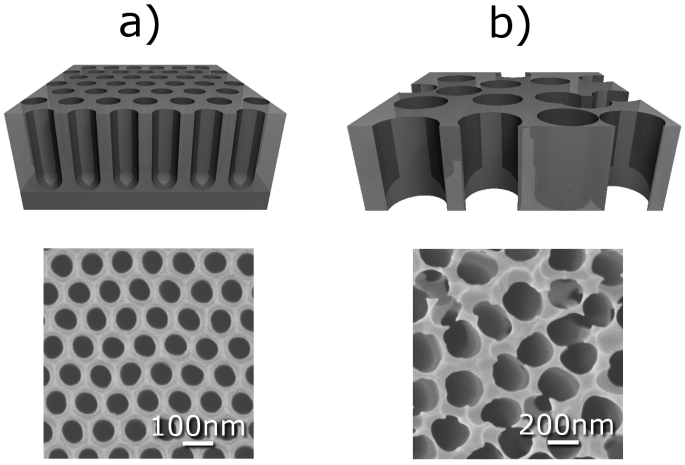

Figure 8.2: Scheme and SEM top view micrographs of (a) the "self-made" AAO template and (b) the commercially available AAO template. The polycarbonate membrane looks similar to the latter with non ordered pores of larger diameters.

In order to perform as many experiments as possible, the "self-made" AAO was cut into small pieces of about 0.5 cm^2. To follow the general work plan, different synthetic approaches were used to deposit the $Zn_{1+x}Sb$ nanoparticles into the various kinds of templates:

1. Particles were dispersed in an appropriate solvent (see below) and dropped onto the self-made AAO template.

2. The dispersion of the particles, together with the self-made AAO, was placed into an ultrasound bath.

3. The dispersion of the particles was pressed through the pores of the commercially available AAO membrane.

4. The $Zn_{1+x}Sb$ particles were functionalized with dopamine making them water-soluble and positively charged in aqueous solution. The pore walls of the polycarbonate membranes were modified with differently charged polyelectrolytes (PSS and PAH) and repeatedly filled with layers of polyelectrolytes and nanoparticles in an automated layer-by-layer dipping process. The idea was to increase the nanoparticle-pore wall interaction to drive more particles into the pores (see figure 8.3).

8.2.1.1 Deposition into AAO templates

Prior to all experiments, the suitable solvent was determined. The wetting behavior of different solvents (water, isopropanol, THF (SAMCHUN pure Chemical CO.)) on AAO was compared (figure 8.4), according to contact angle measurements.

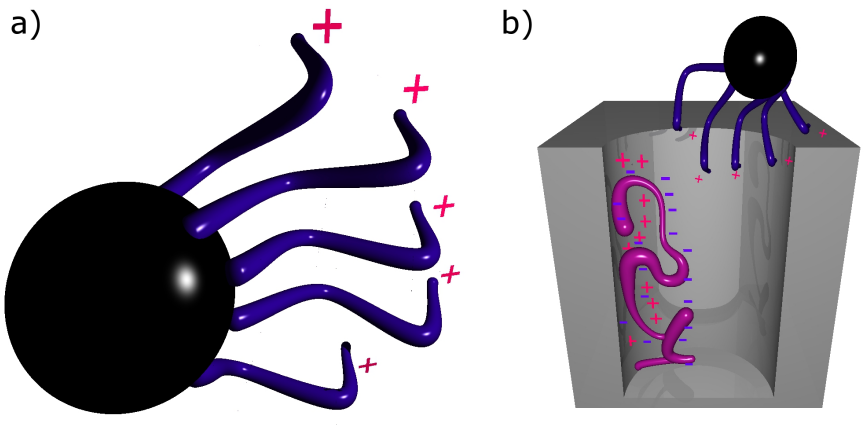

Figure 8.3: Scheme of (a) a functionalized nanoparticle with a positive charge on its surface and (b) a chemically modified pore wall attracting the functionalized nanoparticle.

Isopropanol was found to provide the smallest contact angle, spread most efficiently on the substrate and was therefore used as the solvent in the later experiments.

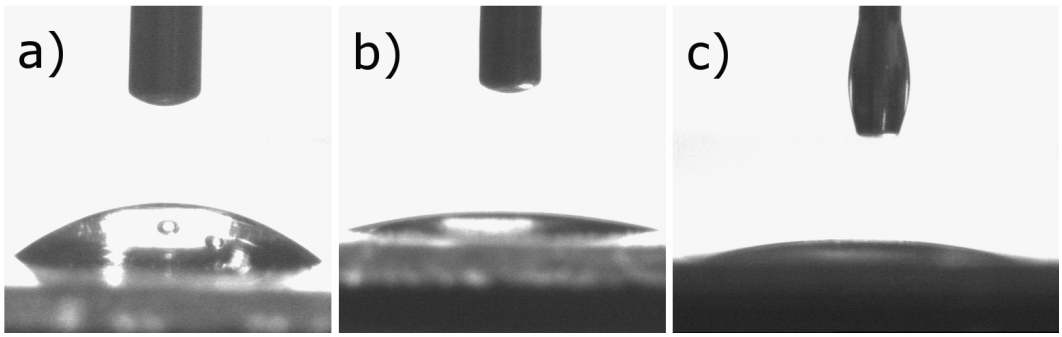

Figure 8.4: Contact angle measurements with three different solvents spreading on an AAO template, a) water, b) THF and c) isopropanol.

For the first three methods, $Zn_{1+x}Sb$ nanoparticles were dispersed in isopropanol with the help of an ultrasound bath. In a typical synthesis 2 mg of nanoparticles were dispersed in 1 ml of solvent and kept in the ultrasound bath for about 60 min. The obtained dispersion was either dropped onto a small piece of AAO or put into the ultrasound bath with a small piece of AAO.

For the pressure-assisted synthesis, the dispersion was filled into a 1 ml syringe and pressed through the pores of a commercially available AAO membrane using an infusion pump apparatus.

8.2.1.2 Deposition into polycarbonate membranes

To prepare the functionalized $Zn_{1+x}Sb$ nanoparticles, the powder was mixed with a solution of dopamine in hexane (SAMCHUN pure Chemical CO.) and kept in an ultrasound bath for 90 min. In a typical experiment, 15 mg of particles were mixed with 60 mg of dopamine hydrochloride (Aldrich) in 10 ml of hexane. Afterwards, 5 ml of water were added to 5 ml of the black solution. Figure 8.5 shows the process of transferring the functionalized particles into the aqueous solution, together with plain nanoparticles in a reference vial. Once the water was added, the organic layer holding the nanoparticles (black) floats on top of the aqueous phase. Shortly after, the functionalized nanoparticles (right) start to move into the lower layer which can be observed in figure 8.5 II+III. To drive all particles into the aqueous phase, the vial was shaken several times until the transfer was complete (figure 8.5 IV).

Two different polyelectrolyte solutions were used for the modification of the pore walls of the polycarbonate membranes. Aqueous polystyrene sulfonate (Aldrich) as well as aqueous polyallylamine hydrochloride (Aldrich) solutions were prepared by stirring 0.117 g NaCl with 0.2 g of either PSS or PAH in 200 ml water for 30 min. Structures of both molecules are shown in figure 8.6.

Using an automated layer-by-layer dipping process, several layers of these polymers were coated onto the pore walls.

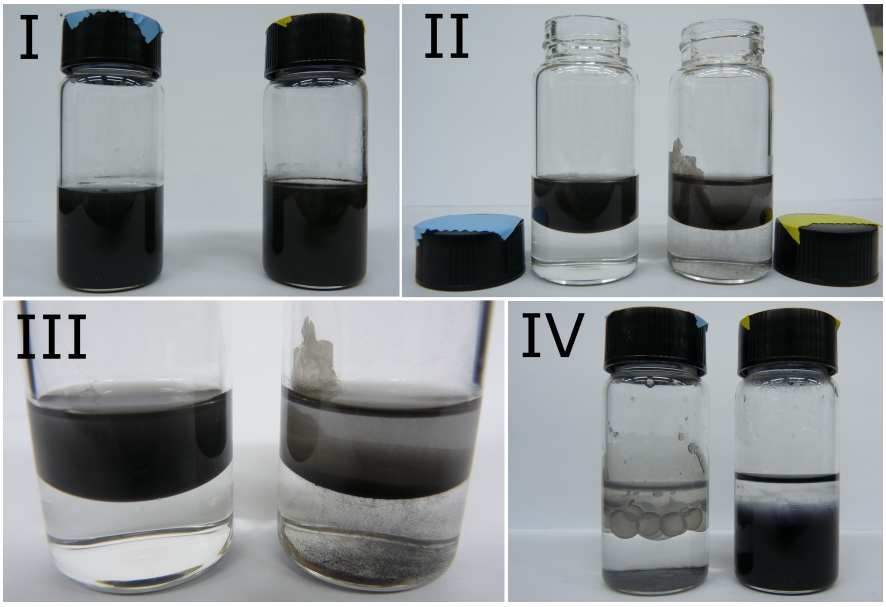

Figure 8.5: Solvation process of the dopamine-functionalized $Zn_{1+x}Sb$ nanoparticles in water (left:reference, right:sample), from solution in hexane (I), directly after adding water (II), after 2-3 minutes (III) and after shaking (IV).

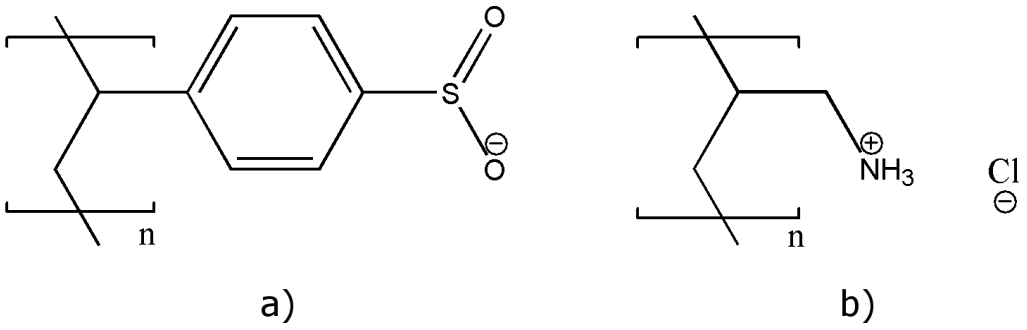

Figure 8.6: Structures of (a) polystyrene sulfonate (PSS) and (b) polyallylamine hydrochloride (PAH).

With several polyelectrolyte and nanoparticle layers, the pores of the "self-made" AAO templates turned out to be too narrow to hold enough nanoparticles which are also between 30 nm and 70 nm in diameter. Therefore, polycarbonate membranes with pore diameters of 800-1000 nm were used. The membrane was attached to a holder (yellow in figure 8.7) which moves vertically and horizontally. The membrane was automatically dipped into the polyelectrolyte solution for 30 min, rinsed with water for 5 min and again dipped into the oppositely charged polymeric solution.

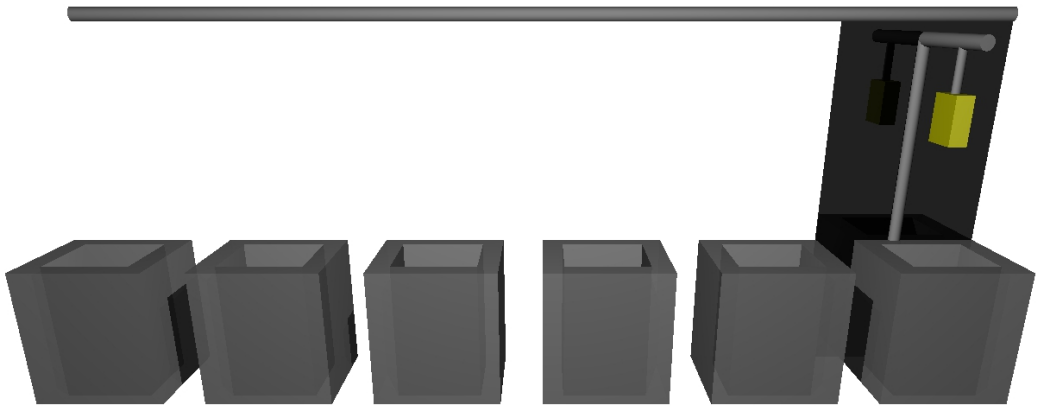

Figure 8.7: Scheme of the automated dipping machine used for the layer-by-layer deposition of different polyelectrolytes.

This process was repeated several times until four layers of each polymer had been attached. Following that step, the membrane was put into the aqueous nanoparticle solution and kept there for about 10 hours to allow the positively charges nanoparticles to attach to the polymers bound to the pore walls. After rinsing the membrane, more polyelectrolyte layers were added using layer-by-layer deposition, before the membrane was then subject to further nanoparticle treatment. The whole process was repeated one more time. The polymer layers were meant to increase electrostatic interactions between particles and pore walls and to function as a "glue"-like material holding the particles together.

8.2.1.3 Formation of rods and removal of the template

After the deposition of particles or particle-polymer mixtures into the membranes, they were put into an oven at temperatures of around 200°C for 10-12 hours. A phase change of the $Zn_{1+x}Sb$ nanoparticles into ZnSb accompanied by the formation of rods or wires was expected.

After cooling down, the membranes were subject to different kinds of Scanning electron microscopy. Top view images were obtained by simply attaching the membranes to an SEM sample holder. For cross-section images, the aluminum layer of the "self-made" AAO was removed using acetic $CuCl_2$ solution. To access free rods, the template was attempted to be removed through base treatment (scheme in figure 8.8). In a typical experiment the membrane was put into 5 M NaOH at 45°C for 5 min. After the AAO was dissolved, potential rods were collected by centrifugation (5000 rpm, 4°C, 5 min) and repeatedly washed with water. The solution was then dropped onto a Si waver and dried in a vacuum oven.

Figure 8.8: Scheme of the removal of the AAO template by NaOH treatment.

8.2.2 Electron microscopy

The appearance of all the samples after heating and further treatment (if applicable) was determined by electron microscopy.

8.2.2.1 AAO templates

To compare the dropping of the dispersion onto the template to the ultrasound-assisted method, top view images of the membranes were obtained. Figure 8.9 b) clearly shows more particles in the pores than figure 8.9 a) due to the ultrasound-assisted method. By using the "dropping method", only very few particles lying loosely on the surface could be found.

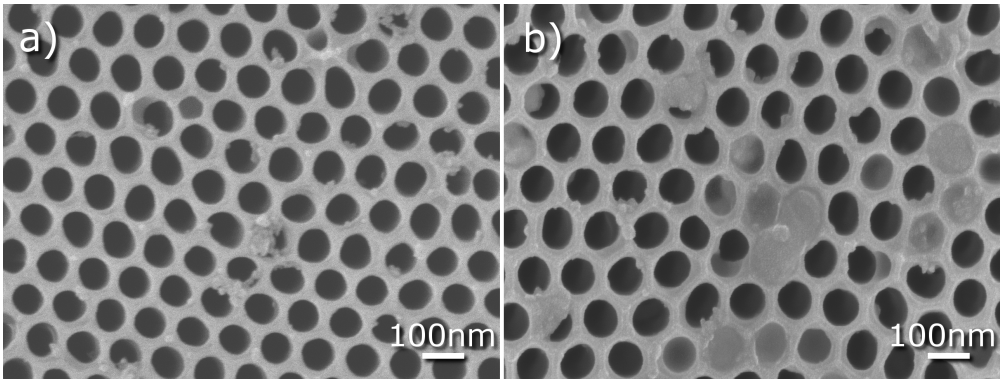

Figure 8.9: SEM topview image of particles deposited on AAO template by (a) dropping and (b) ultrasound-assisted technique.

Top view images of the templates can be misleading, since it is not certain whether the particles are only covering the top or have actually entered the pores. According to cross-section micrographs (figure 8.10 b), the pores are filled to a comparably high extent.

The AAO template was removed by base treatment and SEM images of the obtained structures on Si wavers are shown in figure 8.11.

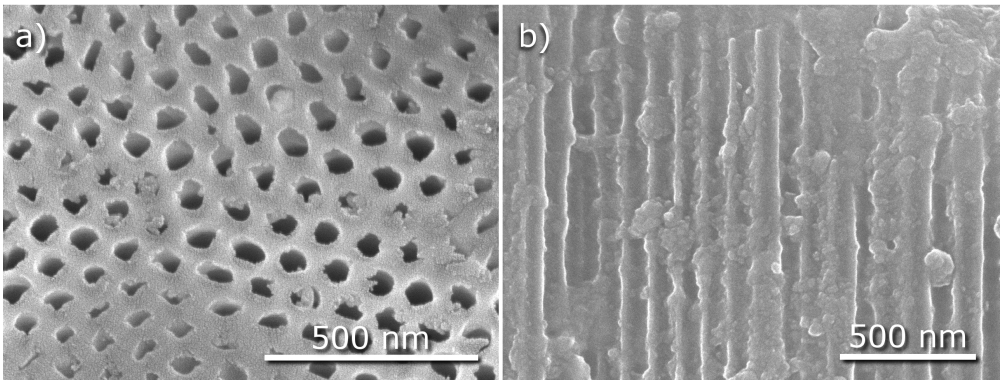

Figure 8.10: SEM topview (a) and sideview (b) images of the obtained templates after ultrasound-assisted synthesis.

Several rod-like structures can be found which seem to have broken since they do not resemble the whole length of the AAO pores. Upon closer look the intrinsic nanostructuring of the rods is apparent. This is a consequence of the synthetic method where $Zn_{1+x}Sb$ particles build up the anisotropic structures. Yet, the samples are not clean, since there are also agglomerates of particles next to the rod-like structures.

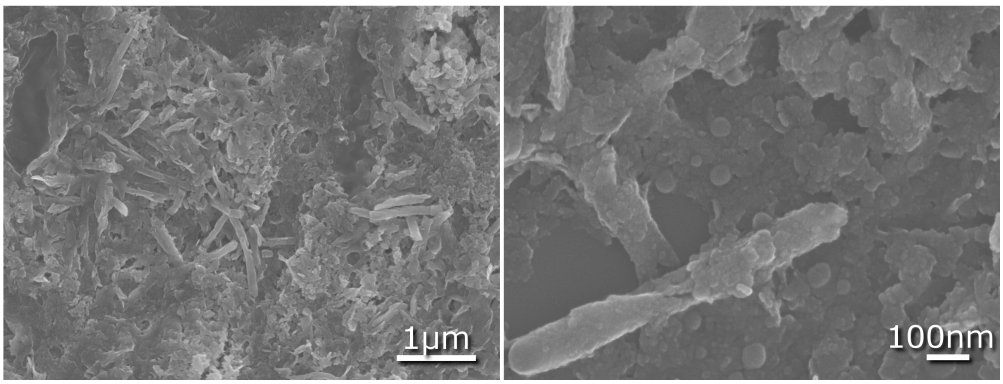

Figure 8.11: SEM images of the obtained Zn-Sb nanorods after removal of the AAO template through base treatment.

For the pressure-assisted synthesis, commercially available AAO with a pore diameter of about 200 nm was used. Side view images show that nanoparticles are distributed inside the pores. However, they are too far apart from each other to build structured materials (figure 8.12 a).

The removal of the template also proved to be far from trivial. The structures which were left after base treatment are shown in figure 8.12 b). What looked like needles, turned out to be broken AAO when a plain membrane was dissolved in NaOH as a reference.

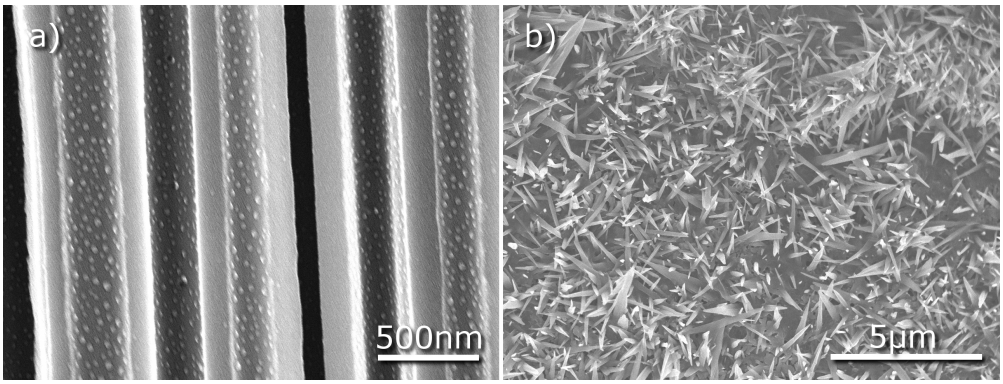

Figure 8.12: a) Sideview images of the nanoparticles in the pores of the commercial AAO template, b) broken AAO after the attempted removal of aluminum oxide with dilute base.

8.2.2.2 Polycarbonate membranes

The functionalization of the $Zn_{1+x}Sb$ nanoparticles started with some promising results when the particles could be transferred into the aqueous phase which increased their processibility significantly. TEM images show how the nanoparticles changed after the functionalization with dopamine (figure 8.13). The former heavily agglomerated particles (compare to figure 3.5 in chapter 3) were separated but exhibit a rougher surface. Having a positive charge on their surface in aqueous solution, they should be driven into negatively charged pores through electrostatic interactions. Top and bottom view of such templates are shown in figure 8.14 a+b). Through repeated layer-by-layer deposition of the polymers and treatment with aqueous nanoparticle solution, filled pores could be obtained.

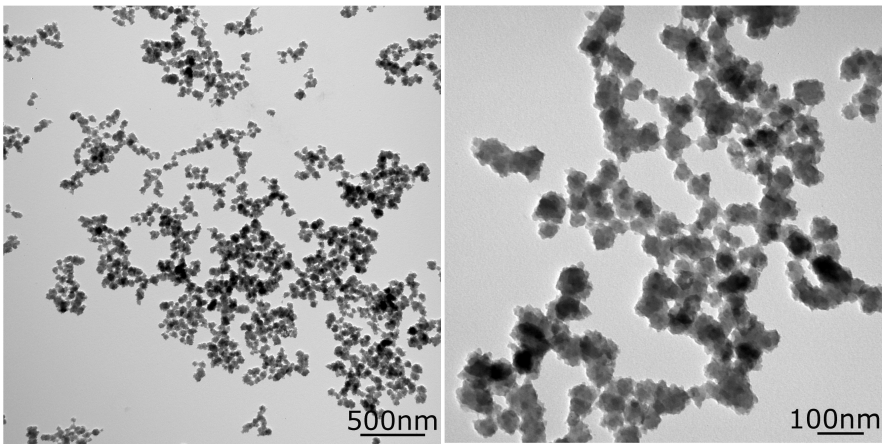

Figure 8.13: TEM micrographs of the dopamine-functionalized $Zn_{1+x}Sb$ nanoparticles.

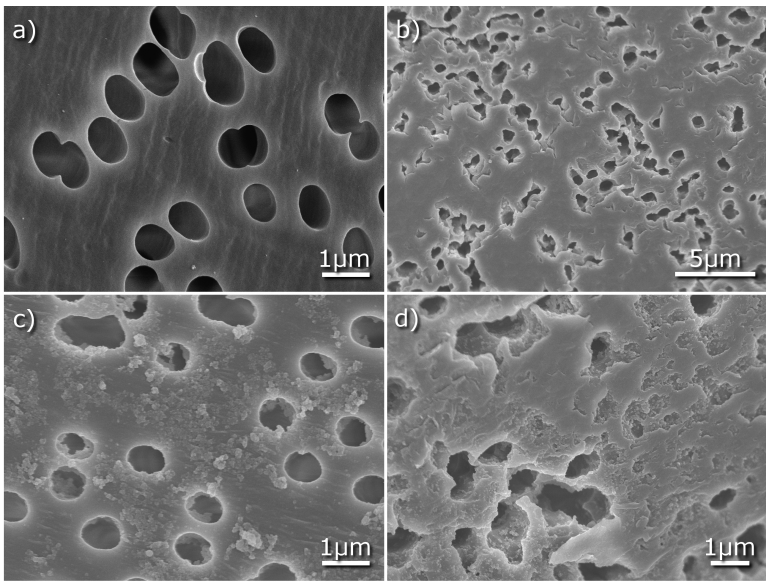

Figure 8.14: Top and bottom view of the polycarbonate membrane (a+b) and pores filled with particles and polyelectrolytes (c+d) after heating at 200°C.

8.3 Conclusion

The template-assisted synthesis of ZnSb nanorods has been attempted. Taking into account the metastability of the $Zn_{1+x}Sb$ nanoparticular phase, the work plan included the deposition of a dispersion of these nanoparticles onto a template, heating the template to induce decomposition into ZnSb and rod formation and removing the template to gain single nanorods. First results have been achieved through optimization of the different steps.

Contact angle measurements revealed that the most suitable solvent was isopropanol since it spreads efficiently on the template. The ultrasound-assisted deposition method onto the "self-made" AAO template was found to be most promising since the majority of particles entered the pores of the template. Cross-section SEM images proved this fact and some rod-like structures were obtained after removal of the AAO template by base treatment. The rods consisted of small particles and reflected the pore diameter of the template. Unfortunately, no clean samples consisting exclusively of nanorods were obtained. This could be the consequence of agglomerates also staying on the surface of the template and therefore not forming any anisotropic structures.

In order to increase the processibility of the nanoparticles and enhance the particle-pore wall interaction, their surface was functionalized with dopamine. It was demonstrated that this made the material water soluble and TEM micrographs showed less agglomerated structures. Besides, those functionalized particles were positively charged in aqueous solution. Separately, the pore walls of the polycarbonate membranes were modified with two differently charged polyelectrolyte (PSS and PAH) solutions by means of an automated layer-by-layer deposition process.

Through the attachment of different polymer layers and several layers of nanoparticles in alteration, the polyelectrolytes were meant to function as a "glue" to hold the particles together.
Top and bottom view SEM images of the obtained structures after heating show particles densely occupying the 800 nm pores of the polycarbonate membrane. This turned out to be promising and further optimization of this technique could yield even better results. However, removing the polycarbonate template turned out to be far from trivial, thus no rod-like structures have been obtained yet.

Future work will have to optimize the layer-by-layer deposition method to completely fill the pores of the membrane. Removal of the templates, AAO as well as polycarbonate, also needs further exploring in order to gain samples exclusively consisting of rod-like structures. Once nanorods/-wires are obtained, additional characterization is needed, including e.g. phase analysis by X-ray diffraction methods.

8.4 Experimental section

Scanning electron microscopy

The samples were attached to the brass sample holder with an adhesive carbon tape, either on top of it for top view images or tilted by 90° for the cross-section images. A 1 nm thick platinum layer was sputtered onto the samples using a Cressington (208HR) coater to ensure good conductivity of the surfaces. SEM images were obtained using a JEOL JSM-6701F.

Contact angle measurements

Contact angle measurements were performed using a KRUSS-DSA100.

Pump infusion

For the pressure-assisted synthesis, a PHD 2000 Infuse/Withdraw pump (Harvard Apparatus) was used. An infusion speed of 40-50 ml/min was applied for pressing the solution through the membranes.

Chapter 9

Summary and outlook

The main part of this work covers the wet chemistry synthesis of nanoscale zinc and iron antimonides, "Zn_4Sb_3", ZnSb, $FeSb_2$ and $Fe_{1+x}Sb$. The motivation lies in the application of most of these compounds in thermoelectric devices, which can convert between thermal and electrical energy, offering an elegant way to harvest waste heat for example. Their conversion efficiency is determined by the dimensionless figure of merit ZT which includes the Seebeck coefficient, electrical conductivity and thermal conductivity. By downsizing to the nanoscale, the thermal transport is decreased due to phonon scattering on the interfaces between the nanoparticles. This approach was the motivation of this work.

In *Chapter 3*, the novel synthesis of "Zn_4Sb_3" has been reported using Sb and Zn nanoparticles as starting materials. The phase formation has been investigated by time-dependent X-ray diffraction data. The X-ray diffraction data of the final product are perfectly in line with the data of "Zn_4Sb_3". However, TEM data show the presence of at least two crystalline phases.

This raises the fundamental question how powerful and reliable structure determinations based on X-ray powder diffraction for nanomaterials with complex structures and mixtures really are. A detailed diffraction technique, Automated electron tomography (ADT), allowed further insight into the phases and revealed the presence of a hitherto unknown phase, $Zn_{1+\delta}Sb$. Structurally, this new phase resembles some motifs from the known "Zn_4Sb_3" compound, such as the framework composed of single antimony anions and antimony dumbbells. However, additional antimony dumbbells can be found perpendicular to the ones along the c-axis.

In *Chapter 4*, the results for the characterization of the obtained pellets are presented. A combined batch of $Zn_{1+x}Sb$ nanoparticles has been divided into four equal parts and sintered using different Spark plasma sintering conditions. Knowing of the phase instability above 200°C sintering temperatures below 200°C and short sintering times of four to six minutes have been chosen. The "$Zn_{1+x}Sb$" workpieces have been subject to two different X-ray diffraction studies: Some loose powder was scratched off their surfaces and has been subject to regular powder X-ray diffraction, while small pieces of the pellets have been subject to high-energy synchrotron radiation also showing their interior composition. Already the surface composition showed major decomposition which becomes more prominent the higher the sintering temperatures were. Inside the pellets, higher contents of the decomposition products, ZnSb, Zn and ZnO, can be found.

The density and morphology of the samples have been determined by means of Laser microscopy and Scanning electron microscopy. The density has been found to be only 50% of the bulk value of "Zn_4Sb_3" and the SEM images reveal rather porous structures with many voids and cracks. However, the nanostructuring seems to be maintained during the sintering process which would be crucial for possibly decreased thermal conductivity.

Another requirement for handling and characterization of the workpieces is some good mechanical strength. Unfortunately, the obtained "$Zn_{1+x}Sb$" pellets were not robust enough and broke when cut prior to the thermoelectric measurements. Heat capacity measurements show a deviation from the Debye law at low temperatures due to the nanosize of the samples.

In *Chapter 5*, the novel synthesis of $FeSb_2$ nanoparticles is reported. Similarly to the synthesis of $Zn_{1+x}Sb$, antimony nanoparticles were used as a starting material. They were reacted with a molecular iron precursor, cyclopentadienyl iron(II) dicarbonyl dimer, decomposing at around 130°C. Time-dependent X-ray diffraction data reveal the phase to form between 200°C and 250°C. Intermediate products have also been investigated by ^{57}Fe-Mößbauer measurements. While XRD data show the presence of crystalline phases, ^{57}Fe-Mößbauer is sensitive to any iron containing species. Weak signals are found in the samples taken at early stages of the reaction, when XRD data show crystalline antimony, exclusively. These weak signals correspond to weakly bound iron in molecular compounds, as cyclopentadienyl iron(II) dicarbonyl dimer and its primary decomposition products.
The phonon density of states has been determined by Nuclear inelastic scattering and has been compared to bulk values. Reduced phonon DOS shows an increased Debye level at low temperatures. The velocity of sound, determined from this data, shows a decrease for the nanostructured material.

In *Chapter 6*, the results for the characterization of the solidified materials are presented. Two pellets have been sintered under different sintering conditions with temperatures of 200°C and 250°C, respectively. Surface composition, determined by XRD data of powder scratched off the surfaces, has revealed no decomposition during sintering.

However, ^{57}Fe-Mößbauer data of the pellets show the presence of an impurity phase, possibly iron oxide, in both pellets. The decomposition is most prominent for the workpiece sintered at higher temperatures which consists only to ca. 50% of the original $FeSb_2$ phase.

SEM and Laser microscopy images show porous structures with densities between 50% and 60% of the bulk value, whereas the nanostructuring has been maintained. Heat capacity measurements show a deviation from the Debye law at low temperatures due to the nanosize of the samples.

A complete set of thermoelectric measurements has only been obtained from the pellet which had been sintered at 200°C. Due to radically increasing resistivities at low temperatures, the Seebeck coefficient could not be determined in that temperature region. However, the thermal conductivity was found to be reduced drastically. Unfortunately, these low numbers cannot balance out the small power factor only leading to ZT values in the order of 10^{-5}.

The resistivity of the second pellet sintered at higher temperatures, is lower which could be due to a slightly higher density. Unfortunately, the remaining thermoelectric data could not be obtained since the workpiece broke after contacting. It can only be assumed that higher ZT values would be reached, if similar Seebeck coefficients and thermal conductivities had been found.

Chapter 7 describes the ongoing work on the ZnSb and $Fe_{1+x}Sb$ compounds. The synthesis of both materials could be optimized based on the findings of the previous chapters. Comparing the obtained XRD data of the $Fe_{1+x}Sb$ phase to literature data, it has been assumed that a clean sample has been prepared. ^{57}Fe-Mößbauer data, however, show at least two impurity phases in the product.

Rietveld refinement of XRD data measured with MoKα radiation of the final $Fe_{1+x}Sb$ phase are still subject of ongoing examination.

Automated diffraction tomography data are also currently evaluated and are hoped to allow a deeper insight into the exact crystal structure of $Fe_{1+x}Sb$.

In *Chapter 8*, the template-assisted synthesis of anisotropic structures of ZnSb has been attempted. The previously obtained $Zn_{1+x}Sb$ nanoparticles have been filled into various kinds of inorganic membranes via different methods. Through heat treatment the $Zn_{1+x}Sb$ nanoparticles were meant to transform into ZnSb forming nanorods. After removal of the template, some rod-like structures, but no clean samples, have been observed. The step of dissolving the template without destroying the formed anisotropic structures is still subject of ongoing work.

In summary, synthetic routes towards nanoparticles of thermoelectric antimonides have been optimized. Detailed characterization techniques have revealed a hitherto unknown Zn-Sb phase and have allowed insight into the presence of impurity phases which have not been detected by regular X-ray diffraction data. The solidification process, performed by Spark plasma sintering, has turned out to be a crucial step in the fabrication of thermoelectric devices. Intensive characterization by means of XRD and ^{57}Fe-Mößbauer studies, has revealed the decomposition of the solidified materials. Beside the phase stability, the processibility of the obtained workpieces is a key requirement to obtain thermoelectric data. Almost all of them have not been robust enough mechanically for the treatment necessary prior to the measurement of their transport properties.
Dealing with these challenges will be a crucial subject in future projects.

References

[1] T. Caillat, J. P. Fleurial, and A. Borshchevsky. Preparation and thermoelectric properties of semiconducting Zn_4Sb_3. *Journal of Physics and Chemistry of Solids*, 58(7):1119–1125, 1997.

[2] P. J. Shaver and J. Blair. Thermal and electronic transport properties of rho-type ZnSb. *Physical Review*, 141(2):649–663, 1966.

[3] L. T. Zhang, M. Tsutsui, K. Ito, and M. Yamaguchi. Effects of ZnSb and Zn inclusions on the thermoelectric properties of beta-Zn_4Sb_3. *Journal of Alloys and Compounds*, 358(1-2):252–256, 2003.

[4] V. S. Arunachalam and E. L. Fleischer. Harnessing materials for energy - Preface. *Materials Research Bulletin*, 33(4):261–263, 2008.

[5] V. S. Arunachalam and E. L. Fleischer. The global energy landscape and materials innovation. *MRS Bulletin*, 33(4):264–276, 2008.

[6] Illustration of the Energy Landscape, "Harnessing Materials for Energy". *MRS Bulletin*, 33(4), 2008.

[7] N. W. Ashcroft and N. D. Mermin. *Solid State Physics*. Harcourt College Publishers, 1976.

[8] D. M. Rowe (ed.). *Thermoelectrics Handbook - Macro to Nano*. CRC, Boca Raton, 2006.

[9] F. J. DiSalvo. Thermoelectric cooling and power generation. *Science*, 285(5428):703–706, 1999.

[10] G. A. Slack. *CRC Handbook of Thermoelectrics*. CRC, Boca Raton, 1995.

[11] G. J. Snyder and E. S. Toberer. Complex thermoelectric materials. *Nature Materials*, 7(2):105–114, 2008.

[12] B. C. Sales, D. Mandrus, and R. K. Williams. Filled skutterudite antimonides: A new class of thermoelectric materials. *Science*, 272(5266):1325–1328, 1996.

[13] G. S. Nolas, D. T. Morelli, and T. M. Tritt. Skutterudites: A phonon-glass-electron crystal approach to advanced thermoelectric energy conversion applications. *Annual Review of Materials Science*, 29:89–116, 1999.

[14] H. J. Goldsmid. *Thermoelectric Refrigeration*. Plenum Press, New York, 1988.

[15] F. D. Rosi. Thermoelectricity and thermoelectric power generation. *Solid-State Electronics*, 11(9):833–848, 1968.

[16] R. R. Heikes and Ure R. W. *Thermoelectricity: Science and Energy*. Interscience, New York, 1961.

[17] Y. Gelbstein, Z. Dashevsky, and M. P. Dariel. High performance n-type PbTe-based materials for thermoelectric applications. *Physica B-Condensed Matter*, 363(1-4):196–205, 2005.

[18] C. Wood. Materials for thermoelectric energy conversion. *Reports on Progress in Physics*, 51(4):459–539, 1988.

[19] K. F. Hsu, S. Loo, F. Guo, W. Chen, J. S. Dyck, C. Uher, T. Hogan, E. K. Polychroniadis, and M. G. Kanatzidis. Cubic $AgPb_mSbTe_{2+m}$: Bulk thermoelectric materials with high figure of merit. *Science*, 303(5659):818–821, 2004.

[20] E. A. Skrabek and D. S. Trimmer. *CRC Handbook of Thermoelectrics*. CRC, Boca Raton, 1995.

[21] H. J. Goldsmid and A. W. Penn. Boundary scattering of phonons in solid solutions. *Physics Letters A*, A 27(8):523–524, 1968.

[22] D. P. Spitzer. Lattice thermal conductivity of semiconductors. A chemical bond approach. *Journal of Physics and Chemistry of Solids*, 31(1):19–40, 1970.

[23] E. S. Toberer, A. F. May, and G. J. Snyder. Zintl Chemistry for Designing High Efficiency Thermoelectric Materials. *Chemistry of Materials*, 22(3):624–634, 2010.

[24] L. D. Hicks and M. S. Dresselhaus. Effect of quantum-well structures on the thermoelectric figure of merit. *Physical Review B*, 47(19):12727–12731, 1993.

[25] L. D. Hicks, T. C. Harman, and M. S. Dresselhaus. Use of quantum-well superlattices to obtain a high figure of merit fron non-conventional thermoelectric materials. *Applied Physics Letters*, 63(23):3230–3232, 1993.

[26] R. Venkatasubramanian, E. Siivola, T. Colpitts, and B. O'Quinn. Thin-film thermoelectric devices with high room-temperature figures of merit. *Nature*, 413(6856):597–602, 2001.

[27] T. C. Harman, P. J. Taylor, M. P. Walsh, and B. E. LaForge. Quantum dot superlattice thermoelectric materials and devices. *Science*, 297(5590):2229–2232, 2002.

[28] Y. Kimura and A. Zama. Thermoelectric properties of p-type half-Heusler compound HfPtSn and improvement for high-performance by Ir and Co additions. *Applied Physics Letters*, 89(17), 2006.

[29] P. F. R. Poudeu, J. D'Angelo, A. D. Downey, J. L. Short, T. P. Hogan, and M. G. Kanatzidis. High thermoelectric figure of merit and nanostructuring in bulk p-type $Na_{1-x}Pb_mSb_yTe_{m+2}$. *Angewandte Chemie-International Edition*, 45(23):3835–3839, 2006.

[30] G. S. Nolas, J. L. Cohn, G. A. Slack, and S. B. Schujman. Semiconducting Ge clathrates: Promising candidates for thermoelectric applications. *Applied Physics Letters*, 73(2):178–180, 1998.

[31] V. Keppens, D. Mandrus, B. C. Sales, B. C. Chakoumakos, P. Dai, R. Coldea, M. B. Maple, D. A. Gajewski, E. J. Freeman, and S. Bennington. Localized vibrational modes in metallic solids. *Nature*, 395(6705):876–878, 1998.

[32] L. D. Hicks, T. C. Harman, X. Sun, and M. S. Dresselhaus. Experimental study of the effect of quantum-well structures on the thermoelectric figure of merit. *Physical Review B*, 53(16):R10493, 1996.

[33] M. Martin-Gonzalez, G. J. Snyder, A. L. Prieto, R. Gronsky, T. Sands, and A. M. Stacy. Direct electrodeposition of highly dense 50 nm $Bi_2Te_{3-y}Se_y$ nanowire arrays. *Nano Letters*, 3:973–977, 2003.

[34] J. C. Caylor, K. Coonley, J. Stuart, T. Colpitts, and R. Venkatasubramanian. Enhanced thermoelectric performance in PbTe-based superlattice structures from reduction of lattice thermal conductivity. *Applied Physics Letters*, 87(2), 2005.

[35] Ravi V. A. Ikeda, T. and G. J. Snyder. Evaluation of true interlamellar spacing from microstructural observations. *Journal of Materials Research*, 23(9):2538–2544, 2008.

[36] T. Ikeda, L. A. Collins, V. A. Ravi, F. S. Gascoin, S. M. Haile, and G. J. Snyder. Self-assembled nanometer lamellae of thermoelectric PbTe and Sb_2Te_3 with epitaxy-like interfaces. *Chemistry of Materials*, 19(4):763–767, 2007.

[37] C. J. Vineis, A. Shakouri, A. Majumdar, and M. G. Kanatzidis. Nanostructured Thermoelectrics: Big Efficiency Gains from Small Features. *Advanced Materials*, 22(36):3970–3980, 2010.

[38] S. Bhattacharya, R. P. Hermann, V. Keppens, T. M. Tritt, and G. J. Snyder. Effect of disorder on the thermal transport and elastic properties in thermoelectric Zn_4Sb_3. *Physical Review B*, 74(13), 2006.

[39] V. Y. Shevchenko, V. A. Skripkin, Y. A. Ugai, and T. A. Marshakova. *Izv. Akad. Nauk SSSR, Neorg. Mater.*, 4:1359–1360, 1968.

[40] Y. A. Ugai, T. A. Marshakova, V. Y. Shevchenko, and N. P. Demina. *Izv. Akad. Nauk SSSR, Neorg. Mater.*, 5:1381–1385, 1969.

[41] G. Vuillard and J. P. Piton. Sur les transformation des phases intermetalliques du systeme antimoine-zinc. *Comptes Rendus Hebdomadaires Des Seances De L´Academie Des Sciences Serie C*, 263(17):1018, 1966.

[42] G. B. Bokii and R. F. Klevtsova. *Zh. Strukt. Khim.*, 6:866–871, 1965.

[43] H. W. Mayer, I. Mikhail, and K. Schubert. Phases of ZnSb and CdSb mixtures. *Journal of the Less-Common Metals*, 59(1):43–52, 1978.

[44] M. Tapiero, S. Tarabichi, J. G. Gies, C. Noguet, J. P. Zielinger, M. Joucla, J. L. Loison, M. Robino, and J. Herion. Preparation and characterization of Zn_4Sb_3. *Solar Energy Materials*, 12(4):257–274, 1985.

[45] S. Elliott. *The Physics and Chemistry of Solids*. Wiley and Sons, Chichester, 1998.

[46] G. J. Snyder, M. Christensen, E. Nishibori, T. Caillat, and B. B. Iversen. Disordered zinc in Zn_4Sb_3 with phonon-glass and electron-crystal thermoelectric properties. *Nature Materials*, 3(7):458–463, 2004.

[47] F. Cargnoni, E. Nishibori, P. Rabiller, L. Bertini, G. J. Snyder, M. Christensen, C. Gatti, and B. B. Iversen. Interstitial Zn atoms do the trick in thermoelectric zinc antimonide, Zn_4Sb_3: A combined maximum entropy method X-ray electron density and ab initio electronic structure study. *Chemistry-a European Journal*, 10(16):3862–3870, 2004.

[48] Y. Mozharivskyj, A. O. Pecharsky, S. Bud'ko, and G. J. Miller. Promising thermoelectric material: Zn_4Sb_3 or $Zn_{6-delta}Sb_5$. Its composition, structure, stability,

and polymorphs. Structure and stability of $Zn_{1-delta}Sb$. *Chemistry of Materials*, 16(8):1580–1589, 2004.

[49] J. Nylen, M. Andersson, S. Lidin, and U. Häussermann. The structure of alpha-Zn_4Sb_3: Ordering of the phonon-glass thermoelectric material beta-Zn_4Sb_3. *Journal of the American Chemical Society*, 126(50):16306–16307, 2004.

[50] Y. Mozharivskyj, Y. Janssen, J. L. Harringa, A. Kracher, A. O. Tsokol, and G. J. Miller. $Zn_{13}Sb_{10}$: A structural and Landau theoretical analysis of its phase transitions. *Chemistry of Materials*, 18(3):822–831, 2006.

[51] J. Nylen, S. Lidin, M. Andersson, H. Liu, N. Newman, and U. Häussermann. Effect of metal doping on the low-temperature structural behavior of thermo electric beta-Zn_4Sb_3. *Journal of Solid State Chemistry*, 180:2603–2615, 2007.

[52] J. Nylen, S. Lidin, M. Andersson, B. B. Iversen, H. X. Liu, N. Newman, and U. Häussermann. Low-temperature structural transitions in the phonon-glass thermoelectric material beta-Zn_4Sb_3: Ordering of Zn interstitials and defects. *Chemistry of Materials*, 19(4):834–838, 2007.

[53] W. Schweika, R. P. Hermann, M. Prager, J. Persson, and V. Keppens. Dumbbell rattling in thermoelectric zinc antimony. pages 125501–1 – 125501–4, 2007.

[54] K. E. Almin. The crystal structure of CdSb and ZnSb. *Acta Chemica Scandinavica*, 2(5-6):400–407, 1948.

[55] A. S. Mikhaylushkin, J. Nylen, and U. Häussermann. Structure and bonding of zinc antimonides: Complex frameworks and narrow band gaps. *Chemistry - A European Journal*, 11(17):4912–4920, 2005.

[56] D. Boa, S. Hassam, J. Rogez, and K. P. Kotchi. The iron-antimony system: enthalpies of formation of the $FeSb_2$ and ϵ-FeSb phases. *Journal of Alloys and Compounds*, 365(1-2):228–232, 2004.

[57] Yamamoto H. Yamaguchi Y. Yamaguchi, K. and H. Watanabe. Antiferromagnetism of $Fe_{1+d}Sb$. *Journal of the Physical Society of Japan*, 33(5):1292–1295, 1972.

[58] Yamaguchi Y. Tomiyoshi S Kazama N. Yashiro, T. and H. Watanabe. Magnetic structure of $Fe_{1+d}Sb$. *Journal of the Physical Society of Japan*, 34(1):58–62, 1973.

[59] F. W. Richter and K. Schmidt. Mossbauer-Spectroscopy in system $Fe_{1+x}Sb$ with NiAs-structure. *Zeitschrift für Naturforschung Section A-A Journal of Physical Sciences*, 30(12):1621–1626, 1975.

[60] G. Lefevre, M. Ulrich, F. Behar, C. Servant, and G. Cizeron. Structures of phases $Fe_{1+x}Sb$ and $FeSb_2$. *Journal of the Less-Common Metals*, 60(2):283–299, 1978.

[61] C. Blaauw, C. G. White, and W. Leiper. Hyperfine interactions of Fe-57 in $Fe_{1+x}Sb$. *Physica Status Solidi B-Basic Research*, 91(2):K129–K132, 1979.

[62] P. J. Picone and P. E. Clark. Magnetic-ordering of interstitial iton in $Fe_{1+x}Sb$ alloys. *Journal of Magnetism and Magnetic Materials*, 25(2):140–146, 1981.

[63] P. J. Picone and P. E. Clark. Mossbauer measurements on lattice and interstitial iron atoms in $Fe_{1+x}Sb$ alloys. *Journal of Magnetism and Magnetic Materials*, 12(3):233–238, 1979.

[64] A. Bentien, S. Johnsen, G. K. H. Madsen, B. B. Iversen, and F. Steglich. Colossal

Seebeck coefficient in strongly correlated semiconductor $FeSb_2$. *Epl*, 80(3):17008–p1 – 17008–p5, 2007.

[65] G. Aeppli and Z. Fisk. *Comments Condens. Matter Physics*, 16:155–165, 1992.

[66] P. Sun, N. Oeschler, S. Johnsen, B. B. Iversen, and F. Steglich. Narrow band gap and enhanced thermoelectricity in $FeSb_2$. *Dalton Transactions*, 39(4):1012–1019, 2010.

[67] R. Orru, R. Licheri, A. M. Locci, A. Cincotti, and G. Cao. Consolidation/synthesis of materials by electric current activated/assisted sintering. *Materials Science & Engineering R-Reports*, 63(4-6):127–287, 2009.

[68] S. Schlecht, C. Erk, and M. Yosef. Nanoscale zinc antimonides: Synthesis and phase stability. *Inorganic Chemistry*, 45(4):1693–1697, 2006.

[69] U. Kolb, T. Gorelik, C. Kubel, M. T. Otten, and D. Hubert. Towards automated diffraction tomography: Part I - Data acquisition. *Ultramicroscopy*, 107(6-7):507–513, 2007.

[70] U. Kolb, T. Gorelik, and M. T. Otten. Towards automated diffraction tomography. Part II - Cell parameter determination. *Ultramicroscopy*, 108(8):763–772, 2008.

[71] R. Vincent and P. A. Midgley. Double conical beam-rocking system for measurement of integrated electron diffraction intensities. *Ultramicroscopy*, 53(3):271–282, 1994.

[72] C. S. Own. *System Design and Verification of the Precession Electron Diffraction Technique*. 2005.

[73] A. Avilov, K. Kuligin, S. Nicolopoulos, M. Nickolskiy, K. Boulahya, J. Portillo, G. Lepeshov, B. Sobolev, J. P. Collette, N. Martin, A. C. Robins, and P. Fischione. Precession technique and electron diffractometry as new tools for crystal structure analysis and chemical bonding determination. *Ultramicroscopy*, 107(6-7):431–444, 2007.

[74] E. Mugnaioli, T. Gorelik, and U. Kolb. "Ab initio" structure solution from electron diffraction data obtained by a combination of automated diffraction tomography and precession technique. *Ultramicroscopy*, 109(6):758–765, 2009.

[75] T. Novet and D. C. Johnson. New synthetic approach to extended solids - selected synthesis of iron silicides via the amorphous state. *Journal of the American Chemical Society*, 113(9):3398–3403, 1991.

[76] M. Noh, J. Thiel, and D. C. Johnson. Synthesis of crystalline superlattices by controlled crystallization of modulated reactants. *Science*, 270(5239):1181–1184, 1995.

[77] J. Etzkorn, H. A. Therese, F. Rocker, N. Zink, U. Kolb, and W. Tremel. Metal-organic chemical vapor deposition synthesis of hollow inorganic-fullerene-type MoS_2 and $MoSe_2$ nanoparticles. *Advanced Materials*, 17(19):2372–2375, 2005.

[78] Y. G. Sun and Y. N. Xia. Shape-controlled synthesis of gold and silver nanoparticles. *Science*, 298(5601):2176–2179, 2002.

[79] B. M. Leonard, N. S. P. Bhuvanesh, and R. E. Schaak. Low-temperature polyol synthesis of $AuCuSn_2$ and $AuNiSn_2$: Using solution chemistry to access ternary intermetallic compounds as nanocrystals. *Journal of the American Chemical Society*, 127(20):7326–7327, 2005.

[80] G. M. Sheldrick. A short history of SHELX. *Acta Crystallographica Section A*, 64:112–122, 2008.

[81] M. C. Burla, R. Caliandro, M. Camalli, B. Carrozzini, G. L. Cascarano, L. de Caro, C. Giacovazzo, G. Polidori, D. Siliqi, and R. Spagna. IL MILIONE: a suite of computer programs for crystal structure solution of proteins. 40(3):609–613, 2007.

[82] J. Jansen. *Structure Refinement by Taking Dynamical Diffraction into Account*. Springer Netherlands, 2006.

[83] E. Zintl. Intermetallische Verbindungen. *Angewandte Chemie*, (52):1–6, 1939.

[84] R. Nesper. Bonding patterns in intermetallic compounds. *Angewandte Chemie-International Edition in English*, 30(7):789–817, 1991.

[85] G. A. Papoian and R. Hoffmann. Hypervalent bonding in one, two, and three dimensions: Extending the Zintl-Klemm concept to nonclassical electron-rich networks. *Angewandte Chemie-International Edition*, 39(14):2409–2448, 2000.

[86] A. Coelho. TOPAS Academic V1.0, 2004.

[87] NanoMEGAS. NanoMEGAS: Advanced Tools for Electron Diffraction, 2004.

[88] Heil U. Schlitt S. Schömer E. ADT-3D: A software package for ADT data visualizing and processing.

[89] B. L. Pedersen, H. Birkedal, B. B. Iversen, M. Nygren, and P. T. Frederiksen. Influence of sample compaction on the thermoelectric performance of Zn_4Sb_3. *Applied Physics Letters*, 89(24), 2006.

[90] K. Ueno, A. Yamamoto, T. Noguchi, T. Inoue, S. Sodeoka, H. Takazawa, C. H. Lee, and H. Obara. Optimization of hot-press conditions of Zn_4Sb_3 for high thermoelectric performance - I. Physical properties and thermoelectric performance. *Journal of Alloys and Compounds*, 384(1-2):254–260, 2004.

[91] C. S. Birkel, E. Mugnaioli, T. Gorelik, U. Kolb, M. Panthöfer, and W. Tremel. Solution Synthesis of a New Thermoelectric $Zn_{1+x}Sb$ Nanophase and Its Structure Determination Using Automated Electron Diffraction Tomography. *Journal of the American Chemical Society*, 132(28):9881–9889, 2010.

[92] G. J. Snyder, M. Christensen, E. Nishibori, T. Caillat, and B. B. Iversen. Disordered zinc in Zn_4Sb_3 with phonon-glass and electron-crystal thermoelectric properties. *Nature Materials*, 3(7):458–463, 2004.

[93] R. P. Hermann, F. Grandjean, and G. J. Long. Einstein oscillators that impede thermal transport. *American Journal of Physics*, 73(2):110–118, 2005.

[94] C. Stiewe, T. Dasgupta, L. Boettcher, B. Pedersen, E. Mueller, and B. Iversen. Thermoelectric Characterization of Zone-Melted and Quenched Zn_4Sb_3. *Journal of Electronic Materials*, 39(9):1975–1980, 2010.

[95] A. Coelho. TOPAS Academic V4.1, 2007.

[96] F. L. Carter and R. Mazelsky. ZnSb structure - further inquiry. *Journal of Physics and Chemistry of Solids*, 25(6):571–581, 1964.

[97] F. Weitzer, K. Remschnig, J. C. Schuster, and P. Rogl. Phase-equilibria and structural chemistry in the ternary-systems Al-Si-N, Cu-Si-N, Zn-Si-N, Ag-Si-N, Cd-Si-N, In-Si-N, Sn-Si-N, Sb-Si-N, Au-Si-N, Tl-Si-N, Pb-Si-N, Bi-Si-N and

Al-B-N, Cu-B-N, Zn-B-N, Ag-B-N, Cd-B-N, In-B-N, Sn-B-N, Sb-B-N, Au-B-N, Tl-B-N, Pb-B-N, Bi-B-N. *Journal of Materials Research*, 5(10):2152–2159, 1990.

[98] E. H. Kisi and M. M. Elcombe. Upsilon-parameters for the wurtzite structure of ZnS and ZnO using powder neutron-diffraction. *Acta Crystallographica Section C-Crystal Structure Communications*, 45(Part 12):1867–1870, 1989.

[99] G. E. Bacon. Unit-cell dimensions of graphite. *Acta Crystallographica*, 3(2):137–139, 1950.

[100] P. Ziolkowski, G. Karpinski, D. Platzek, C. Stiewe, and E. Müller. Application Overview of the Potential Seebeck Microscope. *Thermoelectrics, 2006. ICT´06.*, pages 684–688, 2006.

[101] H. Holseth and A. Kjekshus. Compounds with marcasite type crystal structure 4. Crystal structure of $FeSb_2$. *Acta Chemica Scandinavica*, 23(9):3043, 1969.

[102] W. Trzebiatowski and E. Bryjak. Röntgenanalyse des Systems Arsen–Antimon. *Z. Anorg. Allg. Chem.*, 238(2-3):255–267, 1938.

[103] J. R. Allan and A. D. Paton. Thermal analyses and electrical studies of bis[dicrbonyl(π-cyclopentadienyl)iron(II). *Thermochimica Acta*, 231:333–335, 1994.

[104] S. Caric, L. Marinkov, and J. Slivka. Mossbauer Study of Thermal-Decomposition of $FeC_2O_4.2H_2O$. *Physica Status Solidi A-Applied Research*, 31(1):263–268, 1975.

[105] J. Steger and E. Kostiner. Mossbauer-effect study of $FeSb_2$. *Journal of Solid State Chemistry*, 5(1):131–135, 1972.

[106] D. Neidherr, G. Audi, D. Beck, K. Blaum, Ch. Böhm, M. Breitenfeldt, R. B. Cakirli, R. F. Casten, S. George, F. Herfurth, A. Herlert, A. Kellerbauer, M. Kowalska, D. Lunney, E. Minaya-Ramirez, S. Naimi, E. Noah, L. Penescu, M. Rosenbusch, S. Schwarz, L. Schweikhard, and T. Stora. Discovery of ^{229}Rn and the Structure of the Heaviest Rn and Ra Isotopes from Penning-Trap Mass Measurements. *Physical Review Letters*, 102(11):112501, Mar 2009.

[107] W. Sturhahn, T. S. Toellner, E. E. Alp, X. Zhang, M. Ando, Y. Yoda, S. Kikuta, M. Seto, C. W. Kimball, and B. Dabrowski. Phonon density of states measured by inelastic nuclear resonant scattering. *Phys. Rev. Lett.*, 74(19):3832–3835, 1995.

[108] H. C Wille, R. P. Hermann, I. Sergueev, O. Leupold, P. van der Linden, B. C. Sales, F. Grandjean, Gary J. Long, R. Rueffer, and Yu V. Shvyd'ko. Antimony vibrations in skutterudites probed by Sb-121 nuclear inelastic scattering. *Physical Review B*, 76(14), 2007.

[109] J. Xie, X. B. Zhao, G. S. Cao, M. J. Zhao, Y. D. Zhong, and L. Z. Deng. Electrochemical lithiation and delithiation of $FeSb_2$ anodes for lithium-ion batteries. *Materials Letters*, 57(30):4673–4677, 2003.

[110] Quantum Design. *Physical Property Measurement System Thermal Transport Option User´s Manual*. San Diego, 2002.

[111] Y. Deng, C. W. Cui, N. L. Zhang, T. H. Ji, Q. L. Yang, and L. Guo. Fabrication of bismuth telluride nanotubes via a simple solvothermal process. *Solid State Communications*, 138(3):111–113, 2006.

[112] A. I. Boukai, Y. Bunimovich, J. Tahir-Kheli, J.-K. Yu, W. A. III Goddard, and

J. R. Heath. Silicon nanowires as efficient thermoelectric materials. *Nature*, 451(7175):168–171, 2008.

[113] Y. Deng, C. W. Nan, G. D. Wei, L. Guo, and Y. H. Lin. Organic-assisted growth of bismuth telluride nanocrystals. *Chemical Physics Letters*, 374(3-4):410–415, 2003.

[114] H. Yu, P. C. Gibbons, and W. E. Buhro. Bismuth, tellurium, and bismuth telluride nanowires. *Journal of Materials Chemistry*, 14(4):595–602, 2004.

[115] M. Martin-Gonzalez, G. J. Snyder, A. L. Prieto, R. Gronsky, T. Sands, and A. M. Stacy. Direct electrodeposition of highly dense 50 nm $Bi_2Te_{3-y}Se_y$ nanowire arrays. *Nano Letters*, 3(7):973–977, 2003.

[116] M. Martin-Gonzalez, A. L. Prieto, R. Gronsky, T. Sands, and A. M. Stacy. High-density 40 nm diameter Sb-rich $Bi_{2-x}Sb_xTe_3$ nanowire arrays. *Advanced Materials*, 15(12):1003–1006, 2003.

[117] M. Martin-Gonzalez, A. L. Prieto, M. S. Knox, R. Gronsky, T. Sands, and A. M. Stacy. Electrodeposition of $Bi_{1-x}Sb_x$ films and 200-nm wire arrays from a non-aqueous solvent. *Chemistry of Materials*, 15(8):1676–1681, 2003.

[118] M. S. Sander, A. L. Prieto, R. Gronsky, T. Sands, and A. M. Stacy. Fabrication of high-density, high aspect ratio, large-area bismuth telluride nanowire arrays by electrodeposition into porous anodic alumina templates. *Advanced Materials*, 14(9):665–667, 2002.

[119] A. L. Prieto, M. S. Sander, M. Martin-Gonzalez, R. Gronsky, T. Sands, and

A. M. Stacy. Electrodeposition of ordered Bi_2Te_3 nanowire arrays. *Journal of the American Chemical Society*, 123(29):7160–7161, 2001.

[120] M. Martin-Gonzalez, A. L. Prieto, R. Gronsky, T. Sands, and A. M. Stacy. Insights into the electrodeposition of Bi_2Te_3. *Journal of the electrochemical society*, 149(11):C546–C554, 2002.

[121] E. J. Menke, Q. Li, and R. M. Penner. Bismuth telluride (Bi_2Te_3) nanowires synthesized by cyclic electrodeposition/stripping coupled with step edge decoration. *Nano Letters*, 4(10):2009–2014, 2004.

[122] H. Masuda and K. Fukuda. Ordered metal nanohole arrays made by a 2-step replication of honeycomb structures of anodic alumina. *Science*, 268(5216):1466–1468, 1995.

List of publications

K. Page, **C. S. Schade**, J. Zhang, P. J. Chupas, K. W. Chapman, T. Proffen, A. K. Cheetham, and R. Seshadri. "Preparation and characterization of Pd_2Sn nanoparticles." *Materials Research Bulletin*, **42**, 12 (2007).

C. S. Birkel, E. Mugnaioli, T. Gorelik, U. Kolb, M. Panthöfer, and W. Tremel. "Solution Synthesis of a New Thermoelectric $Zn_{1+x}Sb$ Nanophase and Its Structure Determination Using Automated Electron Diffraction Tomography." *JACS*, **132**, 28 (2010).

C. S. Birkel, T. Claudio, D. Bessas, G. Kieslich, R. Branscheid, U. Kolb, M. Panthöfer, R. Hermann, and W. Tremel "Novel Solution Synthesis and Characterization of Nanostructured $FeSb_2$." *(in preparation)*

C. S. Birkel, T. Claudio, M. Panthöfer, A. Birkel, D. Koll, G. Kieslich, J. Schmidt, R. Hermann, and W. Tremel "Compaction of Nanostructured $Zn_{1+x}Sb$ by Spark Plasma Sintering and Characterization of Obtained Pellets." *(in preparation)*

C. S. Birkel, T. Claudio, D. Bessas, M. Schwall, M. Panthöfer, A. Birkel, D. Koll, G. Kieslich, C. Felser, J. Schmidt, R. Hermann, and W. Tremel "Compaction of Nanostructured $FeSb_2$ by Spark Plasma Sintering and Characterization of Obtained Pellets" *(in preparation)*

C. S. Birkel, D. Bessas, G. Kieslich, A. Stewart, M. Panthöfer, R. Hermann, U. Kolb, and W. Tremel "Synthesis of Nanostructured $Fe_{1+x}Sb$ and its Structure Determination by Automated Diffraction Tomographie" *(in preparation)*

International conferences with poster contributions

Gordon Research Conference on Solid State Chemistry, Colby-Sawyer College, USA, 2010

451. WE-Heraeus-Seminar, Bad Honnef, Germany, 2010

28th International Thermoelectric Conference, Freiburg, Germany, 2009

IRTG Spring Meeting, Seoul, South Korea, 2009

International Conference on Advanced Functional Polymers and Self-Organized Materials, Busan, South Korea, 2008

Gordon Conference on Solid State Chemistry, Colby-Sawyer College, USA, 2008

IRTG Spring Meeting, Rottach-Egern, Germany, 2008

International conferences with oral presentations

Gordon Research Conference on Solid State Chemistry, Colby-Sawyer College, USA, 2010 – invited poster talk

28th International Thermoelectric Conference, Freiburg, Germany, 2009